August 2016

Deep Tissue Light Delivery and Fluorescence Tomography with Applications in Optogenetic Neurostimulation

Mehdi Azimipour
University of Wisconsin-Milwaukee

Deep tissue light delivery and fluorescence tomography with applications in optogenetic neurostimulation

by

Mehdi Azimipour

A Dissertation Submitted in

Partial Fulfillment of the

Requirements for the Degree of

Doctor of Philosophy

in Engineering

at

The University of Wisconsin–Milwaukee

August 2016

Abstract

Deep tissue light delivery and fluorescence tomography with applications in optogenetic neurostimulation

by

Mehdi Azimipour

The University of Wisconsin–Milwaukee, 2016
Under the Supervision of Professor Ramin Pashaie

Study of the brain microcircuits using optogenetics is an active area of research. This method has a few advantages over the conventional electrical stimulation including the bi-directional control of neural activity, and more importantly, specificity in neuromodulation. The first step in all optogenetic experiments is to express certain light sensitive ion channels/pumps in the target cell population and then confirm the proper expression of these proteins before running any experiment. Fluorescent bio-markers, such as green fluorescent protein (GFP), have been used for this purpose and co-expressed in the same cell population. The fluorescent signal from such proteins provides a monitory mechanism to evaluate the expression of optogenetic opsins over time. The conventional method to confirm the success in gene delivery is to sacrifice the animal, retract and slice the brain tissue, and image the corresponding slices using a fluorescent microscope. Obviously, determining the level of expression over time without sacrificing the animal is highly desirable. Also, optogenetics can be combined with cell-type specific optical recording of neural activity for example by imaging the fluorescent signal of genetically encoded calcium indicators.

One challenging step in any optogenetic experiment is delivering adequate amount of light to target areas for proper stimulation of light sensitive proteins. Delivering sufficient light density to a target area while minimizing the off-target stimulation requires a precise estimation of the light distribution in the tissue. Having a good estimation of the tissue optical properties is necessary for predicting the distribution of light in any turbid medium. The first

objective of this project was the design and development of a high resolution optoelectronic device to extract optical properties of rats' brain tissue (including the absorption coefficient, scattering coefficient, and anisotropy factor) for three different wavelengths: $405nm$, $532nm$ and $635nm$ and three different cuts: transverse, sagittal, and coronal. The database of the extracted optical properties was linked to a 3D Monte Carlo simulation software to predict the light distribution for different light source configurations. This database was then used in the next phase of the project and in the development of a fluorescent tomography scanner. Based on the importance of the fluorescent imaging in optogenetics, another objective of this project was to design a fluorescence tomography system to confirm the expression of the light sensitive proteins and optically recording neural activity using calcium indicators none or minimally invasively. The method of fluorescence laminar optical tomography (FLOT) has been used successfully in imaging superficial areas up to $2mm$ deep inside a scattering medium with the spatial resolution of $\sim 200\mu m$. In this project, we developed a FLOT system which was specifically customized for in-vivo brain imaging experiments.

While FLOT offers a relatively simple and non-expensive design for imaging superficial areas in the brain, still it has imaging depth limited to $2mm$ and its resolution drops as the imaging depth increases. To address this shortcoming, we worked on a complementary system based on the digital optical phase conjugation (DOPC) method which was shown previously that is capable of performing fluorescent tomography up to $4mm$ deep inside a biological tissue with lateral resolution of $\sim 50\mu m$. This system also provides a non-invasive method to deliver light deep inside the brain tissue for neurostimulation applications which are not feasible using conventional techniques because of the high level of scattering in most tissue samples. In the developed DOPC system, the performance of the system in focusing light *through* and *inside* scattering mediums was quantified. We also showed how misalignments and imperfections of the optical components can immensely reduce the capability of a DOPC setup. Then, a systematic calibration algorithm was proposed and experimentally applied to our DOPC system to compensate main aberrations such as reference beam aberrations and

also the backplane curvature of the spatial light modulator. In a highly scattering sample, the calibration algorithm achieved up to 8 fold increase in the PBR.

To My Family

Table of Contents

List of Figures

List of Tables

List of Abbreviations

AFG Arbitrary Function Generator

AOM Acousto-Optic Modulation

APD Avalanche Photo-Diode

ART Algebraic Reconstruction Technique

CCD Charge Coupled Device

ChR2 Channelrhodopsin-2

CW Continuous Wave

CSF Cerebro-Spinal Fluid

DPSS Diode-Pumped Solid-State Laser

DOPC Digital Optical Phase Conjugation

DOT Diffusion Optical Tomography

DAQ Data Acquisition

DMD Deformable Mirror Device

EOM Electro-Optic Modulator

EMCCD Electron Multiplying Charge Coupled Device

FAD Flavin Adenine Dinucleotide

FD Frequency Domain

FLOT Fluorescence Laminar Optical Tomography

fMRI functional Magnetic Resonance Imaging

FP Fluorescent Protein

GFP Green Fluorescent Protein

IAD Inverse Adding Doubling

IACUC Institutional Animal Care and Use Committee

KM Kubelka-Munk

LSQR Lease Square

MIP Maximum Intensity Projection

MCA Middle Cerebral Artery

MEMS Micro-Electro-Mechanical Systems

NpHR Natronomonas Haraonis Halorhodopsin

NA Numerical Aperture

OCT Optical Coherence Tomography

OPC Optical Phase Conjugation

PBS Phosphate-Buffered Saline

PDMS Polydimethylsiloxane

PBR Peak to Background Ratio

PSF Point Spread Function

PCM Phase Conjugate Mirror

RTE Radiative Transport Equation

RMS Root-Mean-Square

SART Simultaneous Algebraic Reconstruction Technique

SIRT Simultaneous Iterative Reconstruction Technique

SLM Spatial Light Modulators

SD-OCT Spectral-Domain Optical Coherence Tomography

SLD Superluminescence Laser Diode

sCMOS Scientific CMOS

TiO2 Titanium Dioxide

TRUE Time-Reversed Ultrasonically Encoded

TRACK Time Reversal by Analysis of Changing wavefronts from Kinetic targets

TRAP Time-Reversed Adapted-Perturbation

TR Time Resolved

YFP Yellow Fluorescent Protein

Acknowledgements

First of all, I would like to express my sincere gratitude to my advisor Prof. Ramin Pashaie for providing me with the opportunity to work toward my phd at bio-inspired science and technology lab, his continuous support during my Ph.D study, his motivation and guidance. I appreciate his vast knowledge, insightful comments and constructive discussions which helped me in all the time of research. Besides my advisor, I would like to thank the rest of my thesis committee members: Prof. Armstrong, Prof. Law, Prof. Hirschmugl and Prof. Schmidt, for their insightful comments.

I thank my fellow labmates, Ryan Falk, Ryan Baumgartner, Seth, Alana, Amy, Mahya, Ghazal, Rex, Fariborz, Israel, Tamara, and in particular, Farid who was always willing to help.

Last but not the least, I would like to thank my family for their support and encouraging me with their best wishes and looking forward to see them soon!

Chapter 1

Introduction and Background

Optogenetics

Optognetics is a relatively new neurostimulation methodology invented by combining new advances in optics and tools of molecular genetics [1, 2]. To better understand the role of each sub-population of neurons in collective processing of sensory inputs, leading to cognition, perception or other vital functions of the nervous system, a versatile mechanism to reversibly and bi-directionally control the activity of each cell-type is needed [3]. To achieve this goal via optogenetics, we first deliver microbial opsin genes that encode light-gated ion channels, e.g., Channelrhodopsin-2 (ChR2) [4], or ion pumps, e.g., Natronomonas Pharaonis HaloRhodopsin (NpHR) [5], to target a specific cell population. Once such proteins are expressed in a cell, its activity can be modulated just by exposing the cell to light pulses of appropriate wavelengths. ChR2 is mostly a monovalent cation channel that allows the influx of Sodium ions (Na+) to the cell when exposed to blue light and the protein has maximum sensitivity to $\sim 470nm$ wavelength. In contrast, NpHR is a Chloride (Cl-) pump which gets activated when exposed to yellow light with maximum sensitivity to $580nm$ wavelength. Mechanisms of optical activation and the sensitivity spectrum of both ChR2 and NpHR proteins are shown in Figure 1.1 (a), (b). Since the sensitivity spectrum of ChR2 and NpHR are well separated and we have about $100nm$ distance between the peak sensitivity of these proteins, in case we co-express both molecules in a single cell population, the activity level of that cell-type can be controlled bi-directionally by controlling light exposures and without significant interference with other cell populations in the region. As shown in Figure 1.1 (c), a typical neuron co-expressing both proteins responds to blue light pulses by generating a

sequence of well-correlated action potentials, while yellow light exposure hyperpolarizes the cell and inhibits any further activity.

In order to use optogenetics to interrogate the functionality of a cell population in large-scaled neural networks we need to: (1) generate optogenetic proteins in the target cells, (2) design an appropriate strategy for light delivery for example by implanting optical fibers in the brain of the animal under test, see Figure 1.2 (a),(b), and possibly (3) a readout mechanism to continuously assess the neural activity via electrophysiology recording, functional magnetic resonance imaging (fMRI), or by fluorescent imaging of loaded dyes or genetically encoded indicators including Calcium indicators or voltage sensitive dyes [2]. To summarize, optogenetics has multiple advantages over the conventional electrode-based neurostimulation methods including [6]:

- Optogenetics provides a bi-directional mechanism to selectively and reversibly stimulate or suppress neural activity. Direct inhibition of neural activity is not feasible via conventional neurostimulation via micro electrodes.

- Taking advantage of the inherent parallelism of optics, optogenetics provides a systematic approach to generate dynamic patterns of neurostimulation with high spatial-temporal resolution.

- Optogenetics offers an unprecedented targeting strategy to manipulate the activity of specific neural sub-populations. As displayed in Figure 1.2(c), in the conventional electrical stimulation, it is not possible to avoid stimulating other adjacent cell-types while stimulating the target neurons. By using the tools of molecular genetics, it is possible to selectively express optogenetic tools solely in the target neurons. As a result, other cell populations remain neutral and do not respond to exposing light pulses.

An important step in designing optogenetic experiments is to confirm that adequate amount of light is delivered to the target area. Besides implanting optical fibers in the brain to guide and deliver pulses of light to different brain regions, particularly to optically stimulate deep

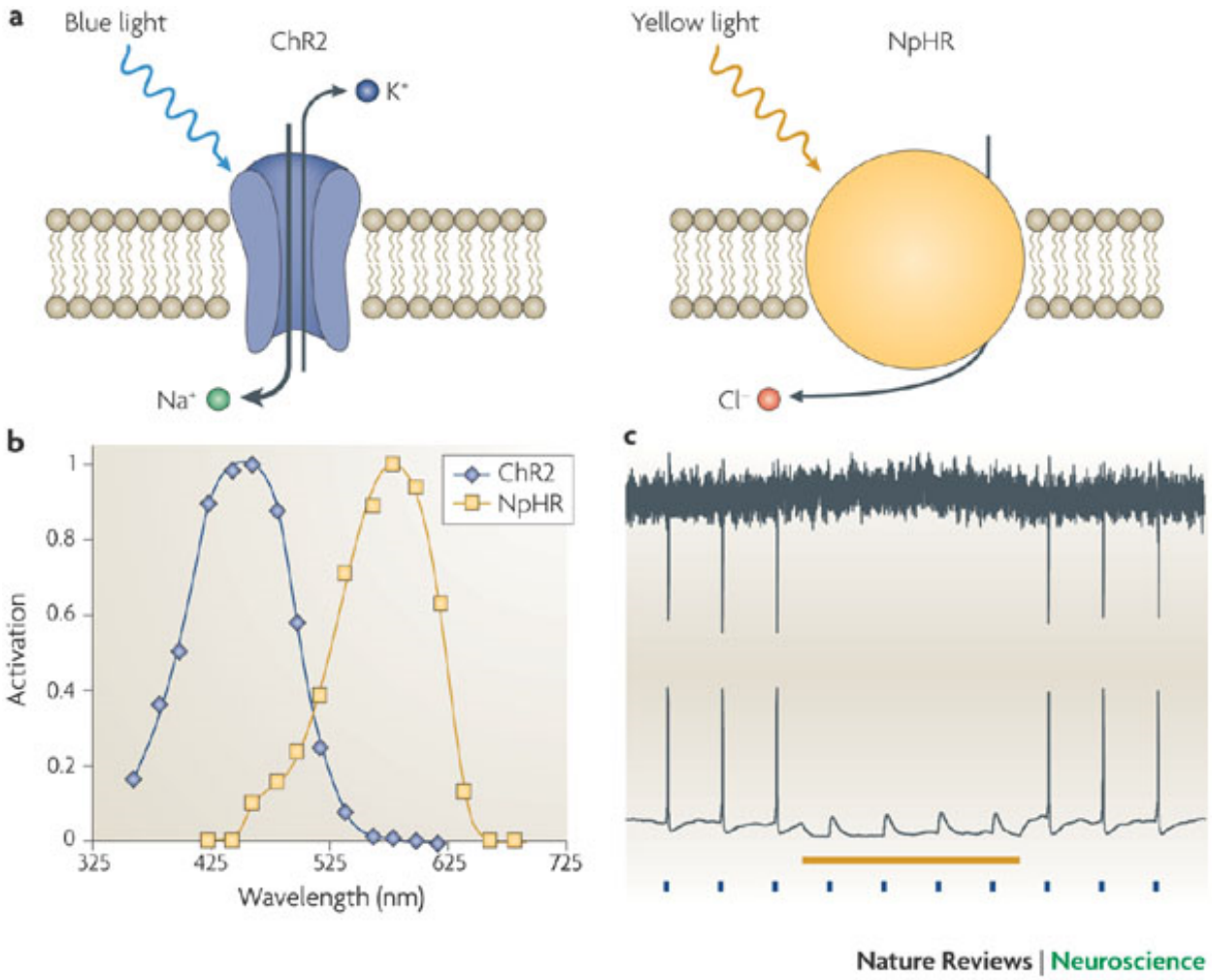

Figure 1.1: (A) Functionality of the main optogenetic proteins, ChR2 and NpHR, (B) sensitivity spectrum of ChR2 and NpHR, (C) blue light flashes generate action potentials in neurons, while yellow light inhibits the activity [3].

brain objects in in-vivo experiments, more advanced technologies are also explored to implement complex light delivery algorithms. In recent years, microelectromechanical systems (MEMS) and liquid crystal spatial light modulators are employed to project complex, and even three-dimensional, light stimulation patterns inside the tissue [7, 8, 9]. Using such advanced technologies makes it possible to step-by-step dissect complex large-scaled networks of neurons and systematically study the function and involvement of each cell-type while the network is processing the input data or in understanding the role of such cell populations in the dynamics of certain neurological and psychiatric diseases.

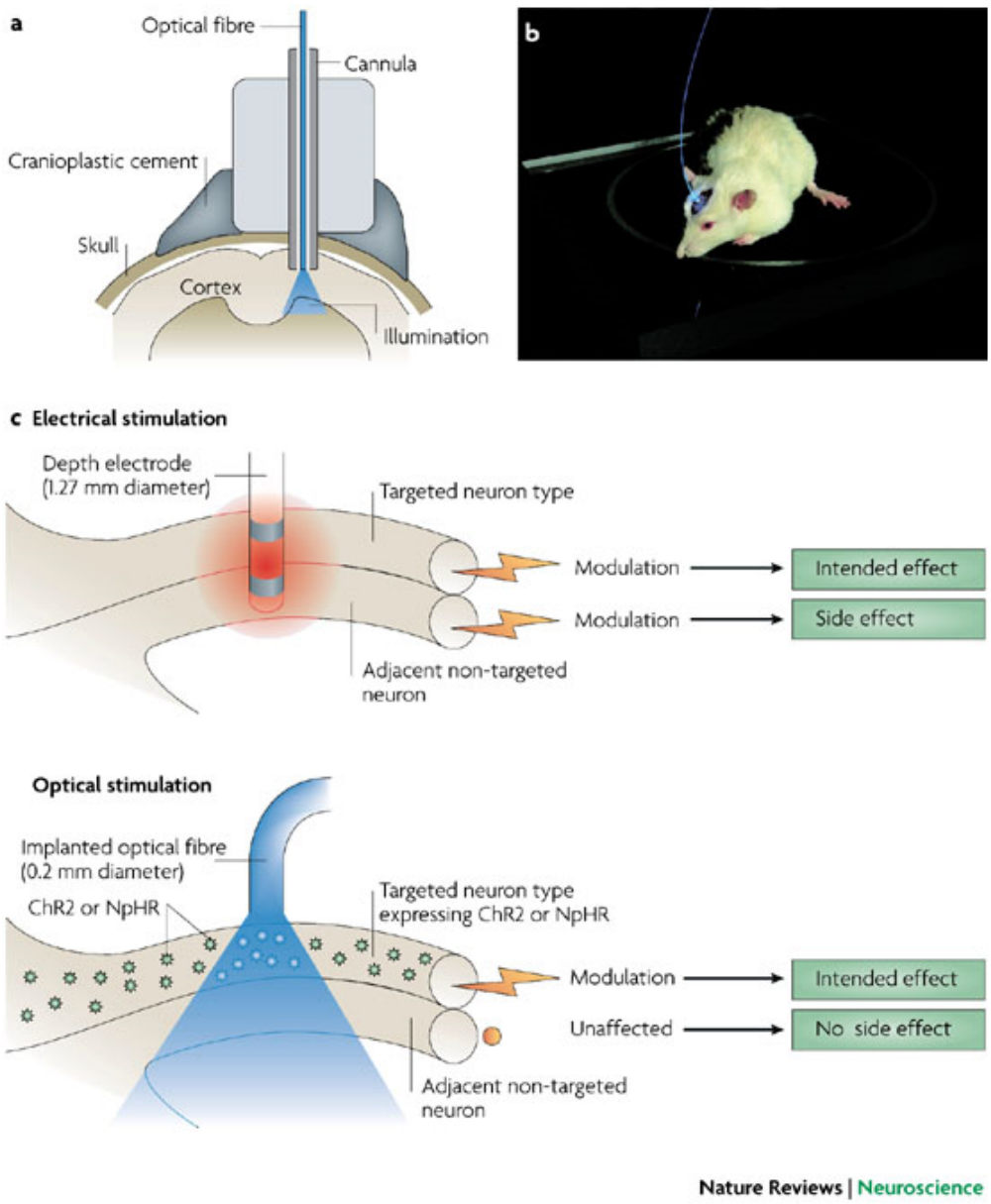

Figure 1.2: (A) An optical fiber is implanted on a skull to deliver light to a target area, (B) blue laser at $488nm$ is launched into the optical fiber, (C) in optogenetics, cell-type targeting of neurons is possible. In this technique, ChR2 or NpHR are co-expressed in a specific cell population and avoid inadvertent stimulation of adjacent non-targeted cells which is not feasible in conventional electrical stimulation methods [3].

Designing appropriate readout strategy is another important step in designing optogenetic experiments. A common method for recording neural activity is using micro-electrodes or electrode arrays. One main problem in electrical stimulation/recording is the generation of artifacts which makes the simultaneous stimulation and activity recording difficult [2].

Optogenetic provides a powerful tool for optical stimulation and parallel recording of neural activity and can be combined with electrode recording [10]. When both optical stimulation and electrical readouts are integrated into a single device, the resulted tool is called "optrode" [11] and these devices are currently widely used by researchers. Nonetheless, in electrical recording, presence of the artifacts, caused by the interaction between light and metal electrodes or temperature fluctuations, might lead to misinterpretation of the acquired data. On the other hand, an appealing approach for recording neural activity during optogenetic stimulation is based on using fluorescent proteins (FP) and optical imaging. Fluorescent proteins can convert physiological signals, such as changes in the concentration of a specific ion, membrane voltage of cells, or pH level of the surrounding environment to some form of fluorescence output [12]. For example, generation of action potentials in cells is usually associated with influx of Calcium ion (Ca2+). Therefore, detection of Calcium ion concentration can be an indirect indicator of neural activity [13]. Fluorescence imaging using Ca2+ dyes, such as fura-2 or Fluo-5F, or voltage sensitive dyes, like RH-155, are employed by different researchers while conducting optogenetic experiments [2]. Genetically encoded indicators provide a new tool for specific cell-type fluorescent recording which is not feasible when we use dye-based imaging techniques. Optical recording makes it possible to monitor the activity of larger networks and acquire more information regarding the spatial distribution of neural activity. By using genetics approaches, even cell-type specific activity recording can be accomplished.

Fluorescent proteins are also employed as bio-markers to confirm the expression of optogenetic proteins and assess the level of success in gene delivery. For this purpose, the genetic code of a fluorescent protein is added to the viral vector that delivers the corresponding genes for optogenetic tools. The fluorescent signal from such proteins provides a monitory mechanism to evaluate the expression of optogenetic opsins over time. When fluorescent proteins are illuminated by appropriate wavelengths of light, they emit fluorescent signals which indirectly confirm the expression of optogenetic proteins. The graphics in Figure 1.3(a)

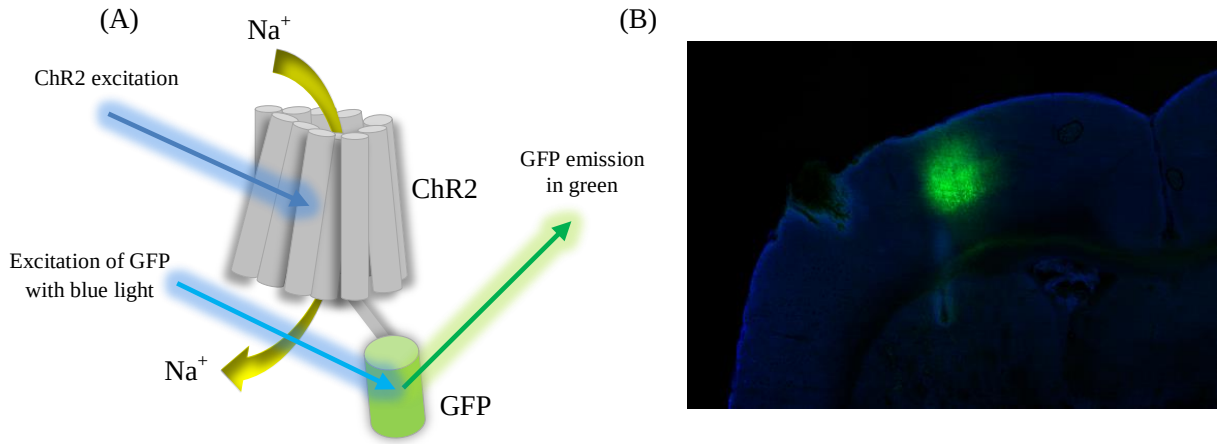

Figure 1.3: (A) Co-expression of light sensitive protein $ChR2$ and green fluorescent protein (GFP). GFP can be excited with a blue light source and its emission spectrum will be in green, (B) confocal fluorescent image of rat brain slice transfected with GFP on the left hemisphere.

shows a typical ChR2 molecule labeled by a green fluorescent protein (GFP). GFP can be excited by blue light illumination to generate green light fluorescence emission. Figure 1.3(b) displays the confocal fluorescence image of a brain slice from one of our experiments and it clearly shows the expression of GFP in the brain of a rat few weeks after receiving the viral transfection for this fluorescence protein.

In conclusion, any successful optogenetic experiment requires: (1) appropriate expression of light sensitive proteins and (2) delivering adequate amount of light to a target area. Delivering sufficient light density to a target area, while minimizing the off-target stimulation, requires reasonably precise estimation of light distribution in the tissue. Having a good estimation of the optical properties is necessary for predicting the distribution of light in any turbid medium. One of the objectives of this project was to design and build a high resolution optoelectronic device to extract optical properties of the rat brain tissue including absorption coefficient, scattering coefficient, and anisotropy factor, for three different wavelengths: $405nm$, $532nm$ and $635nm$, and three different cuts: transverse, sagittal, and coronal. Once this content was produced, the database of the extracted optical properties was linked to a three dimensional Monte Carlo (MC) simulation software to predict light

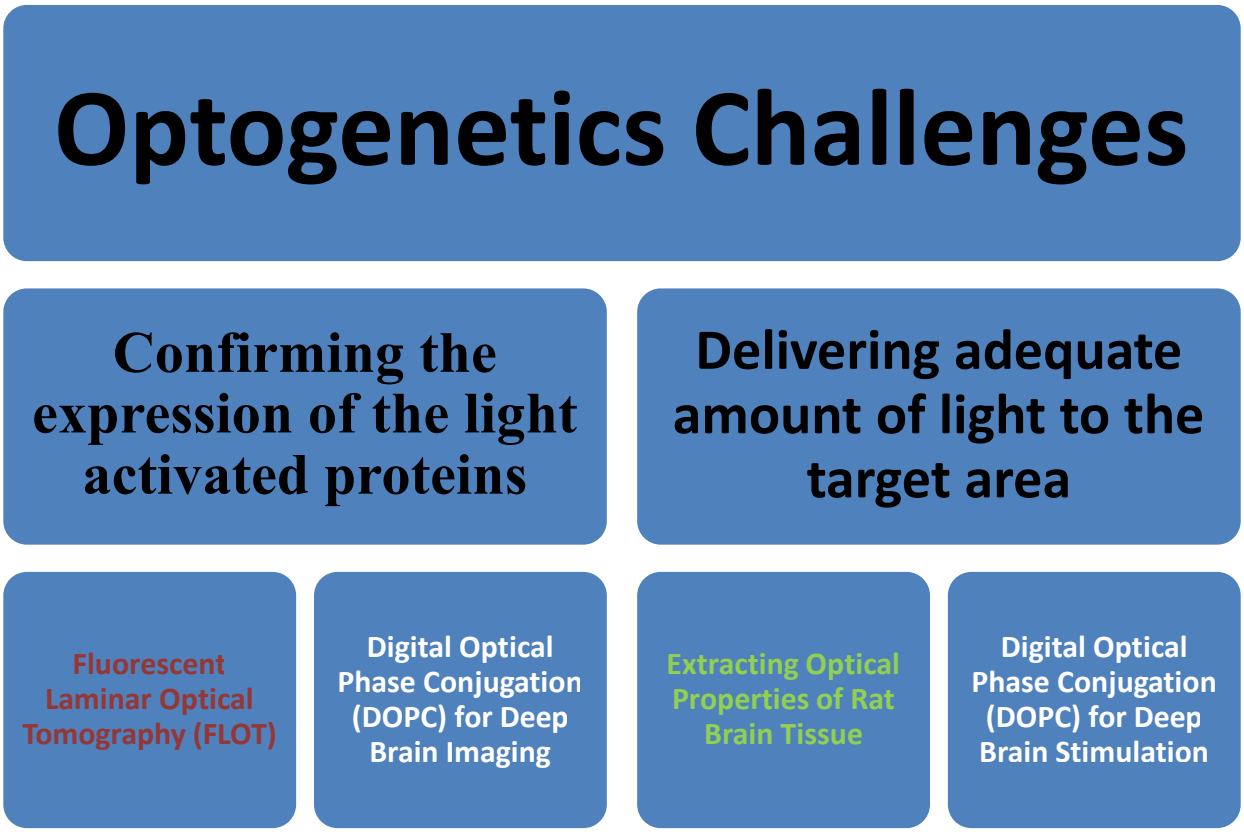

Figure 1.4: Outline of the thesis.

distribution for different light source configurations. Details of this experimental setup and corresponding simulation results are discussed in chapter 2.

To address the second challenge, confirming the expression of light sensitive opsins in the brain of small rodents, we developed a fluorescence laminar optical tomography (FLOT) [65] scanner (both hardware and software) and the system was specifically designed to be used for in-vivo optogenetic experiments. Mesoscopic imaging techniques, such as laminar optical tomography, have a penetration depth in the range of $2mm$ with resolution of $\sim 200\mu m$. In tomography systems that are built based on the diffusion approximation to the radiative transport equation (RTE), it is assumed that the radiation is almost isotropic in the medium. However, such a mathematical model is not suitable for small source-detector separations used in LOT scanners. In LOT imaging, the typical distance between each source and detector is less than the scattering length of photons [65]. Therefore, the propagation of photons

were simulated by the statistical model and more specifically the method of Monte Carlo (MC), discussed in Chapter 2, was employed to simulate the sensitivity matrix for source-detector pair configuration of the LOT setup. To develop an accurate forward model based on MC, a good estimation of the brain optical properties was also needed. The database of rats' brain optical properties, obtained in the first phase of the research, was used for this purpose. Details of the experimental setup, the forward model, and structure of tissue phantoms which were made and used to test the tomography system and results of *in-vivo* fluorescent image reconstructions are discussed in chapter 3.

While FLOT provides a relatively simple approach to image superficial fluorescent objects, the depth of imaging is limited to $\sim 2mm$ and the resolution also noticeably drops as a function of depth in highly scattering tissue such as the brain. Therefore, a more advanced approach, based on digital optical phase conjugation (DOPC) [16], was also explored to build a fluorescence tomography scanner that can reach deeper in the brain and generate images with better resolution. As conceptually proved in [15, 16], by ultrasonically tagging photons and employing optical phase conjugation (OPC) techniques, effect of scattering can be partially compensated so that a coherent beam of light can be focused deep inside a scattering medium beyond the ballistic regime. This system also provides a non-invasive method to deliver light deep inside the brain tissue for neurostimulation application which is not feasible by using conventional techniques. In chapter 4, our design and implementation of a DOPC system and the performance of the system in focusing light *through* and *inside* scattering samples are discussed. In this work, we also showed how misalignments and imperfections of the optical components can immensely reduce the capability of a DOPC setup. To address this challenge, a systematic calibration algorithm was proposed and experimentally tested by using the digital optical phase conjugation platform which was build for this purpose. We systematically proved that the proposed algorithms can compensate and eliminate the effect of main aberrations in a DOPC system including the backplane curvature of the spatial light modulator and the aberration terms in the reference beam.

The block diagram shown in Figure 1.4 summarizes the main objectives of this project.

Chapter 2

Extraction of optical properties and prediction of light distribution in rat brain tissue

This chapter is reproduced with some adaptations from the manuscript [17]:
Azimipour M, Baumgartner R, Liu Y, Jacques SL, Eliceiri K, Pashaie R; Extraction of optical properties and prediction of light distribution in rat brain tissue. J. Biomed. Opt. 0001;19(7):075001. doi:10.1117/1.JBO.19.7.075001. http://dx.doi.org/10.1117/1.JBO.19.7.075001

2.1 Introduction

There has been tremendous interest in recent years in implementing new techniques for optical stimulation of neurons. Optical stimulation is often considered the superior technology, compared with electric stimulation, since the inherent parallelism of optics allows researchers to excite or inhibit the activity of cells in large-scale networks of the brain. Among all developed techniques, optogenetics has become the most popular method and widely used for the study of the dynamics of the brain and circuitry of neurological and psychiatric disorders. In optogenetic brain stimulation, specific cell-types of interest, on the surface or inside the brain tissue, are genetically targeted to express certain light-gated ion channels or ion pumps [18, 19, 20, 21, 22, 23, 24, 25]. Once these proteins are produced in a cell, the activity of the cell can be increased or suppressed simply by exposing the cell to specific wavelengths mostly in the visible range of the spectrum. Obviously, delivering an adequate amount of light to stimulate the target area within the brain is an important step in the design of all optogenetic experiments. An insufficient amount of light cannot generate effective stimula-

tion whereas excessive light intensity can potentially cause damage to the tissue or penetrate deeper and stimulate other brain objects. In optogenetic stimulation, the amplitude of the induced photocurrent in a neuron depends on multiple factors including biological variables such as the kinetics of the expressed opsin [26] and optical properties of the tissue as well as system design variables such as the intensity and wavelength of light. Two separate approaches have been explored for light delivery in optogenetics. For cortical stimulation and superficial areas, spatial light modulators, such as MEMS devices [27] or liquid crystals [28, 29], are employed to generate complex and even three-dimensional patterns of light distributions inside tissue. However, to target deep brain objects, optical fibers are implanted to guide and deliver laser pulses to the region of interest [20, 21, 30, 31, 32].

Predicting the light intensity delivered by an optical fiber to a target area in the brain is necessary for proper *in-vivo* optogenetic stimulation and has been briefly studied before. A simplified *Kubelka-Munk model* [33], which neglects the absorption coefficient, was proposed by Aravanis et. al. [32] and later by Stark et. al. [34]. To develop this model, they conducted a sequence of experiments and measured the intensity of the transmitted light through mouse brain slices of different thicknesses and used this experimental data to formulate a set of equations which estimate the axial variations of light intensity inside the brain tissue. More recently, Al-juboori et. al. [35] used the *fiber punch-through method* to measure the effective attenuation coefficient of different areas of the mouse brain and employed the *Beer-Lambert law* to measure the effective attenuation coefficient in tissue slices of $600\mu m$ thickness. Then, based on the extracted optical properties, the diffusion equation in one-dimension was adapted to determine the required input light intensity needed to deliver the desired optical power to target a deep brain object. Although this approach offers a systematic pathway to measure the tissue effective attenuation coefficient, it is still unable to clarify other optical properties which are essential for precise estimation of light distribution in any turbid medium. Moreover, these models do not incorporate the impact of the tissue heterogeneity on light distribution in the medium.

Obviously, an initial requirement for the design of all biophotonic experiments (including optogenetic stimulation) or related theraputic protocols, is obtaining reasonable estimates of the optical properties of tissue [37]. In most published literature, tissue optical properties are parameterized by three variables: the absorption coefficient, μ_a, the scattering coefficient, μ_s, and the anisotropy factor, g [33]. The mathematical models that are developed to emulate light transport in turbid media use these variables to estimate the distribution and penetration depth of light within the medium [37]. These phenomenological properties of biological tissue can be measured *in vivo* or *in vitro*. For *in-vivo* measurements, multiple time-domain or frequency-domain methods have been developed with instrumentation such as confocal microscopy and optical coherence tomography used to collect the raw data [36]. Then, the values of tissue optical properties are extracted from the raw data by solving a set of inverse problems [38, 39, 40]. Data acquisition *in-vitro* is performed mostly by using double-integrating-sphere setups [41] which are used to measure the total diffuse reflection and transmission, and the intensity of the transmitted ballistic beam. By making these three measurements and using mathematical algorithms, e.g., Inverse Adding Doubling (IAD) method [42], the optical properties of the tissue under test are estimated.

In this chapter, we present a new approach to measure the three variables that define optical properties for the rat brain tissue. To extract the values of these parameters, $500\mu m$ brain slices were prepared and scanned by two customized optical setups and the diffuse transmittance, diffuse reflectance and ballistic transmittance for each slice were measured with high spatial sampling rate of 3000 points per square centimeter. These measurements were made for three different cuts (transverse, sagittal, and coronal) and three different wavelengths, $405nm$, $532nm$, and $635nm$, to cover the visible range of the spectrum. Then, the IAD method [42] was employed to reconstruct the optical properties of the tissue using the collected experimental data. By repeating this procedure for all slices, a three-dimensional database of the tissue optical properties was developed. Next, this database was connected to our three-dimensional (3D) Monte Carlo toolbox [49, 50], to simulate light-tissue interactions

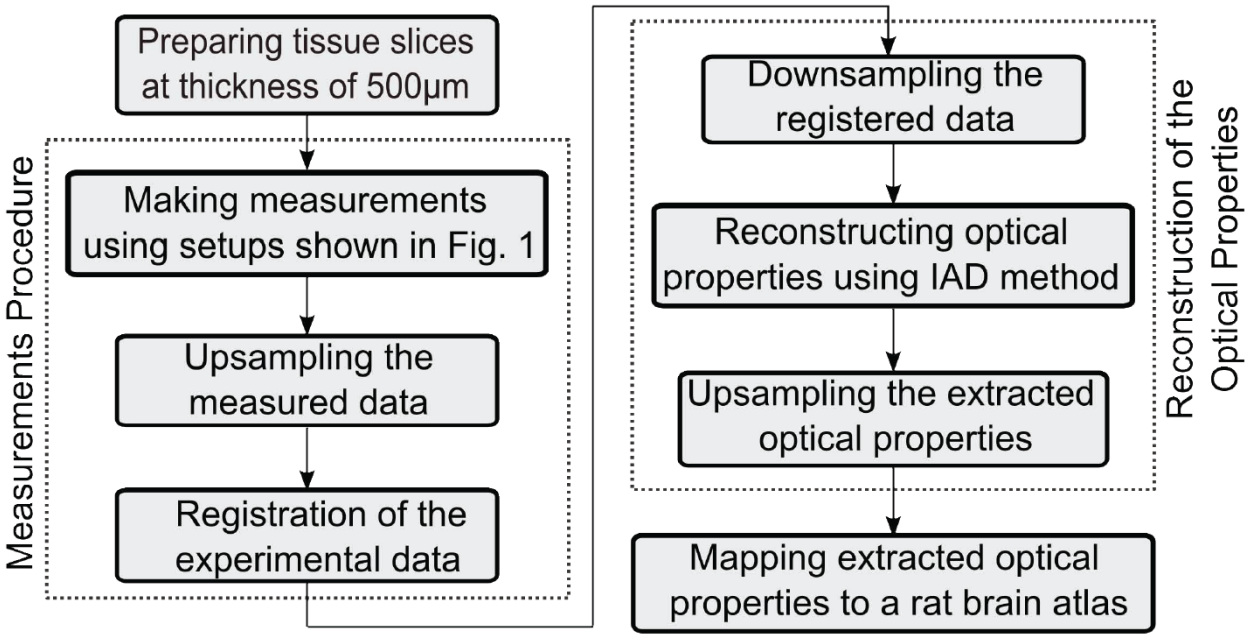

Figure 2.1: The algorithm adapted for extracting tissue optical properties. The process starts with sample preparation in which brain slices of $500\mu m$ thickness are produced and scanned by the customized optical setups shown in Fig. 2.2. Next, the IAD reconstruction algorithm is applied to the collected data to extract the value of parameter which determine the optical properties of the tissue.

and find a reasonable estimation of the distribution of light inside the tissue. The developed software incorporates the effect of tissue heterogeneities, physical parameters of the source, including optical fiber core diameter, numerical aperture or beam type such as uniform or Gaussian [51] and the wavelength of the source, to offer a more accurate model for light distribution in the brain. The process of extracting tissue optical properties is shown in Figure 2.1.

2.2 Material and Methods

2.2.1 Sample preparation

In these experiments, 27 female Sprague-Dawley rats, weighing from $250g$ to $300g$ were used. All animal procedures were approved by the University of Wisconsin-Milwaukee Institutional Animal Care and Use Committee (IACUC), and were conducted in accordance with National Institute of Health standards on humane treatment of laboratory animals. Animals were anesthetized by isoflurane (1.5%-2% Oxygen) before decapitation by a lab guillotine. The intact brain tissue was extracted for each animal and fixed on an agarose block for slicing. Next, transverse, sagittal, and dorsal brain slices of $500\mu m$ thicknesses were cut using a vibratome (Lancer vibratome Series 1000) while the brain was submerged in Phosphate-buffered saline (PBS) solution (Sigma-Aldrich) and cooled by dry ice. Then, fresh slices were loaded into the optical setup displayed in Fig. 2.2 and scanned one slice at a time. In each round, one slice was cut and scanned during the period the vibratome was cutting the next slice. To minimize the timing of the experiment during which the brain is kept in the freezing solution to preserve the tissue and its optical properties, it is important to synchronize the slicing and the scanning procedures. In our experience, following this protocol, the optical properties did not have significant change during the scanning of each slice, and it took about two hours to complete the whole brain scan.

2.2.2 Measurement procedures

Experimental setup

Based on the IAD model, three different measurements (diffuse reflectance, diffuse transmittance, and ballistic transmittance) are required to extract the complete set of tissue optical properties including μ_a, μ_s, and g [42]. Diffuse reflectance and diffuse transmittance were measured simultaneously using the optical setup 1 and the ballistic transmittance measurements were performed by the optical setup 2 which are both illustrated in Fig. 2.2.

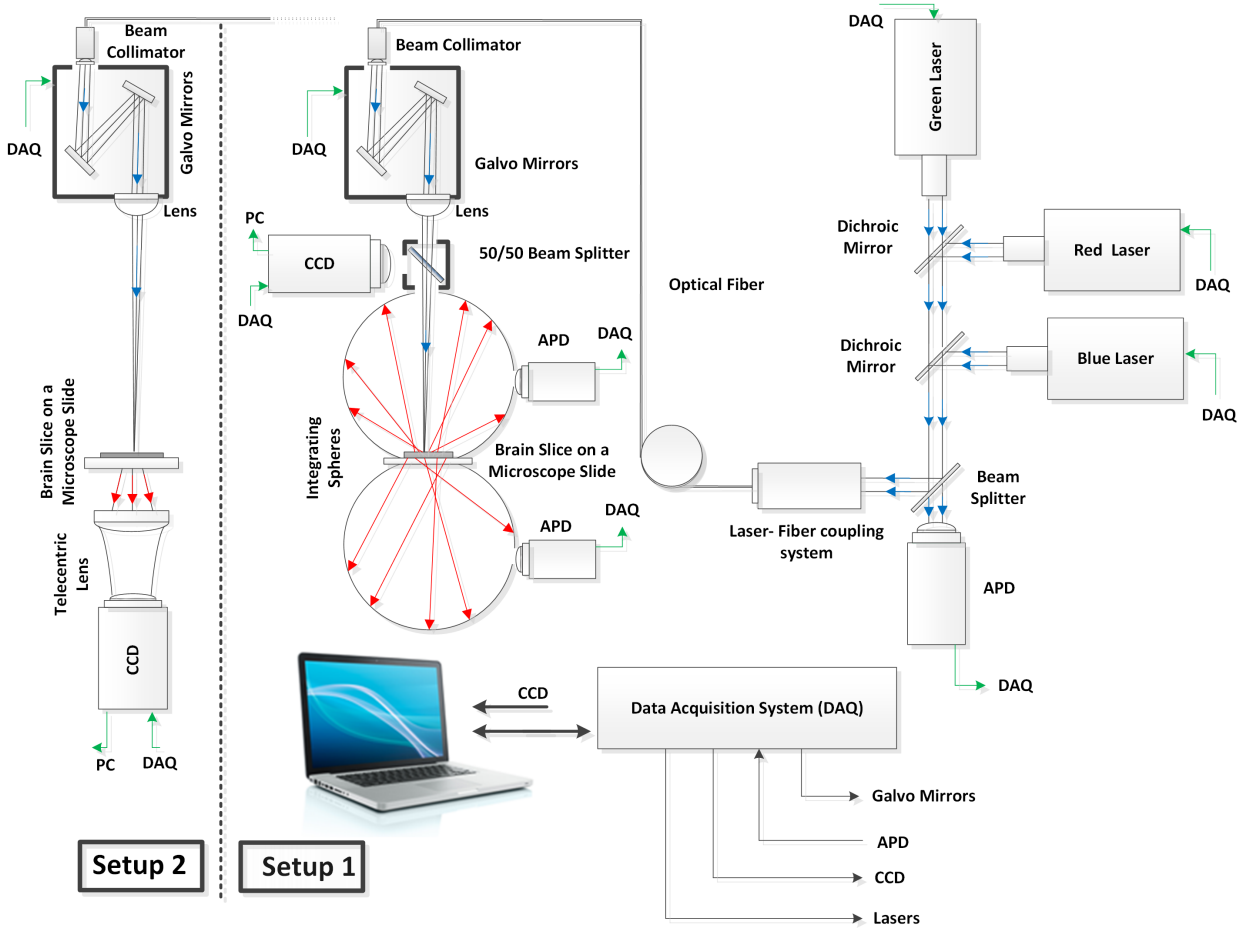

Figure 2.2: Schematic of the experimental setups used to measure diffuse reflected and transmitted light (Setup 1), and transmitted ballistic light (Setup 2).

Diffuse reflectance and diffuse transmittance measurements were acquired using the double-integrating-sphere technique. For this experiment, after preparing a brain slice, the slice was placed between two integrating spheres (one two-port, 6 inch CVI Melles Griot BPS integrating sphere with 1.5 inch sample port diameter, and one 4-Port, 6 inch Spectraflect Integrating Sphere, Newport Corporation with 1 inch sample port diameter) and was scanned using a focused laser beam (with three different wavelengths: blue laser Thorlabs 405nm Laser Diode, green laser Ultralaser 532nm diode-pumped solid-state laser (DPSS), and red laser Thorlabs 635nm Laser Diode) with $200\mu m$ spot size at the focal point on the sample. The diffuse reflected light intensity, $R(r_s^{direct}, r_s)$, was measured using a photodetector (Thorlabs, PDA36A, Si switchable gain detector) that is mounted on the top sphere and diffuse transmitted light intensity, $T(t_s^{direct}, r_s)$, was measured by a second photodetector (Thorlabs, APD110A2/M, avalanche photodetector) that was installed on the bottom sphere. The variables reflectance (M_R) and transmittance (M_T), defined by the amount of light reflected by and transmitted through the sample normalized to the intensity of the incoming light, respectively, were calculated using the following set of equations [42]:

$$M_R \equiv r_{std} \cdot \frac{R(r_s^{direct}, r_s) - R(0,0)}{R(r_{std}, r_{std}) - R(0,0)},$$

$$M_T \equiv \frac{T(t_s^{direct}, r_s) - T_{dark}}{T(0,0) - T_{dark}}. \tag{2.1}$$

In these equations, parameters $R(0,0)$, $T(0,0)$, and T_{dark} are calibration measurements, and r_{std} is the wall reflectance coefficient of the integrating sphere. More details of the calibration and measurement process are available in reference [42].

Evaluating the Performance of the Scanning System With Calibrated Phantom

To evaluate the performance of the proposed approach in extracting optical properties, including the process of making the measurements using the scanning system that is shown in

Figure 2.2 and the application of the IAD algorithm to reconstruct the optical properties, a calibrated phantom with known optical properties was needed. For this purpose, 1% milk was used as a calibrated phantom for which the optical properties were measured by the *added absorber* method [52]. The added absorber method clarifies the reduced scattering and absorption coefficients of a homogenous semi-infinite medium by measuring its diffuse reflectance before and after adding some absorbing material (such as India ink solution) with known absorption coefficient to the medium. Then these measurements are used to solve a system of equations to obtain the reduced scattering and absorption coefficients. In the added absorber method we assume that adding an absorber does not change the scattering coefficient.

In our experiment, we measured the diffuse reflectance of 1%milk (R_{d1}). Then, some India ink was added to the sample to increase its absorption coefficient by $0.1cm^{-1}$ and the same parameter was measured again, (R_{d2}). By having these two measurements, the absorption and reduced scattering coefficients of the original phantom were determined using the grid shown in Figure 2.3. This grid represents the contours of constant absorption and reduced scattering coefficients for the added absorber of $\mu_a = 0.1cm^{-1}$. The first point (marked by $\circledast$) shows the total diffuse reflectance before and the second point (marked by $\odot$) shows the total diffuse reflectance after adding absorber and the intersection determines the properties of the original phantom, which in our case was $\mu_a = 0.033cm^{-1}$ and $\mu_s^{'} = 22.5cm^{-1}$. To validate the accuracy of our system in extracting the optical properties, Agaros gel and the calibrated phantom (1% milk) were mixed to prepare a solid phantom with the thickness of $500\mu m$. By using our technique, the optical properties were estimated to be $\mu_a = 0.025cm^{-1}$ and $\mu_s^{'} = 20.49cm^{-1}$. Compared to the calibrated phantom properties, the reconstructed values show 21% error for the absorption coefficient and 9% for reduced scattering coefficient.

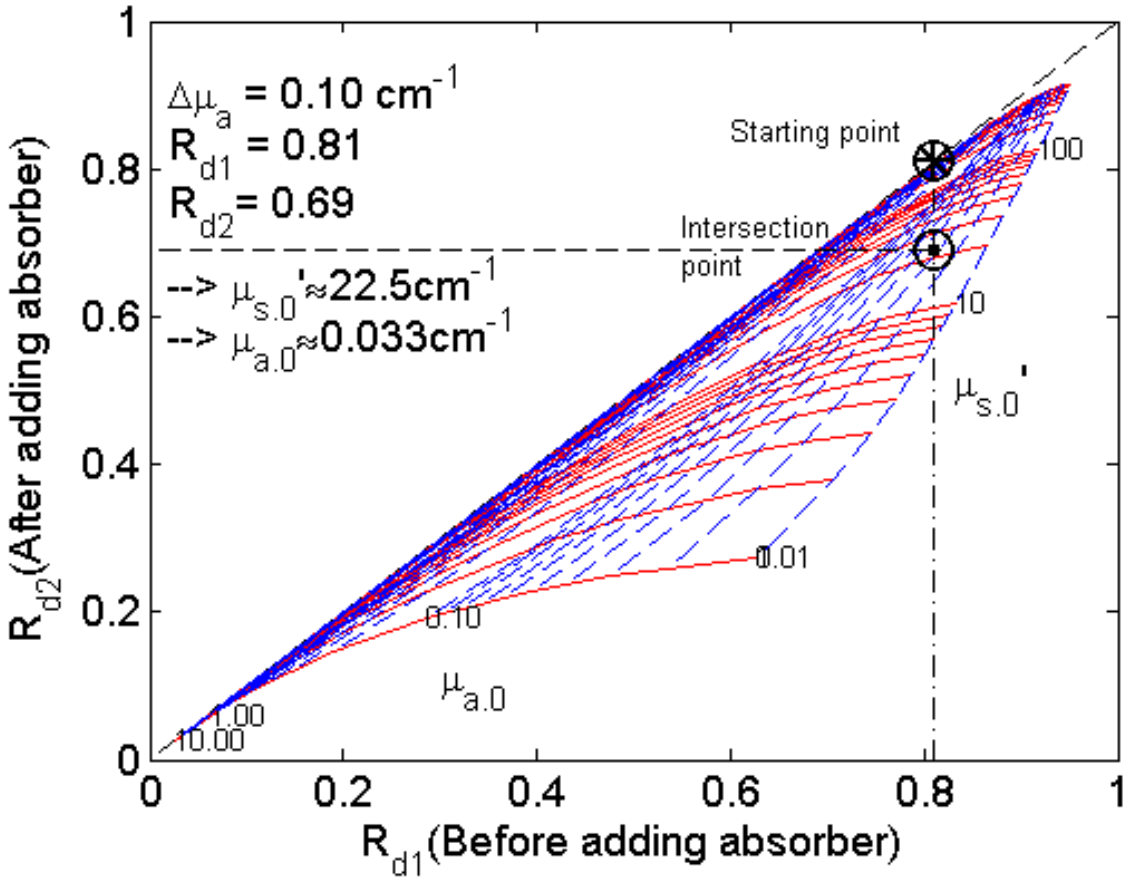

Figure 2.3: Optical properties of a phantom can be determined by measuring total diffuse reflectance before and after adding an absorber with known absorption coefficient. This grid represents the contours of constant absorption and reduced scattering coefficient for the added absorber of $\mu_a = 0.1cm^{-1}$.

Measuring diffused reflectance and transmittance

By using a galvo scanner (Te-Lighting, PT-30K laser scanner galvo system kits), for each brain slice, M_R and M_T variables were measured with a spatial resolution of 3000 points per square centimeter as discussed later. In our measurements, we utilized a charge coupled device (CCD) camera to obtain the geometry of the tissue and used this information to avoid scanning the empty areas around or within the slice to speed up the scanning process (Fig.2.4A). Therefore, it was necessary to register the galvo scanner on the camera output.

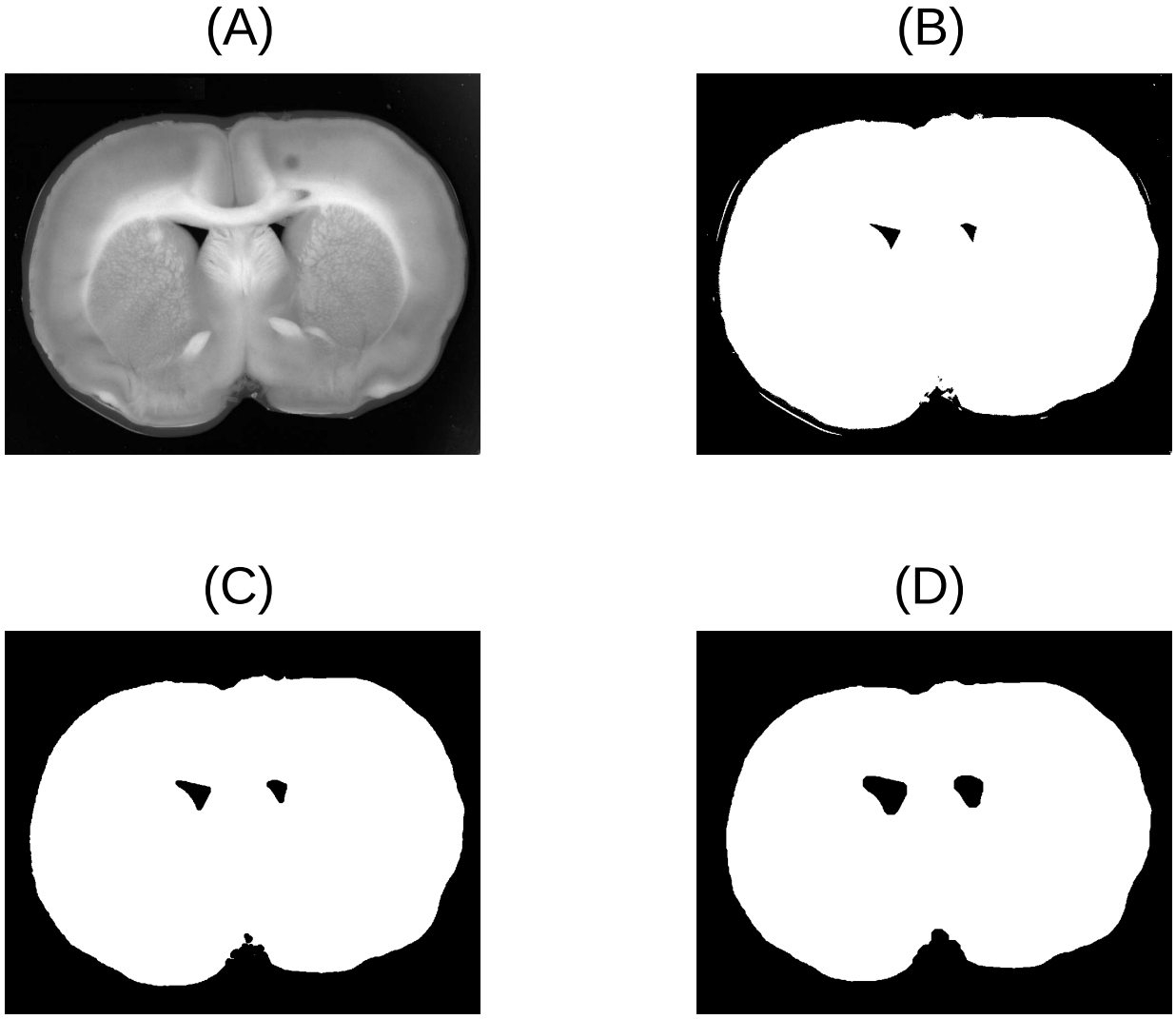

Figure 2.4: (A) Image of a sample brain slice, (B) binary image of (A), resulted images by setting two different radius sizes in *strel* function: (C) R=5, (D) R=13.

The registration was carried out by formulating the relationship between the voltages applied to the scanning mirrors of the galvo system and the coordinates of the laser beam on the tissue, which was recorded by the camera. For this purpose, four different voltages were applied to the scanning mirrors while the camera was monitoring the position of the beam and the system used this information to map the position of the scanning mirrors on the pixels of the CCD camera. The registration needs to be done only once during the whole experiment. Then, for each slice the geometrical shape was obtained by taking the image of

each brain slice by the CCD camera, and this image was used as a mask to separate the tissue from the surrounding background (Fig.2.4B). The developed binary mask defines the region of interest (ROI) that includes just the tissue area. This complex ROI also excludes the edges of the tissue where measurements are not accurate and also footprint of ventricles within each slice. To do that, a MATLAB function, *strel*, with disk-shaped structuring element was used. Figures 2.4(C) and 2.4(D) show the resulted image by setting two different radius sizes in *strel* function. The process of scanning and data acquisition for each slice took about one minute and it was controlled through a custom software developed using LabVIEW [44].

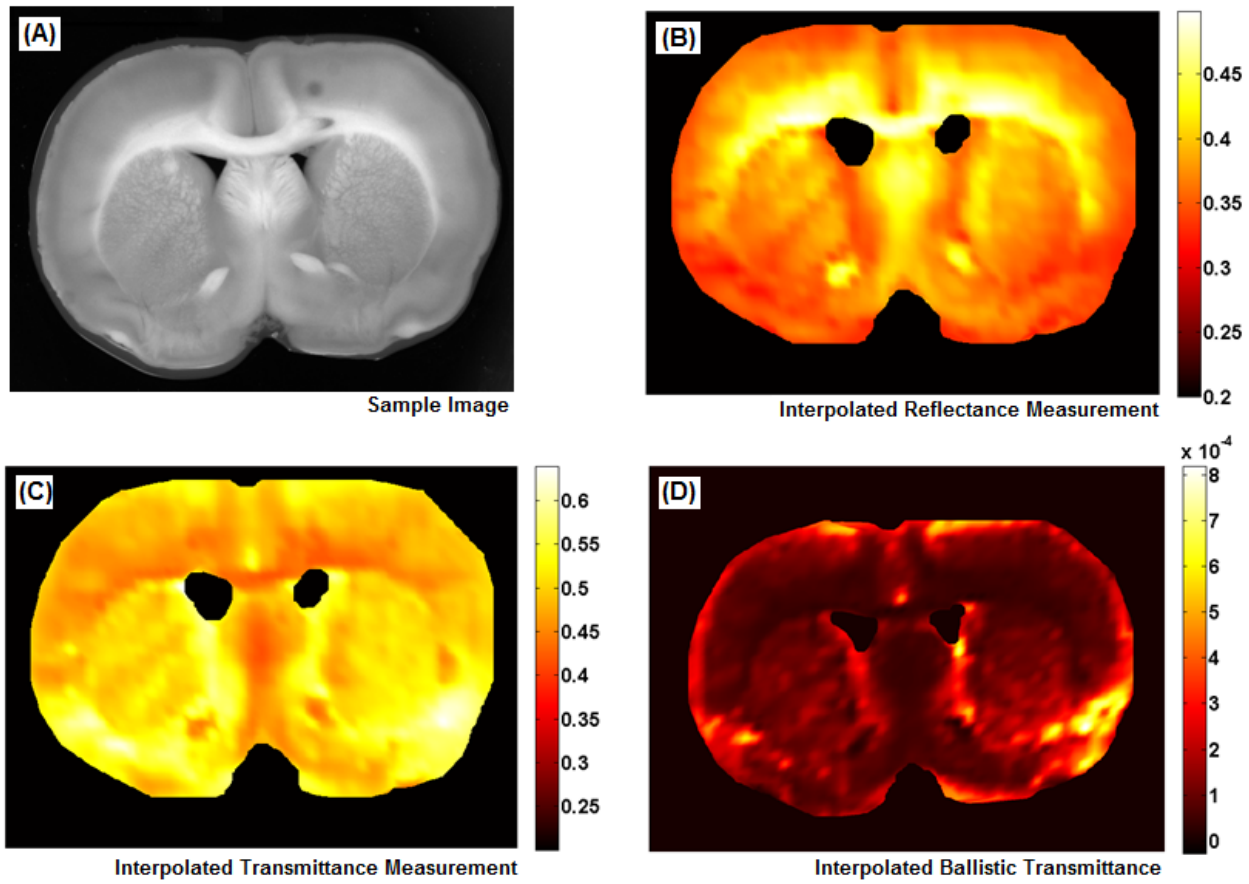

Figure 2.5: Results of the scanning process with the green laser wavelength of $532nm$. Data is presented in arbitrary units. (a) Image of a sample brain slice. (b) Interpolated reflectance measurements. (c) Interpolated transmittance measurements, and (d) Interpolated ballistic transmittance.

Measuring ballistic transmittance

In the ballistic transmittance test, we measured the percentage of the beam that passes through a sample with no scattering or absorption. Traditionally, for this test a photodetector is used to measure the intensity of the beam that passes directly through the sample in combination with an aperture placed in front of the detector that rejects the scatterers rays. For heterogeneous samples such as brain slices, this test can be performed either by moving the sample or possibly the aperture and the photodetector which makes the process quite time consuming. To avoid this problem, we used a telecentric lens system, instead of the aperture, which only passes and projects the collimated portion of the transmitted beam onto a CCD rather than the photodetector [45]. In these experiments each brain slice was placed on a sample holder between the galvo mirrors and the camera and once again the slice was scanned with the same spatial resolution of 3000 points per square centimeter (see Figure 2.2). Similar to the previous measurements, only the tissue area was scanned. By processing the captured frame, the intensity of the ballistic beam was computed by integrating the values of all the pixels within a circular area that has the same diameter as the reference beam-waist. Then, the transmitted ballistic beam ratio was calculated using the following equation:

$$M_U = \frac{I_B - I_N}{I_R - I_N}, \tag{2.2}$$

where I_N is the mean value of the background noise intensity when the laser beam is blocked, I_B is the intensity of the transmitted ballistic beam, I_R in the intensity of the reference beam, and $M_U \in [0, 1]$ is ballistic transmittance. The calibration process, including measuring the intensity of the reference beam (I_R) and the background noise (I_N), needs to be done only once during the whole experiment. To measure the intensity of the reference beam, a predefined voltage was applied to the laser and an image was captured by the CCD camera without any sample in the path. To prevent saturating the camera, a neutral density filter was positioned in front of the CCD sensor to reduce the laser intensity. As described

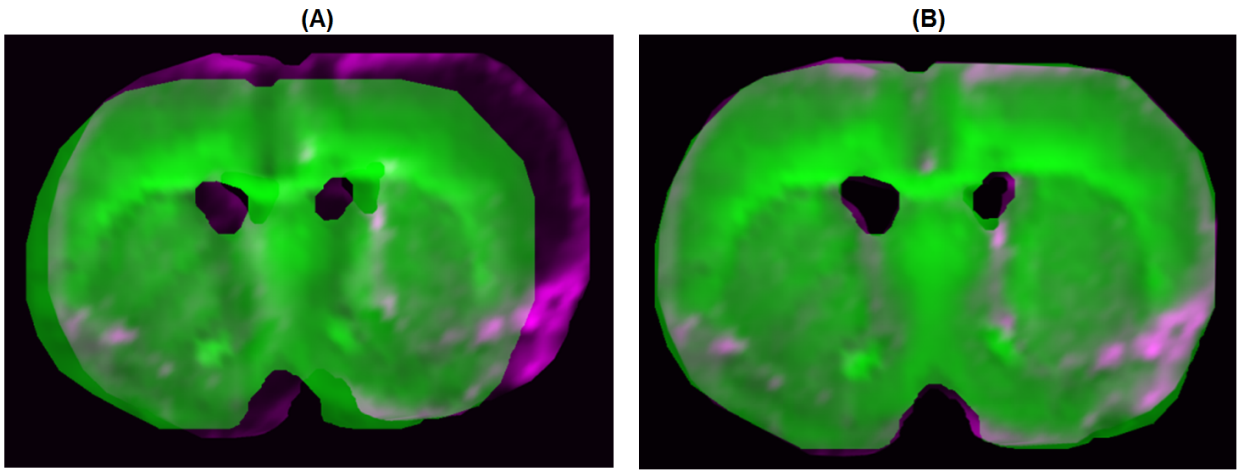

Figure 2.6: Extracted experimental data using setup 1 and 2 (A) before registration, (B) after registration.

earlier, the summation of all the pixel values inside the beam-waist was calculated to obtain the reference beam intensity (I_R).

In Figures 2.5, a sample transverse cut of rat brain and the corresponding interpolated diffuse reflectance, diffuse transmittance and ballistic transmittance measurements are shown for the green laser ($532nm$) measurements. This data is used later to extract the optical properties of the tissue including the absorption coefficient, scattering coefficient and anisotropy factor.

Mapping the experimental data

Since the measurements are made by two different setups, there is a possible displacement between the data collected by these two optical setups (Fig. 2.6). Therefore, before any further process, this displacement should be compensated. We adapted the Matlab command "imregister" from the image processing toolbox (MATLAB 7.14, The MathWorks Inc., Natick, MA, 2012 [43]) to register these two datasets. Once the dataset was prepared and displacement was compensated, this data was fed to the IAD code.

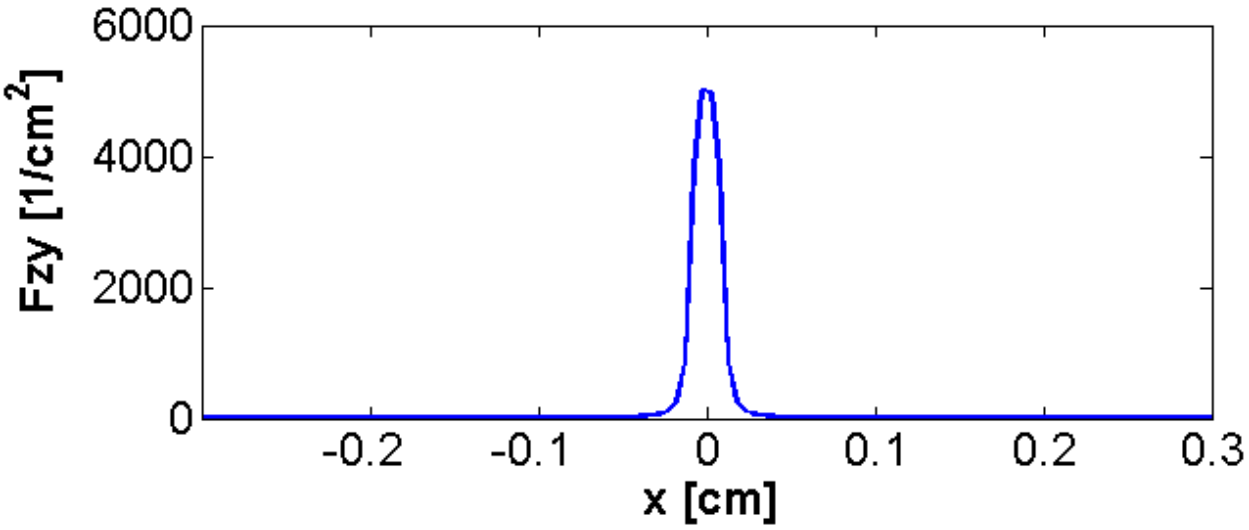

Figure 2.7: Lateral distribution of light transmitted through a slab with thickness of $500\mu m$ and typical tissue optical properties when illuminated with a laser beam of $200\mu m$ diameter.

2.3 Reconstructing optical properties

The IAD method is an iterative algorithm designed to extract the optical properties of a homogeneous sample from the measurements discussed in the previous section. The iterations are initiated with some random values assigned to the optical properties of the medium. Then, in each iteration, the algorithm solves the radiative transport equation [48] to calculate the transmission and reflection of the sample and compares these results with the experimental data. Next, it readjusts the values of the optical properties to minimize the error between the calculations and experimental results and continues this process until convergence. As mentioned before, in the IAD method the assumption is that the sample is a slab with uniform optical properties. To satisfy the homogeneity assumption in IAD algorithm, the scattered light in the tissue should be confined in a small region in which the optical properties remain relatively uniform inside the illuminated area. Our Monte Carlo simulation for light propagation in a slab of turbid medium of thickness $500\mu m$ which has uniform optical properties close to typical values of biological tissue ($\mu_a = 1mm^{-1}$, $\mu_s = 31.6mm^{-1}$ and $g = 0.9$) reveals that the uniform beam which its diameter is $200\mu m$ before the slab,

increases to $\sim 500\mu m$ after passing through this scattering medium as shown in Figure 2.7. Therefore, in our experiments we collected data from discrete sample points and assumed that the optical properties are uniform within the illuminated area for each data point. Then, we used the interpolation to fill the gaps between discrete data points on the tissue.

Once the experimental data is prepared and displacement was compensated, this data was loaded to the IAD code. Since IAD is a time consuming process, not all of the interpolated data points could be used for reconstruction. In our code, we only used a subset of the sampled data points to extract the optical properties via IAD. In the next step, the density of the extracted optical properties was increased by two-dimensional *bicubic interpolation* algorithm [46]. For the brain slice shown in Figure 2.5(a), reconstructed values of the absorption coefficient, reduced scattering coefficient, scattering coefficient and anisotropy factor are shown in Figure 2.8. Another example of such reconstruction that illustrates the heterogeneity of the brain tissue regarding the optical properties is displayed in Figure 2.9.

The similarity principle

The described calculation of ballistic transmittance is admittedly approximate, and a more sophisticated deconvolution of the point spread function in angle space of transmitted light versus variable sample thickness would more appropriately define the μ_s and g values. However, when $g >> 0.5$, the spatial distribution of light is dominated by the lumped parameter $\mu_s^{-1} = \mu_s(1-g)$, which is reliably specified by the integrating sphere measurements, even in the region of non-diffuse light that occurs near the probe tip. The similarity principle says that light distributions are specified by the lumped parameter $\mu_s^{'} = \mu_s(1-g)$. While widely understood for diffuse light propagation, it is not widely appreciated that this principle also pertains to the non-diffuse regime near the entry point of light into tissue, where diffusion theory is not accurate. Figure 2.10 shows the pattern of fluence rate near the position where light is launched into a tissue. The reduced scattering coefficient, $\mu_s^{'}$, is kept constant at

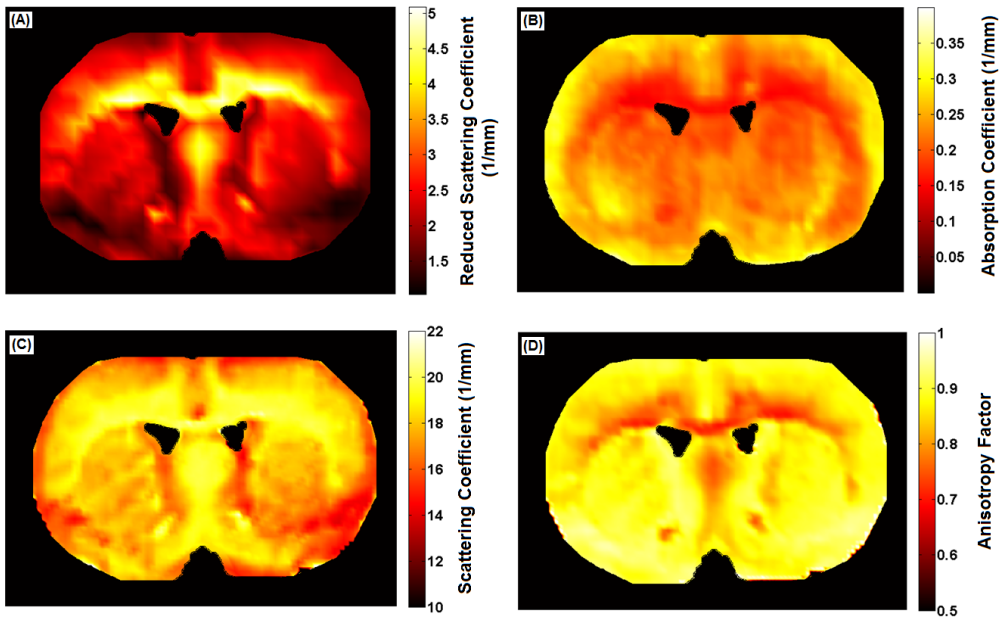

Figure 2.8: Extracted optical properties of the rat brain slice produced by IAD algorithm which is applied to the raw data shown in Figure 2.5, (a) Reduced scattering coefficient, (b) Absorption coefficient, (c) Scattering coefficient, (d) Anisotropy factor.

$10cm^{-1}$, while the value of g is varied from 0.8 to 0.9 to 0.95, and $\mu_s = \mu_s^{'}/(1-g)$. The light distributions are basically the same for all cases. As the g values drops below 0.5, there is an on-axis penetration of light that develops. Figure 11 for $g = 0.8$ shows the early formation of this on-axis penetration. For tissues, which typically present $g \geq 0.8$, the similarity principle means predictions of light distribution depend on $\mu_s^{'}$ and are not strongly dependent on the accuracy of μ_s and g. Therefore, the properties of μ_s and g deduced here, even if slightly in error, will still yield reliable predictions of light distribution in the tissue, even near the light source.

2.4 3D Monte Carlo simulation results

In order to investigate the impact of tissue heterogeneities and different light source configurations on the distribution of light inside tissue, a three-dimensional Monte Carlo toolbox

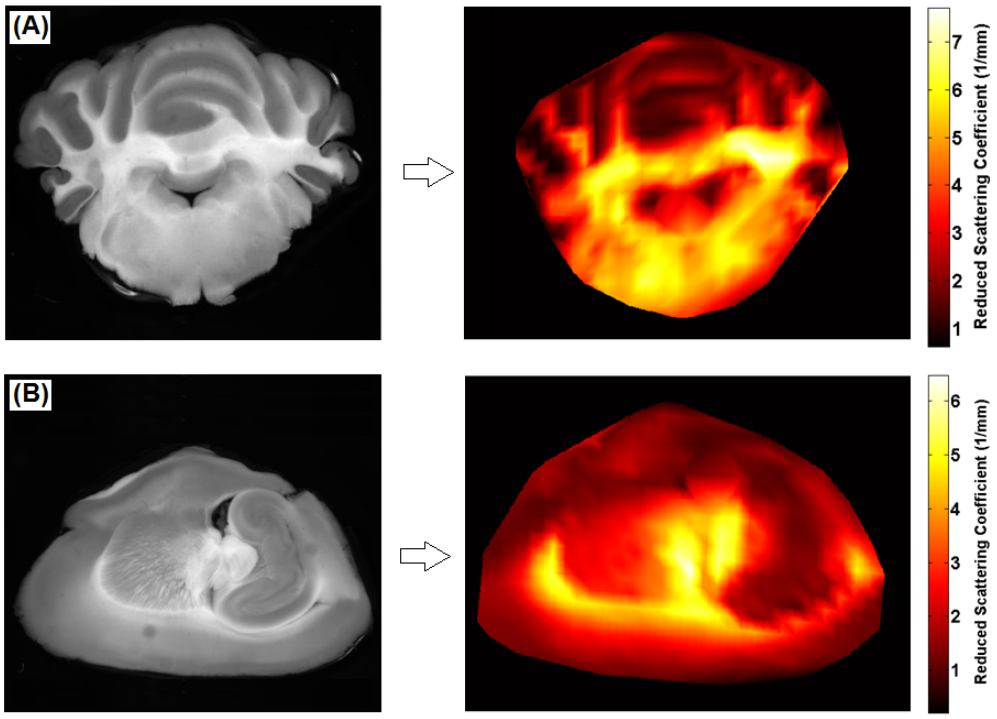

Figure 2.9: Extracted reduced scattering coefficient at $532nm$ for a rat brain tissue, (A) Transverse cut, (B) Sagittal cut.

was prepared and linked to the developed database of the rat brain tissue optical properties. Results of these simulations are presented in the following sections.

2.4.1 Impact of brain tissue heterogeneity on light distribution

For any inhomogeneous medium, such as the brain tissue, we logically expect to observe a different or possibly more complex light distribution pattern compared to the light distribution pattern in a uniform medium of the same volume. To investigate the effect of tissue heterogeneities on light distribution in the brain, we simulated the photon transport process inside the tissue using our three-dimensional Monte Carlo code and compared our results with the dual homogenous medium. In both simulations, all photons are launched from a uniform source with diameter of $150\mu m$ which is placed at the specified area marked in Figure 2.11(A). For the dual homogenous model, the mean value of the optical properties

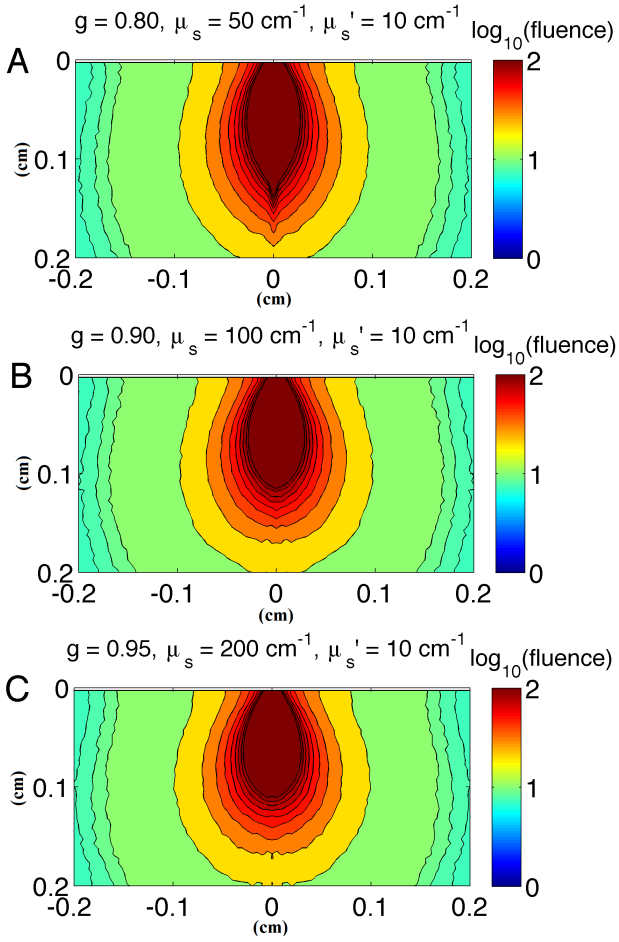

Figure 2.10: The similarity principle is pertinent within the region of non-diffuse light propagation near the light source. Holding $\mu_s^{'}$ constant at $10cm^{-1}$, the relative fluence rate $(1/cm^2)$, is similar despite changes in g and μ_s. (A) g = 0.80, $\mu_s = 50cm^{-1}$, $\mu_s^{'} = 10\ cm^{-1}$. (B) g = 0.90, $\mu_s = 100cm^{-1}$, $\mu_s^{'} = 10\ cm^{-1}$, (C) g = 0.95, $\mu_s = 200cm^{-1}$, $\mu_s^{'} = 10cm^{-1}$. Figure shows iso-fluence-rate contour lines.

of the whole tissue were assigned as the optical properties of a virtual uniform medium. On the other hand, for the heterogeneous test, we used the extracted database of the optical properties. Optical properties of the tissue in the region are displayed in panels (B)-(D). An example of the difference between the light distributions in these two structures are shown in Figure 2.11(E) and (G) and the corresponding contour maps of the light distributions are displayed in panels (F) and (H). Furthermore, light distributions along an arbitrary axial line is displayed in Figure 2.11(I). This result highlights the effect of tissue heterogeneity on

light distribution which, in this experiment, has caused some considerable asymmetry in the distribution pattern in a way that the intensity of light at the distance of about $2.50mm$ on one side is more than 3 times stronger than the light intensity at the same distance from the center of the source on the other side. The curve in Figure 2.11(J) shows the difference between the two distributions that is caused by the heterogeneity in absorption, scattering, and anisotropy factor. Based on our observation, in short distances in the brain tissue the difference between the light distribution in the homogeneous approximation and the actual heterogenous model is minimum. However, as the distance from the source increases, this difference grows. Therefore, the heterogeneity effect in the design of optogenetic experiments is more essential once highly sensitive opsins, such as step-function opsin [23], are used. The reason is that in these cases even low intensity light that reaches to deeper regions of brain tissue can stimulate the cells. The impact of the tissue heterogeneity on the axial distribution of light is also significant. Figure 2.12 shows the simulation results in which the axial penetration depth at two different regions, marked by points 'A' and 'B' in the figure, are compared. In this case, at the depth of $2mm$ from the fiber tip, light fluence rate for point 'B' is almost 5 times larger than point 'A'.

2.4.2 Impact of physical parameters of the source on light distribution

Choosing the proper light delivery mechanism is important in optogenetic experiments particularly when the application demands precise stimulation of some target areas. Optical fibers are widely used for optogenetic stimulation of deep brain objects *in-vivo* [20, 30, 31, 32]. Physical parameters of the optical fiber, such as core diameter and numerical aperture (NA), have certain impact on the beam profile and its distribution in the medium. Here, Monte Carlo simulation was used to investigate the light propagation along the tip of the optical fiber for different fiber parameters and different wavelengths. In Figure 2.13(B), the axial fluence rate (light fluence rate along 'z' direction) for $405nm$ wavelength is shown for dif-

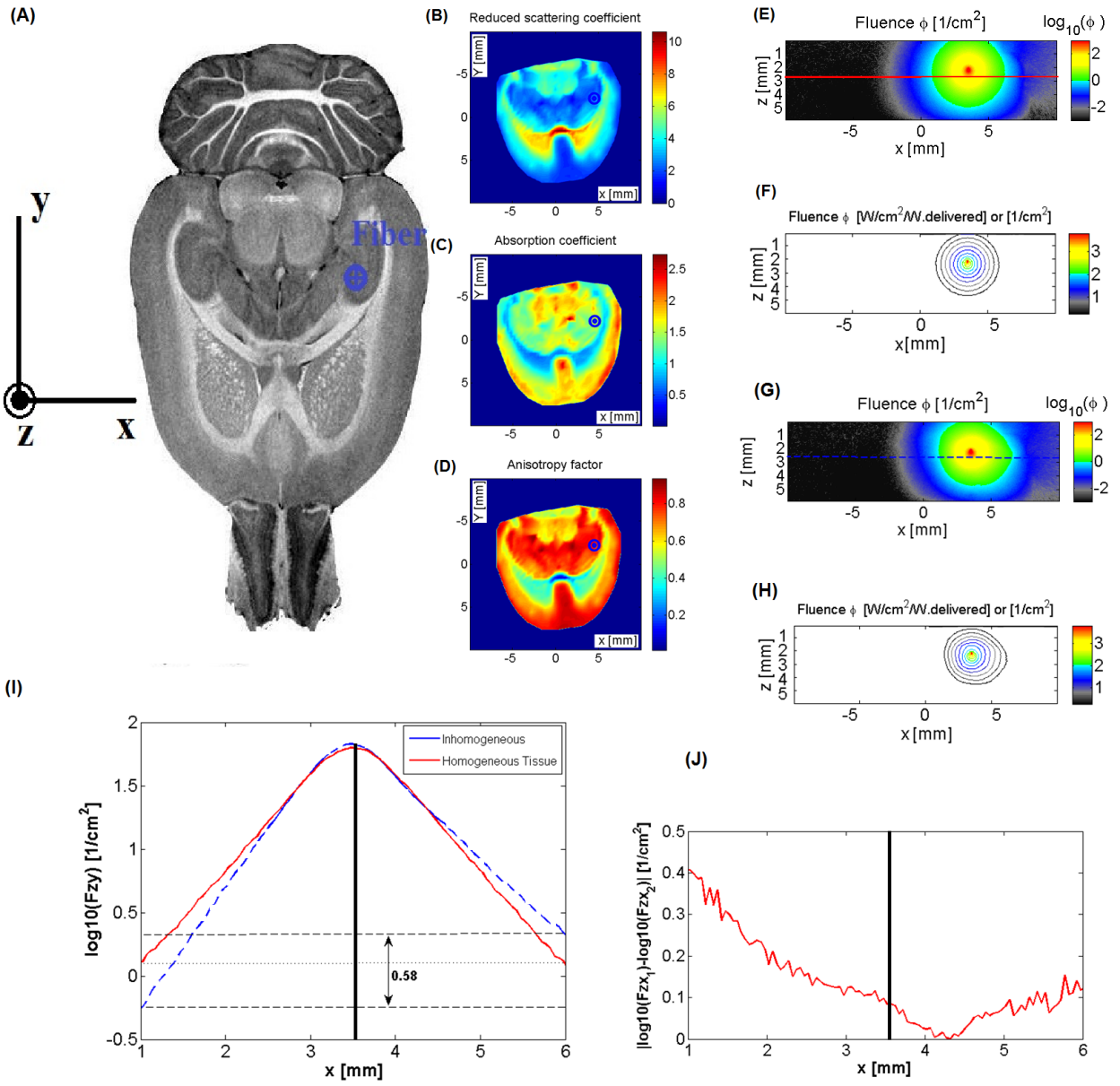

Figure 2.11: (A) An optical fiber of $150\mu m$ diameter is placed on the marked area inside the tissue to launch a uniform beam. The three-dimensional Monte Carlo simulations are run by launching 10 million photons. Optical properties of the tissue in the region are displayed in (B-D) for a blue laser at $405nm$. (E) Two-dimensional representation of the light distribution in the XZ plane (F_{XZ}) for the homogeneous brain tissue, (F) Contour map of the light distribution in the homogeneous brain tissue, (G) Two-dimensional representation for the distribution of light in the XZ plane (F_{XZ}) for the inhomogeneous brain tissue, (H) Contour maps of the light distribution in the inhomogeneous brain tissue, (I) Lateral fluence rate of the light along the 'X' axis for the inhomogeneous and homogenous brain tissue which shows considerable difference between the two distributions. Distribution of the light for homogenous tissue along the 'Z' axis shows almost an identical change in both directions far from the fiber position (solid curve) while the light distribution has become asymmetric as a result of the tissue heterogeneity (dashed curve). (J) The different between distribution of light in the homogeneous and inhomogeneous tissue.

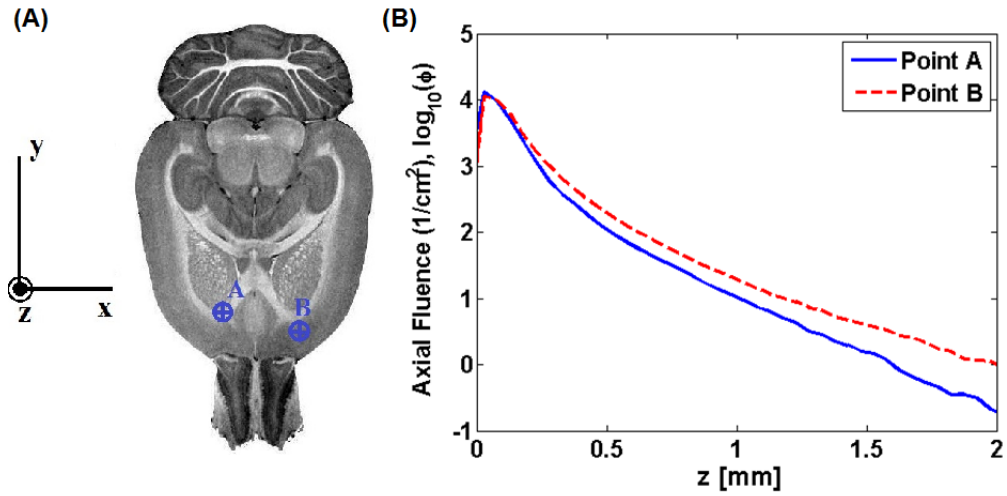

Figure 2.12: (A) Optical fiber with $100\mu m$ diameter is placed on the marked regions in the tissue, (B) Comparing the axial fluence rate along 'z' axis for point 'A' and 'B'. The difference between the attenuation coefficients in these two regions has caused significant difference between the axial penetration depth of light at these two positions for a blue laser at $405nm$.

ferent fiber diameters, $200\mu m$, $150\mu m$, $100\mu m$ and $50\mu m$. The simulation results show that for the same optical power, the axial fluence rate decreases by increasing the fiber diameter. On the other hand, it seems that reducing the diameter of the fiber below $100\mu m$ does not have significant impact on the axial fluence rate. Figure 2.13(C) demonstrates the axial fluence rate for a $100\mu m$ diameter optical fiber with different numerical apertures including 0, 0.1, 0.22 and 0.39. According to these results, light intensity drops faster along the axial direction for the optical fibers which have larger numerical aperture. Panel (D) in the same figure represents the impact of the wavelength on light distribution. Here, for shorter wavelengths the attenuation rate is higher as expected [33]. For the blue light (dashed line) the attenuation is higher and the intensity drops a lot faster than the green and red light. A comparison of the axial attenuation between the Gaussian and uniform light source is presented in panel (E). This data shows that the Gaussian beam has higher fluence rate.

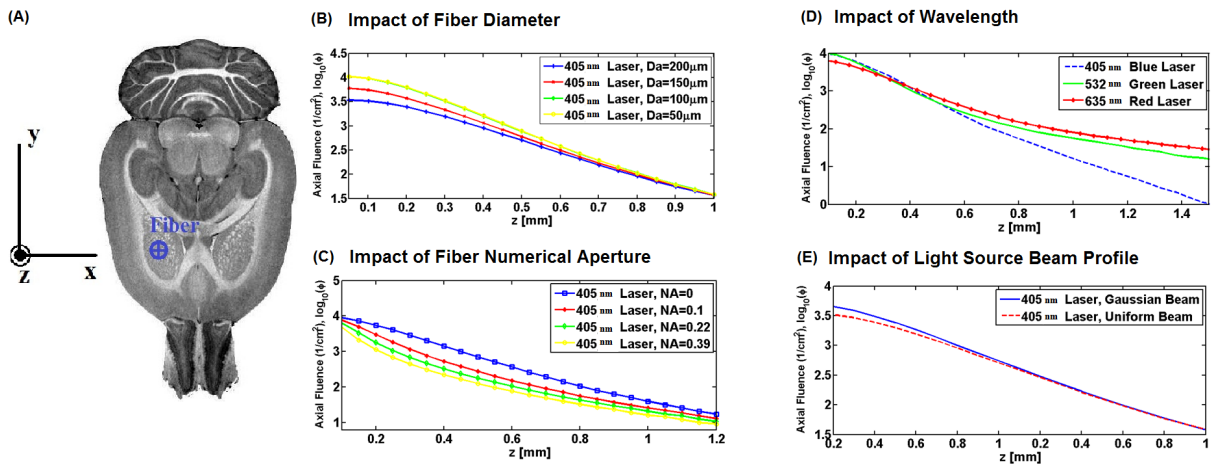

Figure 2.13: (A) An optical fiber is placed on the marked area and the Monte Carlo simulation software is used to investigate the effect of source parameters on light distribution inside the brain tissue for a blue laser at $405nm$, (B) effect of the fiber diameter, (C) effect of fiber numerical aperture (NA), (D) spectral response, (E) effect of the beam profile on the axial distribution of light.

2.4.3 Preservation of the patterned stimulations during optogenetic experiments [60]

Light delivery for optogenetic stimulation is usually performed by implanting optical fiber(s) inside the tissue [31, 32]. Spatial light modulators (SLM) and digital micromirror devices are also used to generate two or three-dimensional stimulating patterns in the brain superficial areas [9, 54]. When the tissue is stimulated by light patterns that are projected on the tissue surface, the question is to what extent this structured distribution of light is preserved at different depths in the brain tissue? To answer this question, we modeled lighttissue interaction using a three-dimensional (3-D) Monte Carlo software [49, 50]. In these simulations, the cortical tissue was modeled by the reduced scattering coefficient, $\mu_s^{'} = 32cm^{-1}$ and absorption coefficient $\mu_a = 9cm^{-1}$ for 445nm blue wavelength and $\mu_s^{'} = 19cm^{-1}$ and $\mu_a = 1cm^{-1}$ for the 635nm red light. Monte Carlo simulations were performed by tracing 50 million photons in the tissue. In these tests, tissue was stimulated by patterns of light that resemble 1-D spatial frequencies: 1.0 lp/mm to 2.0 lp/mm. Fig. 2.14(A) shows the distribution of light

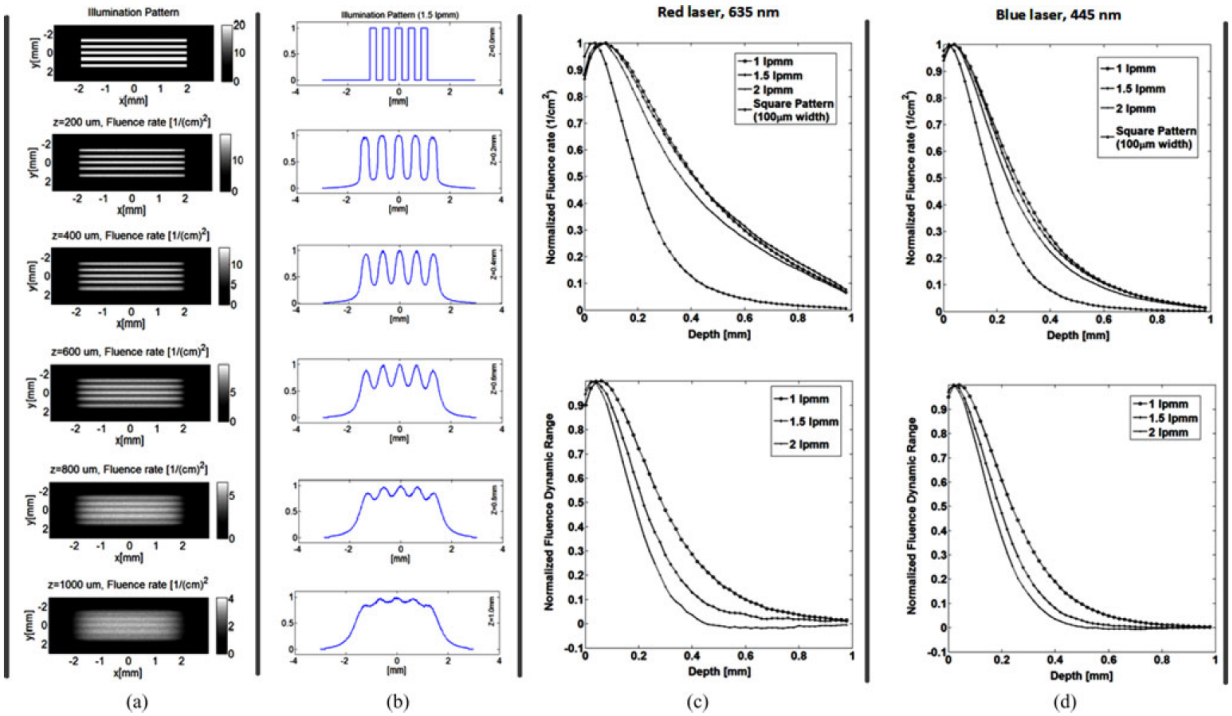

Figure 2.14: Preservation of the projected patterns in the tissue is studied by three-dimensional Monte Carlo simulations: (a) distribution of light at multiple depths ranging from 200 to 1000μm are shown when the tissue is stimulated by a 1-D spatial frequency of 1.5 lp/mm, (b) normalized curves of light distribution at different depths. The dynamic range of fluctuations drops significantly as light penetrates deeper inside the tissue, (c) and (d) maximum intensity of light and the dynamic range of the fluctuations are plotted for different spatial frequencies, 1.0 lp/mm, 1.5 lp/mm, and 2.0 lp/mm for two different wavelengths, 445nm blue light and 635nm red light [60].

at different depths when the projected pattern resembles a square wave of frequency 1.5 lp/mm. Because of the scattering, the dynamic range of fluctuations drops significantly and the distribution of light becomes relatively uniform at the depths 600–800μm in the cortical tissue. This effect is more visible if we plot light distribution curves for different depths as shown in Fig. 2.14(B). In this figure, we see some fluctuations around a plateau; however, the dynamic range of these fluctuations, which is a measure of the pattern preservation, drops as depth increases. The rate of drop for the dynamic range and the maximum light intensity at different depths for two wavelengths (445 and 635nm) are shown in panel (C) and (D). Based on these simulations, structured patterns such as the tested 1-D spatial frequencies

are reasonably preserved to about $500\mu m$ inside the tissue which covers considerable portion of the cortex in small rodents including the optogenetic mice.

2.5 Effect of Blood Vessels on Light Distribution During Optogenetic Stimulation of Cortex

This section is reproduced with some adaptations from the manuscript [61]:
Mehdi Azimipour, Farid Atry, and Ramin Pashaie, "Effect of blood vessels on light distribution in optogenetic stimulation of cortex," Opt. Lett. 40, 2173-2176 (2015). doi:10.1364/OL.40.002173
http://dx.doi.org/10.1364/OL.40.002173

2.5.1 Introduction

One aspect in tissue light interaction that was not discussed in the previous chapter is the effect of blood on light distribution and penetration. Previous experiments have shown that mammalian blood has relatively high absorption and scattering coefficients and incorporating the optical properties of the blood in the models potentially improves the precision of the predictions. Our approach to include the effect of blood vessels on light distribution, both single fiber and patterned illumination setups, is to employ optical coherence tomography, to scan the tissue and generate angiograms, which provide insight to the details of blood distribution in the tissue under test. Next, integrate this angiogram into the extracted optical properties of brain tissue, which is used for Monte Carlo simulations. The main objective of this section is to illustrate the impact of blood vessels on light distribution profile and penetration depth in the brain tissue during optogenetic stimulation. The details of the effect of blood vessels on light distribution in optogenetic stimulation of cortex is given in the following section.

2.5.2 Angiogram of the cortex's blood vessels

Most of the models developed for predicting light distribution during optogenetics stimulation are based on measurements with brain slices [35, 55]. As a result, the impact of

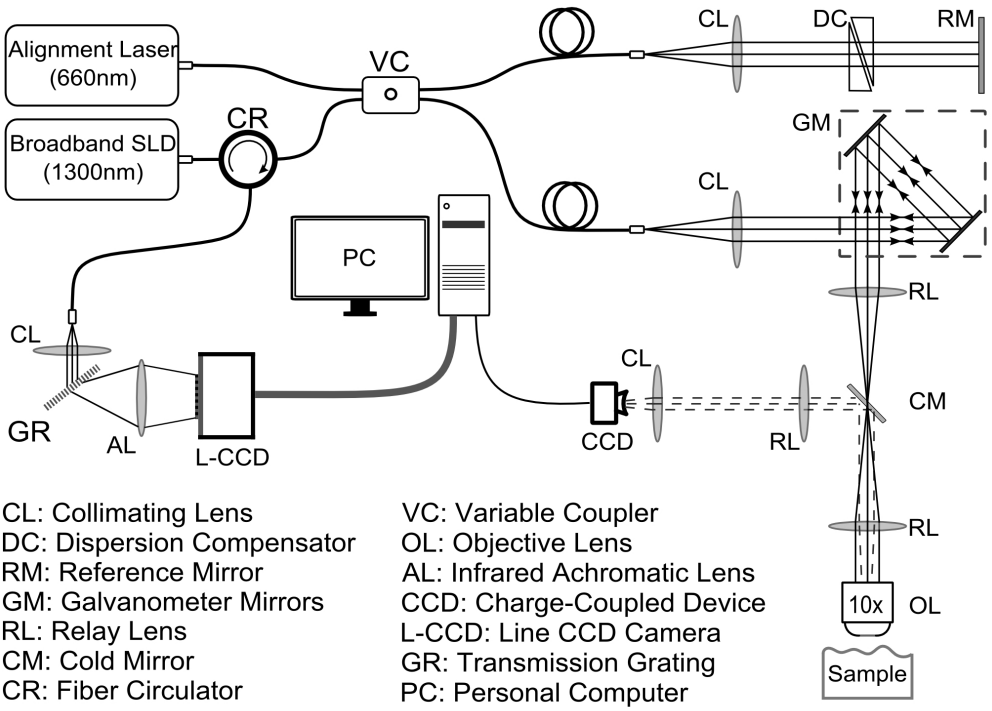

Figure 2.15: Schematic of the SD-OCT setup: A broadband infrared source (center wavelength: 1300nm, bandwidth: 170nm) was used to scan the cortical tissue of live head-fixed rats.

blood vessels on light distribution, which is potentially a major factor in *in-vivo* studies, is neglected. In practice, blood has relatively large absorption coefficient particularly in the visible spectrum where the main optogenetic proteins have maximum sensitivity. The sample in this study was rat's cortex. In our experiments, we started by extracting the optical properties of the cortical tissue at three different wavelengths, 405nm, 532nm and 635nm. We used a double-integrating sphere setup to scan 500μm brain slices and ran standard diffuse reflectance, diffuse transmittance, and ballistic transmittance tests to collect the raw data [41, 55]. This data was fed to an inverse-adding-doubling (IAD) algorithm to obtain optical properties of the tissue, including absorption coefficient (μ_a), scattering coefficient (μ_s), and anisotropy factor (g) [42, 53], Table 2.1. In our next step, we used our custom-made spectral-domain optical coherence tomography (SD-OCT) scanner to image cerebral blood vessel of live animals in the same cortical areas. A simplified schematic of the scanner is displayed in Figure 2.15. In the structure of this SD-OCT scanner we used a 1300nm su-

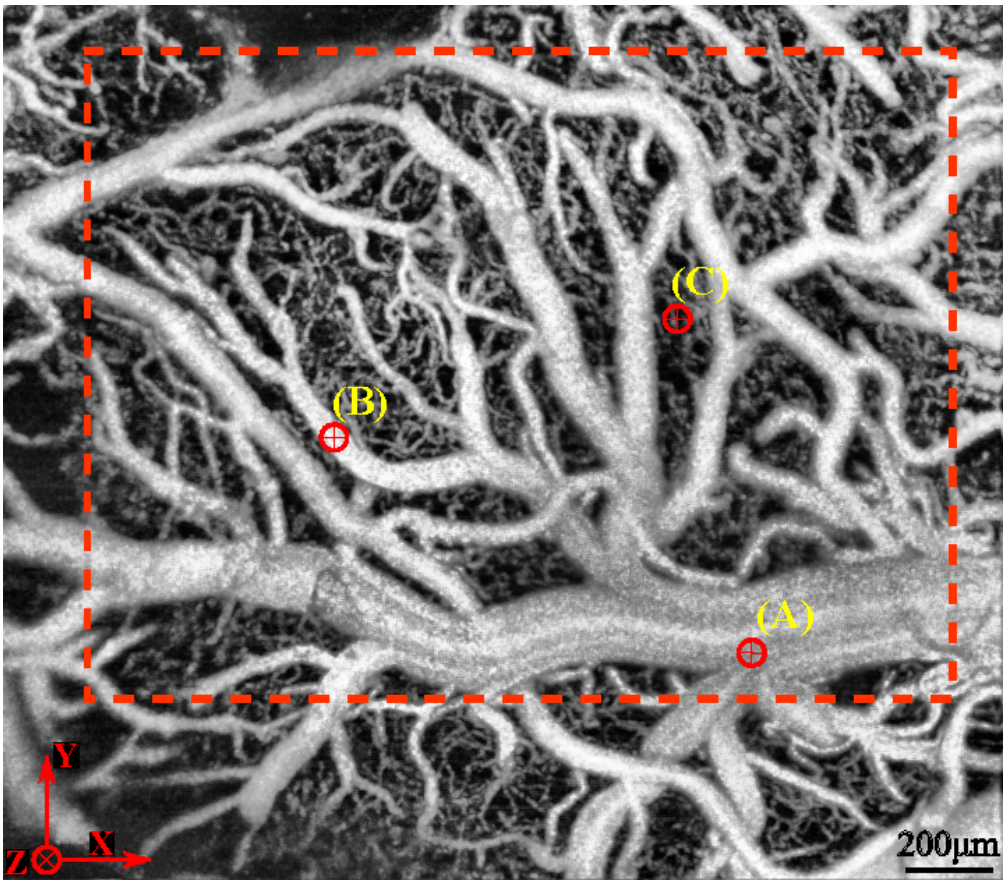

Figure 2.16: Maximum intensity projection of the volume angiogram captured by the SD-OCT scanner from the cortical tissue of a head-fixed live rat.

perluminescence laser diode (SLD) with $170nm$ bandwidth. This infrared center wavelength is chosen since light scattering in the brain tissue around this wavelength is relatively low. The wide bandwidth of the source helps to reduce the coherence length of the source and provide high axial resolution. The lateral and axial resolutions of the scanner are $5\mu m$ and $5.6\mu m$, respectively, which is enough to capture most vessels and small capillaries within the field of view. The imaging depth of the scanner in air is around $1.8mm$.

To image cerebral vascular networks, $2.4mm \times 2.4mm$ field of view was raster scanned at the speed of $40k$ line-scans per second and density of 312×312 axial scans per mm^2. Each cross-section was scanned 10 times. Motion artifacts were detected by cross-correlation maximization [56] and compensated. By detecting the changes between the SD-OCT recordings from each lateral position, cross-sectional angiograms were obtained [57, 58]. At each posi-

Table 2.1: Optical properties of the brain cortical tissue and blood at three different visible wavelengths. The anisotropy factor g is 0.9 which is shown to be a reasonable approximation for the cortical tissue [53, 55].

	μ_a (1/mm)	μ_s' (1/mm)
Wavelength(nm)	405, 532, 635	405 , 532 , 635
Blood	102, 22.5, 0.2	0.38, 1.15, 1.38
Brain	0.9, 0.30, 0.1	3.2 , 2.30, 1.9

tion, the angiogram was normalized by the average of the SD-OCT intensity at that pixel to compensate for the intensity variations across the tissue. Noise was reduced by applying a three-dimensional smoothing filter to the stack of these cross-sectional angiograms. The angiography data obtained by the SD-OCT was then converted to a binary volumetric mask by applying a threshold filter to the data to segment blood vessels and separate them from the brain tissue. A typical maximum intensity projection (MIP) of a scanned volume is shown in Figure 2.16.

2.5.3 Predicting light distribution in a complex model of cortical tissue

In order to predict the light distribution profile during optogenetics stimulation, we filled the gaps between blood vessels in the SD-OCT angiogram with the cortical tissue characterized by the optical properties which were measured earlier. Next, we used our three-dimensional Monte Carlo software [49, 50] to simulate light propagation in this inhomogeneous turbid medium. In the developed volumetric model of the rat brain, each voxel was categorized as brain tissue, blood, or the surrounding air on top, and appropriate optical properties were assigned to each category.

In the Monte Carlo simulations, displayed in Figure 2.17(A), a $100\mu m$ diameter optical fiber with numerical aperture of $NA = 0.37$ is delivering light with three different wavelengths into the tissue at the spot marked as point **B** in Figure 2.16. Point **B** is intentionally

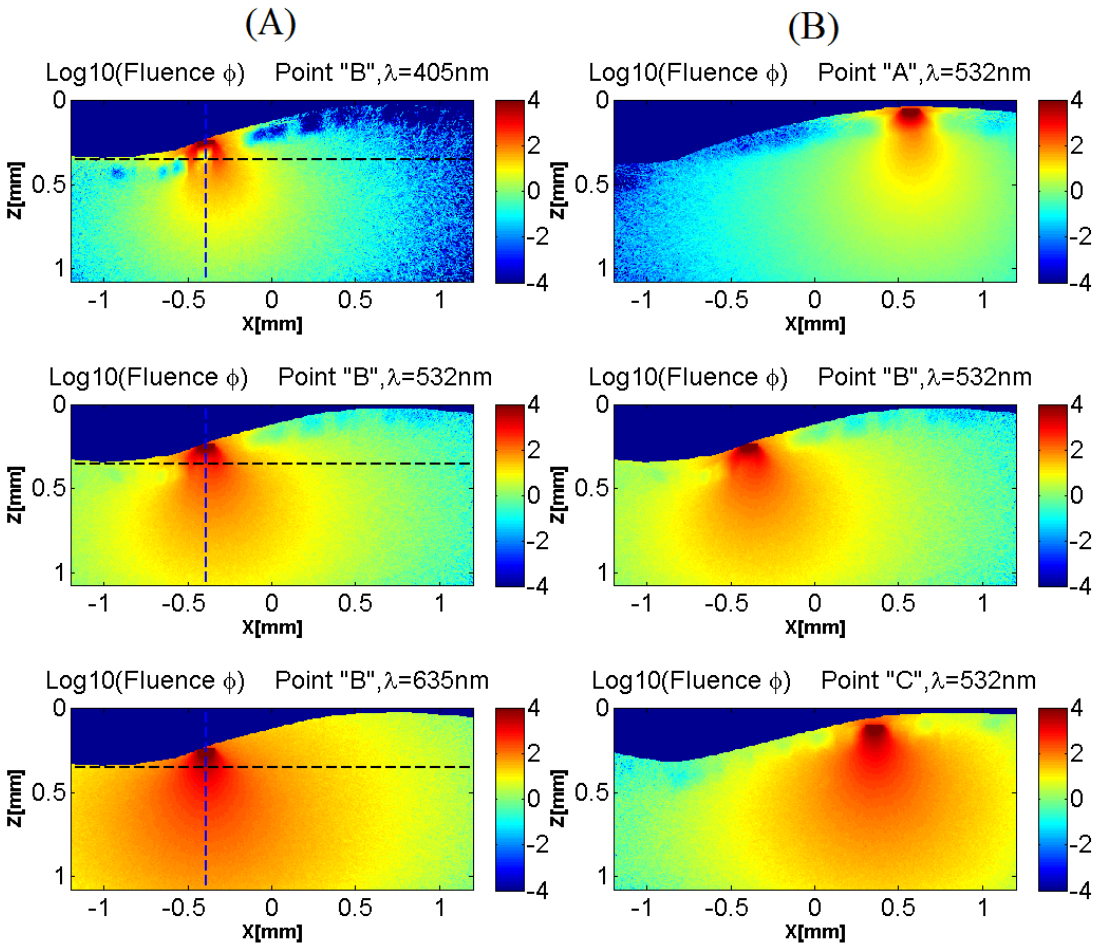

Figure 2.17: Monte Carlo simulation results when a $100\mu m$ diameter fiber, $NA = 0.37$, was launching light into the cortical tissue. (A) Impact of blood vessels on light distribution for wavelengths: $405nm$, $532nm$ and $635nm$, at point 'B'.(B) Impact of the fiber position on light distribution profile for the $532nm$ green laser.

chosen in the vicinity of medium size (about $50\mu m$) vessel. For the $405nm$ wavelength light, where blood has high absorption coefficient, the vessel almost completely blocks light penetration and the light intensity drops abruptly. Penetration depth increases for larger wavelengths. Panel (B) in Figure 2.17(A) illustrates the impact of blood vessel diameter on light distribution for $532nm$ green laser. At point **C** where no major blood vessel is blocking the the beam and only small capillaries are absorbing light, the penetration depth is significantly larger than point **A** where a main blood vessel is absorbing most of the optical power. The quantified data are shown in Figure 2.18 which displays the change in the light

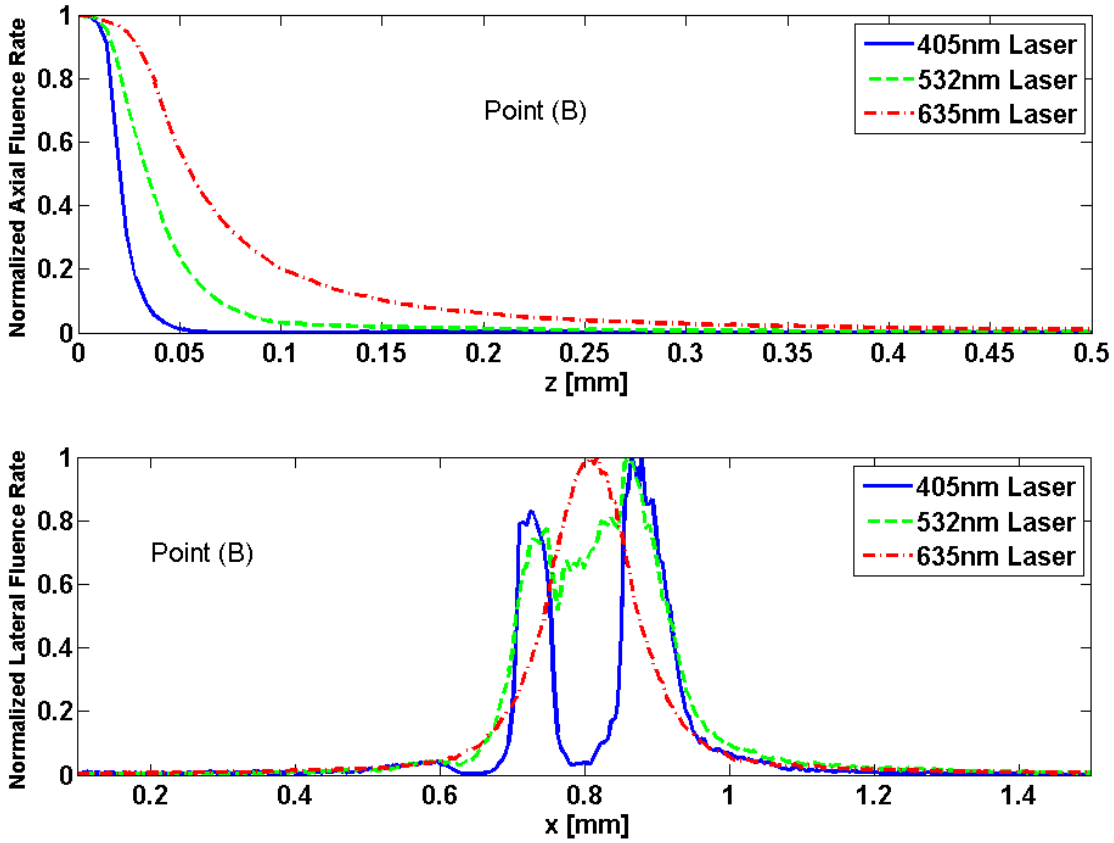

Figure 2.18: Penetration depth and distribution profile change significantly when a major vessel is close to the light injection site. Quantified data along the (A) horizontal and (B) vertical axes marked in figure 2.17(A).

intensity along a vertical and horizontal lines marked in Figure 2.17(A) for three different wavelengths. Figure 2.19 displays the comparison between the new approach in which the effect of blood vessel is included in the model compared with the Kubelka-Munk (KM) which has been used to estimate the penetration depth of light pulses for optogenetic stimulation. Based on this data, the effect of capillary arbor on penetration depth at positions slightly farther away from the tip of the fiber is minimum. The only observable difference is at the vicinity of the fiber tip. Nonetheless, medium and larger vessels cause significant change in penetration depth which should be considered in the design of experiments.

Cortex is known as the center of high-level information processing in the brain. Complex dynamics of cortical circuits and interconnected networks are used to process data, extract features, produce sparse representations, and generate brain rhythms. This information

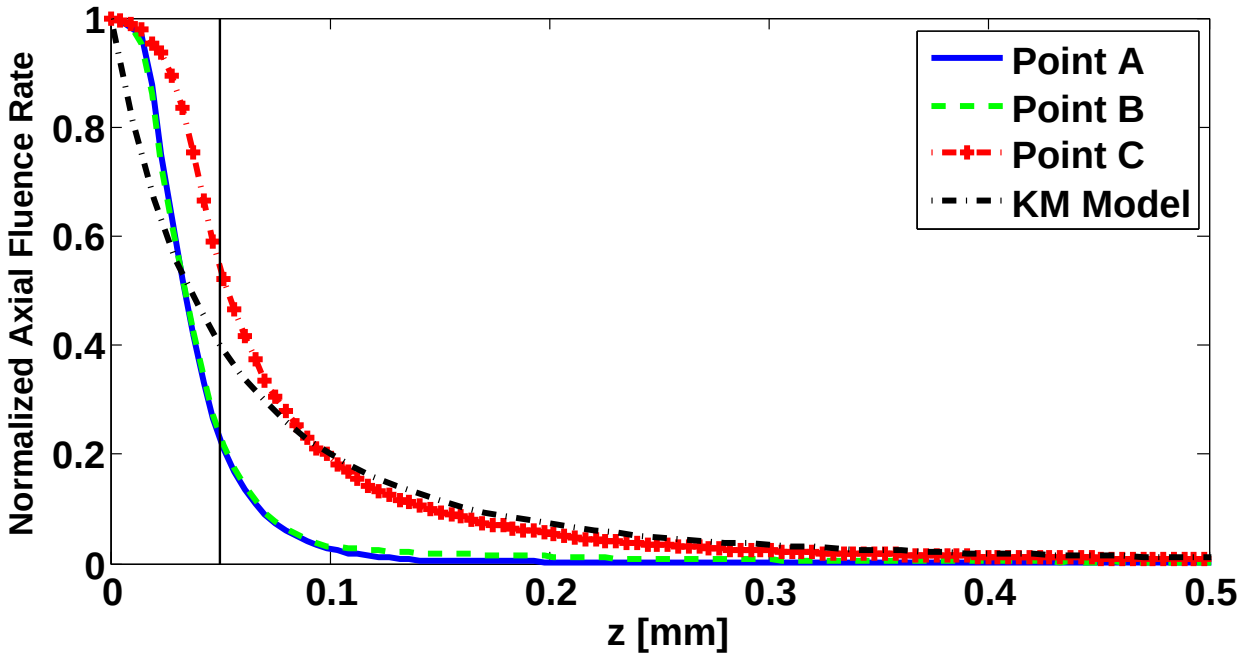

Figure 2.19: Comparison between the Monte Carlo simulation incorporating the effect of vessels and the KM model. The data for the KM model is adapted from [32] and measured at $473nm$. For other curves data was produced at $405nm$.

processing capability stems from the architecture of the cortical maps in which enormous number of spatial filters are generated in the networks by controlling the strength of coupling between neurons. To study such circuitries, we need mechanisms to reversibly manipulate the activity of cells in large-scaled networks. In recent studies, researchers have used SLMs together with optogenetics to generate complex patterns of neural stimulation [7, 8, 54].

While SLMs are delivering high-resolution and rapidly changing patterns on the surface, a main question to be answered is to which depth a projected pattern on the surface is preserved and how the networks of vessels and capillaries perturb the structure of the pattern at different depths inside the tissue. To study the pattern preservation inside the tissue, we used the database and Monte Carlo software to simulate the propagation of photons projected on the surface in the form of simple spatial frequencies. Figures 2.20 and 2.21 show two cases in which patterns representing spatial frequencies of $1lp/mm$ and $2lp/mm$ are projected on the cortical tissue inside the rectangle marked in Figure 2.16. Light distribution profile at multiple depths up to $370\mu m$ for $532nm$ green laser are illustrated in Figures 2.20.

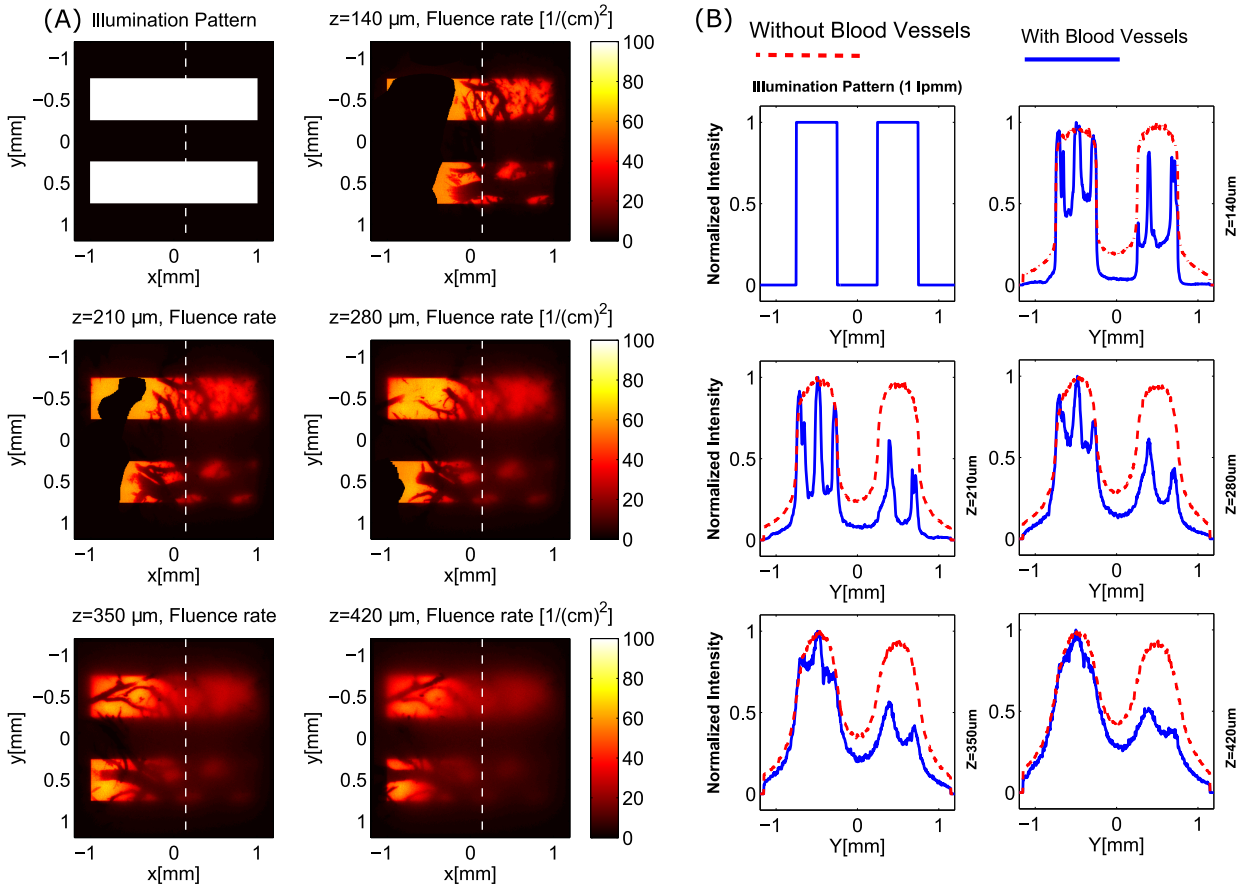

Figure 2.20: Monte Carlo simulation of pattern preservation inside the brain cortical tissue. Single spatial frequency pattern of $1lp/mm$ is projected on the cortex and the structure of the pattern is analyzed at different depths for $532nm$ light. Contours compare the results with the simplified model where the effect of blood vessels was neglected in the simulation. Patterns are projected inside the rectangle marked in Fig. 2.16.

Normalized contours in each case show the distribution of light along the marked vertical axes when the simulation is conducted for with or without blood vessels cases. The main features of the pattern close to the surface are preserved and light absorption in small capillaries only reduce the dynamic range of the fluctuations. However, slightly deeper inside the tissue, medium and larger blood vessels absorb light and produce abrupt drops in the intensity profile. This effect which is displayed clearly in the second row of contours appears like some increase in the spatial frequency of the pattern. At these depths, blood vessels produce the most noticeable difference between this data and the models in which the effect of vessels is completely ignored. Deeper inside the tissue, vessels are not as large as the pial

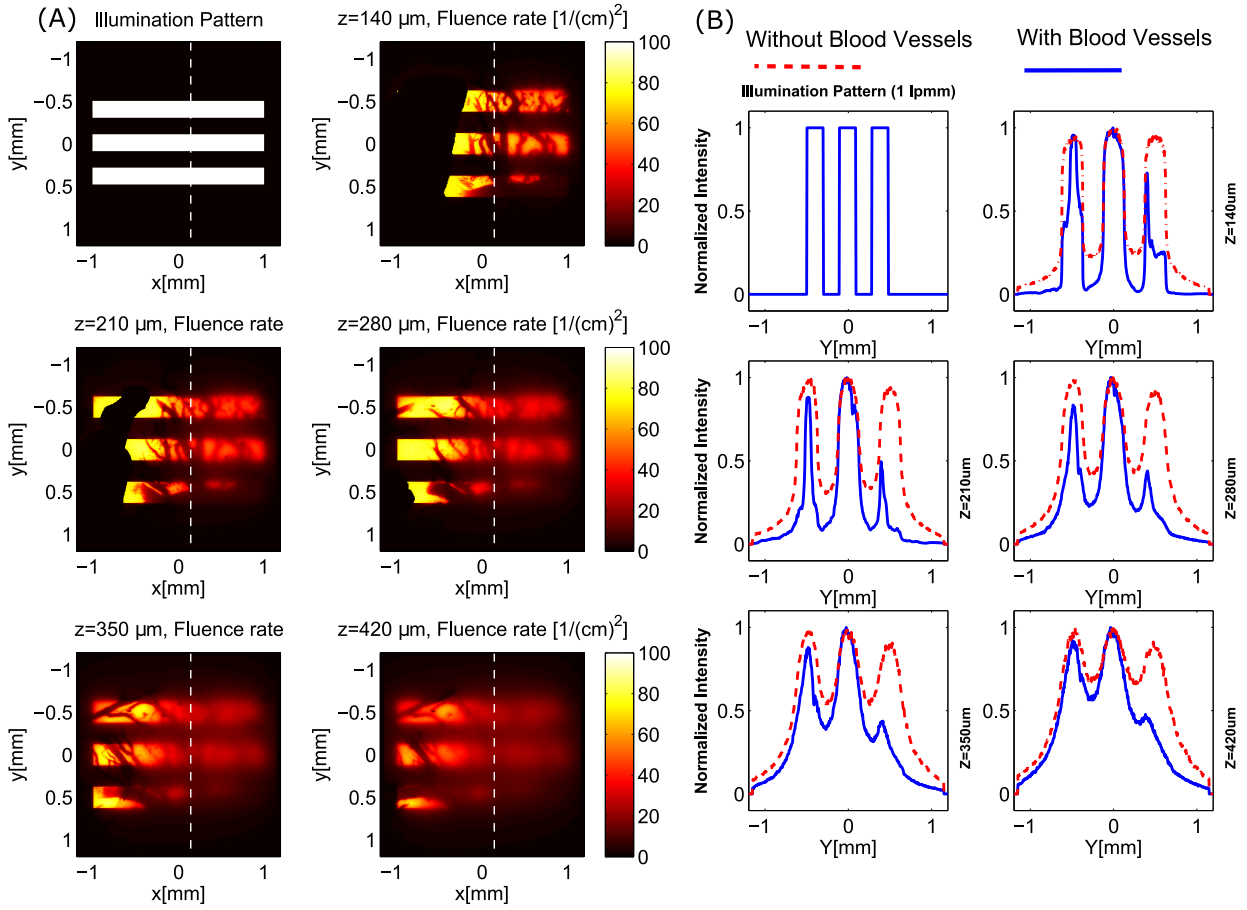

Figure 2.21: Monte Carlo simulation of pattern preservation inside the brain cortical tissue. Single spatial frequency pattern of $2lp/mm$ is projected on the cortex and the structure of the pattern is analyzed at different depths for $532nm$ light. Contours compare the results with the simplified model where the effect of blood vessels was neglected in the simulation. Patterns are projected inside the rectangle marked in Fig. 2.16.

vessels. In these areas, penetrating arterioles that delve into the tissue deliver blood to a large network of small capillaries that distribute blood in the tissue. Because of the large scattering coefficient of the brain tissue, deeper inside, the abrupt drops are compensated by the photons that scatter into the shadow of the vessels and the light distribution takes the form which looks more similar to the projected pattern on the surface. At these depths, the third row in the figure, the difference between the two sets of contours is mostly caused by the attenuation coefficient of the brain tissue. This observation is consistent and independent of the exact position of the stimulation pattern on the cortex.

2.6 Conclusion

In this chapter, we presented a new approach to extract the major optical properties (absorption and scattering coefficients, and anisotropy factor) of rat's brain tissue with spatial resolution of about 3000 sample points per square centimeter for three different cuts (transverse, sagittal, and coronal) and three different wavelengths, $405nm$, $532nm$, and $635nm$. A large database of the brain optical properties is produced by slicing the tissue and measuring these parameters in each slice followed by mapping the measurements to the atlas of rat brain [47]. The developed three-dimensional Monte Carlo simulation software is able to incorporate the effect of tissue heterogeneities, physical parameters of the source (e.g., optical fiber core diameter, numerical aperture or beam type such as uniform or Gaussian) and offers a more accurate model for prediction of light distribution in the brain. When designing an experiment to optogenetically stimulate an area inside the brain some decisions should be made regarding the physical parameters of the fiber and the intensity of light required to generate effective stimulation in the tissue. The integration of the rat brain atlas and the 3D Monte Carlo software can provide a useful toolbox and the simulations can help to choose these parameters more accurately which certainly improves the quality of the results and the rate of success particularly for *in-vivo* optogenetic experiment. Although brain tissue and optogenetic neurostimulation was the main target in this study, the proposed approach for extracting optical properties and predicting the light distribution can be adapted as a general method for other tissue samples and different applications such as laser surgery, laser therapy, optical tomography, etc.

Previous experiments have shown that mammalian blood has relatively high absorption and scattering coefficients [53] and incorporating the optical properties of the blood in the models potentially improves the precision of the predictions. One possible approach to include the effect of blood is to use advanced optical imaging methods such as optical coherence tomography (OCT) to scan the tissue and generate angiograms which provide insight to the details of blood distribution in the tissue under test. Next, this angiogram can be integrated

into the developed brain atlas of optical properties which is used for Monte Carlo simulations. In this chapter, we also looked at the effect of blood vessels on light distribution profile for few visible wavelengths. Based on our data, the approximate models that simply neglect the effect of blood vessels and even the tissue absorption coefficient can still provide a good estimation for larger wavelengths and when no large or medium size blood vessel is in the immediate vicinity of the light injection site. However, when the light delivery site is close to a major vessel, such as the middle cerebral artery (MCA) or its main branches, or in cases where light is delivered in the form of complex patterns, the effect of blood vessels is potentially bold and should be accounted for. One possible option is to use an OCT scanner to extract the volumetric angiogram of the cortex and run similar Monte Carlo simulation prior to *in-vivo* experiments to design appropriate stimulation patterns.

Chapter 3

Design and implementation of a fluorescent tomography system for brain studies

3.1 Introduction

Biomedical imaging technologies are categorized to the macroscopic, mesoscopic and microscopic imaging [62]. These imaging modalities offer different resolutions and penetration depths. Macroscopic imaging techniques such as diffusion optical tomography (DOT) [68] have a large penetration depth in the range of several centimeters with the resolution of few hundred of microns [62]. Optical coherence tomography (OCT) [67] and confocal microscopy are microscopic imaging techniques which have higher resolution in the range of a micron with an imaging depth limited to $\sim 1mm$. Mesoscopic imaging techniques, such as laminar optical tomography (LOT) [65], have a penetration depth in the range of $2mm$ offering resolution of $\sim 200um$. A comparison between different imaging modalities is shown in Figure 3.1 [62]. One bold benefit of optical imaging techniques over other imaging modalities is the possibility of doing fluorescence tomography to image and clarify the special distribution of bio-markers which is an essential element in this project.

Fluorescent proteins are employed as bio-markers to provide a tool to confirm the expression of optogenetic proteins such as ChR2 or NpHR. For this purpose, the gene which encodes a specific fluorescent protein is delivered and co-expressed in the same cell. The fluorescent signal from such proteins provides a monitory mechanism to evaluate the expression of optogenetic opsins over time. If these fluorescent proteins are illuminated by appropriate wavelengths of light, they emit fluorescent signals which indirectly confirms the expression

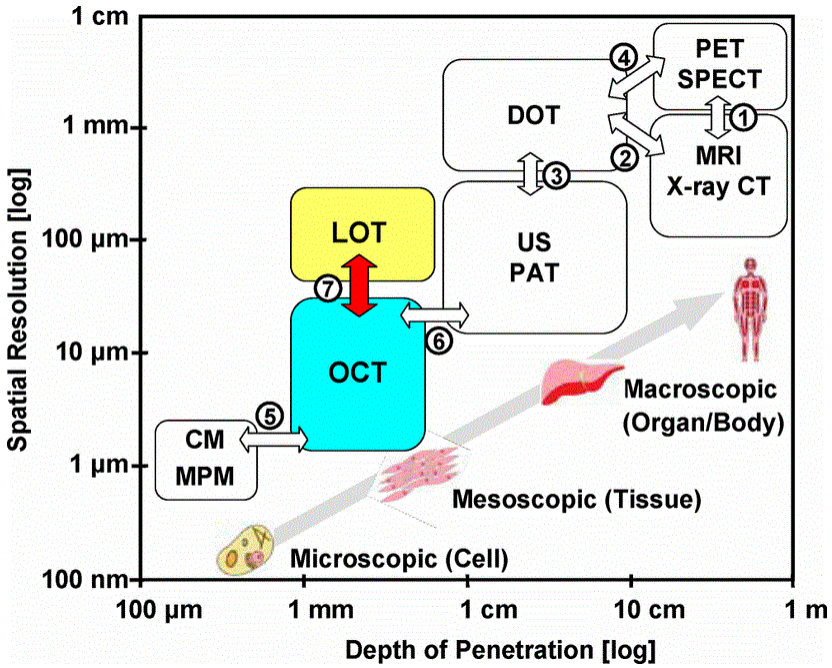

Figure 3.1: A comparison between different imaging modalities based on the imaging depth and resolution [62]. PET: positron emission tomography, SPECT: single-photon emission computerized tomography, MRI: magnetic resonance imaging, DOT: diffusion optical tomography, OCT:optical coherence tomography, CM: confocal microscopy, MPM: multiphoton microscopy, CT: computerized tomography.

of the light sensitive opsins. Figure 3.2 shows the schematic of a tagged ChR2 molecule with green fluorescence protein (GFP). The GFP can be excited by blue light exposure and the emitted green fluorescent signal can be captured for the imaging purpose. The conventional method to confirm the success in gene delivery is to sacrifice the animal, retract and slice the brain tissue, and image the corresponding slices using a fluorescent microscope. Obviously, determining the level of expression over time without sacrificing the animal is highly desirable. The aim of this part of project is to develop a custome-made fluorescent laminar optical tomography (FLOT) system [65], both hardware and software, to be used during *in-vivo* optogenetic experiments to confirm the expression of light sensitive opsins in rodents' brain.

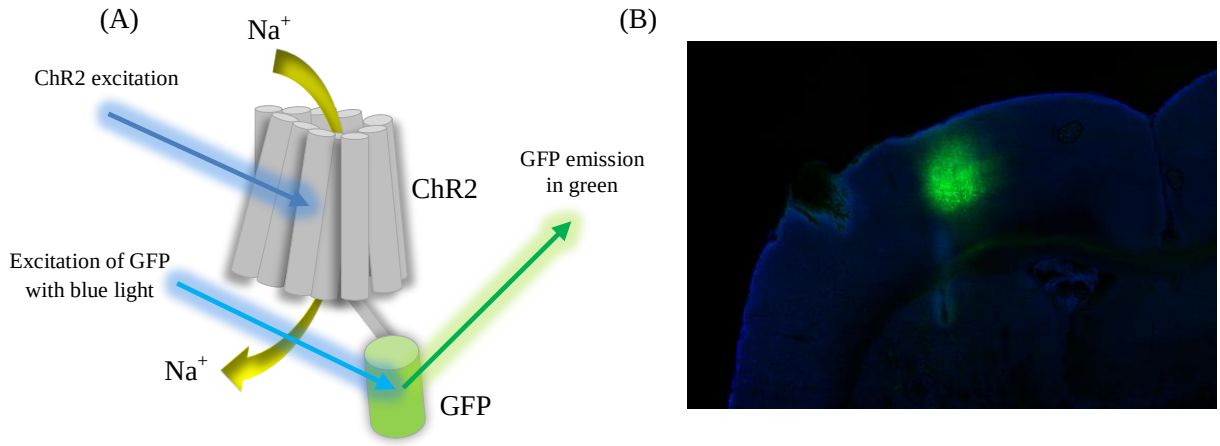

Figure 3.2: (A) Co-expression of light sensitive protein $ChR2$ and green fluorescent protein (GFP) where GFP can be excited by a blue light exposure and to emit green light, (B) confocal fluorescent image of a rat brain slice transfected by GFP on the left hemisphere.

3.2 Optical Tomography

Using light for medical imaging goes back to 1831, where Bright showed that light can be used to diagnose hydrocephalus in a child [64]. Hydrocephalus is the result of some abnormal increase in cerebro-spinal fluid (CSF) in the head. Unlike CSF, which does not have a significant scattering coefficient, biological tissues are highly scattering mediums and direct imaging using ballistic beams is limited to few hundred micron penetration depth. Optical imaging techniques, such as confocal microscopy or optical coherence tomography, are non-invasive imaging techniques which are mostly based on collecting ballistic beams and minimizing the detected scattered light [64]. Even though these imaging modalities have a high resolution on superficial layers, as light travels more than $1mm$ inside the tissue, the scattering effect is dominating and these methods cannot image any deeper inside the sample. To optically image deep inside a specimen, we need to consider the fact that photons experience multiple scattering before reaching detectors. To employ the scattered light for imaging purposes, a model describing the propagation of light in a turbid medium is required. Propagation of light in a medium can be described by the radiative transport equation (RTE) [48]. Diffusion approximation to the radiative transport equation is applied when the

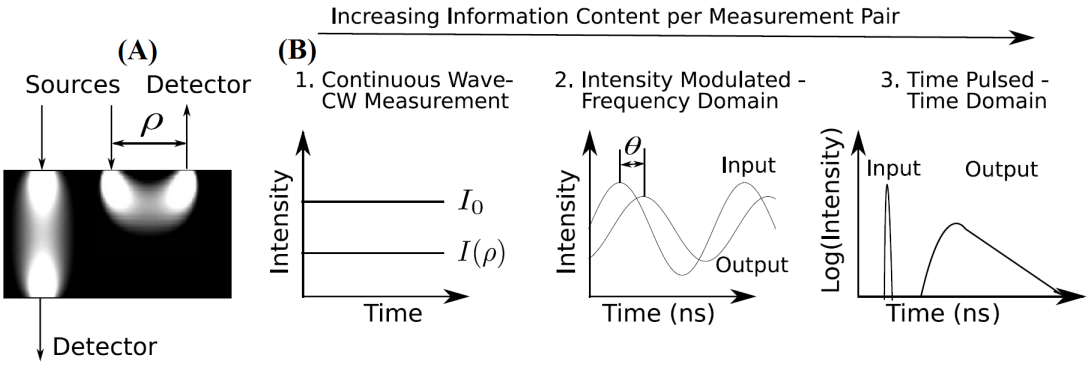

Figure 3.3: (A) Source-detector configuration for the transmission and reflection geometries, (B) different type of light sources are employed for optical tomography, continuous wave (CW), frequency domain(FD) and time resolved (TR) [66].

reduced scattering coefficient is higher than absorption coefficient and the detected photons experience multiple scattering before reaching detectors. Monte Carlo [50] method which are based on the RTE, provides a numerical algorithm to simulate photons propagation in turbid mediums. Monte Carlo is a relatively simple yet powerful and reasonably precise statistical method which is capable of handling complicated boundary conditions particularly useful when finding a close-form solution based on RTE is not readily feasible.

There are two main source-detector configurations for optical tomography: reflection and transmission geometries [66]. In reflection geometry, sources and detectors are placed on the same side of the medium, while in the transmission mode, they are placed on either sides (Figure 3.3(A)). Three different light source types are employed for optical tomography including: continuous wave (CW), intensity modulated (frequency domain, FD) and time resolved (TR) (3.6). In CW method, the amplitude of light source is constant during the measurements and it requires simple detectors to measure the optical signal. The detected amplitude information are used to extract the unknown parameters (absorption coefficient or reduced scattering coefficient). In FD method, the amplitude of light source is modulated at frequencies in the range of few megahertz. In this method, besides the amplitude of diffused photons, the phase information is measured as well. These information enables us to extract the absorption and reduced scattering coefficients of the medium. In TR method, medium

is illuminated by ultrashort light pulses ($< 100ps$) and the broadened profiles are detected. This broadened signal profiles provide enough information to extract the absorption and reduced scattering coefficient of the medium. Designing the source and detectors in TR methods is more complicated than the CW and FD techniques.

Forward Model

All optical tomography techniques have two distinct steps: developing a forward model describing the propagation of light in a medium, and then, solving the inverse problem to find unknown parameters based on the measurements and the forward model. Propagation of photons inside a biological tissue can be modeled by the radiative transport equation [48]:

$$\frac{1}{c}\frac{\partial\phi(r,t)}{\partial t} + \bigtriangledown.J(r,t) - \mu_a(r)\phi(r,t) = S(r,t), \tag{3.1}$$

where c is the speed of light in the medium, $\phi(r,t)$ is the photon fluence rate, $J(r,t)$ is the photon flux, $S(r,t)$ is the total power per volume emitted from position r and $\mu_a(r)$ is the absorption coefficient. By applying diffusion approximation to the radiative transport equation ($\partial\phi(r,t) = -3(\mu_s' + \mu_a)J(r,t)$) [48], equation 3.1 reduces to:

$$\bigtriangledown .(D(r) \bigtriangledown \phi(r,t)) - \nu\mu_a(r)\phi(r,t) + \nu S(r,t) = \frac{\partial\phi(r,t)}{\partial t}. \tag{3.2}$$

This equation relates the changes in the photon fluence rate to the power emitted from the source, scattered photons and photons absorbed in the medium. In diffusion approximation, it is assumed that the radiation is almost isotropic; therefore, this model is not suitable for small source-detector separations similar to what we have in LOT systems where the distance between the source and detector pairs are less than the scattering length of photons [65]. As discussed later in this chapter, for LOT setups, Monte Carlo simulations [50] are employed to generate the sensitivity matrix for each source-detector pair. For a phantom with optical properties of $\mu_a = 1mm^{-1}$ and $\mu_s^{'} = 0.9mm^{-1}$, the simulated sensitivity matrix

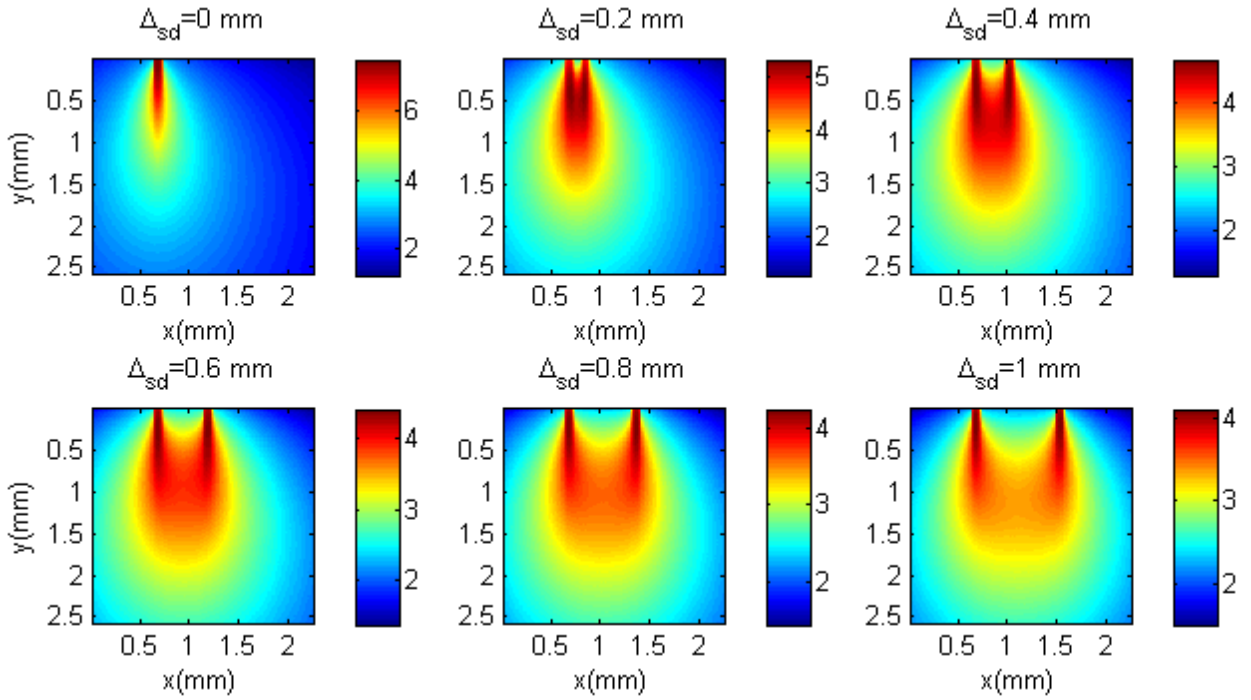

Figure 3.4: Simulated sensitivity matrix for different source-detector separation distances for a phantom with optical properties of $\mu_a = 1mm^{-1}$ and $\mu_s^{'} = 0.9mm^{-1}$.

for different source-detector pairs are shown in Figure 3.4.

Image Reconstruction

After developing the forward model, which represents the sensitivity of the measurements to the parameters of interest, the unknown parameter is obtained by solving the inverse problem:

$$\begin{pmatrix} M_{11} \\ M_{21} \\ \vdots \\ M_{m1} \end{pmatrix} = \begin{pmatrix} W_{11} & W_{12} & \cdots & W_{1n} \\ W_{21} & W_{22} & \cdots & W_{2n} \\ \vdots & \vdots & \ddots & \vdots \\ W_{m1} & W_{m2} & \cdots & W_{mn} \end{pmatrix} \times \begin{pmatrix} C_{11} \\ C_{21} \\ \vdots \\ C_{n1} \end{pmatrix}, \tag{3.3}$$

where in this equation, matrix M is generated through experimental measurements, each row

of W represents the voxelized sensitivity matrix of each measurement simulated using Monte Carlo method and (C) is the spatial distribution of fluorophore concentration in each voxel (unknowns). The tomographic reconstruction problems are mostly ill-posed, where the number of measurements are less than unknowns. Different analytical and numerical algorithms including singular value decomposition method, algebraic reconstruction technique (ART) [70], simultaneous algebraic reconstruction technique (SART) [71], lease square (LSQR) [73] and simultaneous iterative reconstruction technique (SIRT) [72] are employed for reconstruction. In this work, SART is used for image reconstruction and a brief overview of this method is given in the following.

The algebraic reconstruction technique is an iterative method for solving a system of linear equations $Ax = b$ and was employed for the first time by Gordon *et. al.* [70] for medical image reconstruction. In linear algebra, this algorithm is known as Kaczmarz method [74]. Suppose that we have a system of linear equations with M linear equations and N unknowns:

$$\begin{cases} W_{11}f_1 + W_{12}f_2 + W_{13}f_3 + ... + W_{1N}f_N = p_1 \\ W_{21}f_1 + W_{22}f_2 + W_{23}f_3 + ... + W_{2N}f_N = p_2 \\ . \\ . \\ W_{M1}f_1 + W_{M2}f_2 + W_{M3}f_3 + ... + W_{MN}f_N = p_M \end{cases} \tag{3.4}$$

where variables are represented by $(f_1, f_2, ..., f_N)$. The computational procedure to solve equation 3.4 using Kaczmarz method starts by making an initial guess $(f_1^{(0)}, f_2^{(0)}, ..., f_N^{(0)})$ shown by a N dimensional vector $\vec{f^0}$ [74]. In the next step, the initial guess is projected on the first hyperplane in equation 3.4 which results in vector $\vec{f^1}$; then $\vec{f^1}$ is projected on the second hyperplane, and so on so forth. The iterative mathematical procedure for this

method is described by the following equation:

$$\vec{f}^{i} = \vec{f}^{i-1} - \lambda \frac{\vec{f}^{i-1}.\vec{w}_i - p_i}{\vec{w}_i.\vec{w}_i}\vec{w}_i, \tag{3.5}$$

where λ is the relaxation (damping) parameter in the range of $(0, 1]$. The relaxation parameter can be a constant number for all iterations or systematically determined at each iteration using methods such as the method line search. Based on equation 3.5, the value of jth pixel at each iteration is [70]:

$$\Delta {f_j}^{(i)} = {f_j}^{(i)} - {f_j}^{(i-1)} = \frac{p_i - q_i}{\sum_{k=1}^{N} {w_{ik}}^2} w_{ij}, \tag{3.6}$$

where q_i is defined as:

$$q_i = \vec{f}^{i-1}.\vec{w}_i = \sum_{k=1}^{N} {f_k}^{(i-1)} w_{ik}. \tag{3.7}$$

The ART is a relatively fast algorithm but the reconstructed images usually suffer from salt and pepper noise [71]. This noise in ART reconstructed images can be reduced by introducing a relaxation parameter which helps to achieve smoother reconstructions. In general, there is a compromise between the improvement in the image quality and the convergence speed of the basic ART algorithm [71]. Another approach to improve the reconstruction quality at the expense of slower convergence speed is employing the simultaneous iterative reconstruction technique (SIRT) [72]. Unlike ART, in which pixel values change at each iteration, in SIRT, pixel values do not change until going through all the equations. At the end of iterations, the pixel values change to the average value of all the computed changes for each specific pixel. To take advantage of both ART and SIRT, and to obtain fast convergence and good reconstruction quality, simultaneous ART (SART) was proposed by Anderson [71].

In most tomography systems, including LOT, the number of measurements is smaller than unknowns ($M < N$); therefore, there is no unique solution to the equation 3.4 and

this ill-posed problem has infinite number of solutions. It is shown in [74] that equation 3.4 converges to an optimal solution $\vec{f_s}$, to minimize $|\vec{f^0} - \vec{f_s}|$. One of the aspects of iterative techniques such as SART is that prior information can be incorporated in the process of finding the optimal solution. In the case of fluorescent tomography, non-negativity constrain is imposed to the algorithm and at each iteration, zero is assigned to all variables with negative values.

Improving depth localization in fluorescent optical tomography

In optical tomography systems such as DOT and LOT, the sensitivity of measurements drops exponentially as a function of penetration depth. The outcome of lower sensitivity at higher depths is inaccurate depth localization of objects and biased reconstruction toward superficial areas [79, 80]. In [80], a depth compensation algorithm is proposed which attempts to counterbalance the exponential decay of light penetration and directly modifies the weight matrix W. Suppose that the image, to be reconstructed, is consisting of l layers. Therefore, the sensitivity matrix W can be decomposed to l submatrices:

$$W = [W_1 W_2, ...W_l], \tag{3.8}$$

where W_1 is the most superficial layer and W_l is the deepest layer. Then, the maximum singular for each submatrices are calculated and the matrix S is constructed as following:

$$S = \begin{pmatrix} M(W_l) & & & & \\ & M(W_{l-1}) & & & \\ & & \ddots & & \\ & & & M(W_2) & \\ & & & & M(W_1) \end{pmatrix}^{\gamma}, \tag{3.9}$$

where $M(W_j)$ is the maximum singular value of layer j, and γ is an adjustable power between 0 and 3 [80]. Finally, the weighted sensitivity matrix, $W^{\#}$, is calculated by:

$$W^{\#} = WS. \tag{3.10}$$

Based on equation 3.9 and 3.10, maximum singular values in matrix S are arranged inversely from the top to the bottom layers, and once multiplied by the sensitivity matrix W, it compensates the decay in measurements' sensitivity along the axial direction.

3.3 Developed Fluorescent Tomography System

In the following section, details of the developed FLOT setup for fluorescent protein imaging is described and experiments with phantoms and *in-vivo* results are presented.

Experimental setup

In fluorescent imaging techniques, fluorophores are excited by appropriate light wavelengths within the absorption spectra of the molecule and the emitted fluorescent light of longer wavelength is separated by using an appropriate optical filter in front of a photodetector. In a LOT system, the excitation pattern could be in the form of a point source [65] or line illumination [62]. To acquire high resolution data in a point source illumination setup, an array of fast photodetectors are required to reduce the scanning time. In line illumination [62], a CCD camera can be used to acquire data along the lines parallel to the illumination pattern to significantly reduce the scanning time. Our FLOT system is designed based on line illumination and the schematic of the system is shown in Figure 3.5. The implemented experimental setup is shown in Figure 3.6.

This system has two optical paths: the *excitation* path which delivers the light pattern to the surface of the sample and the *imaging* path which records the emitted fluorescent signal. In the excitation path, the output beam of a single mode blue laser diode ($450nm$ single

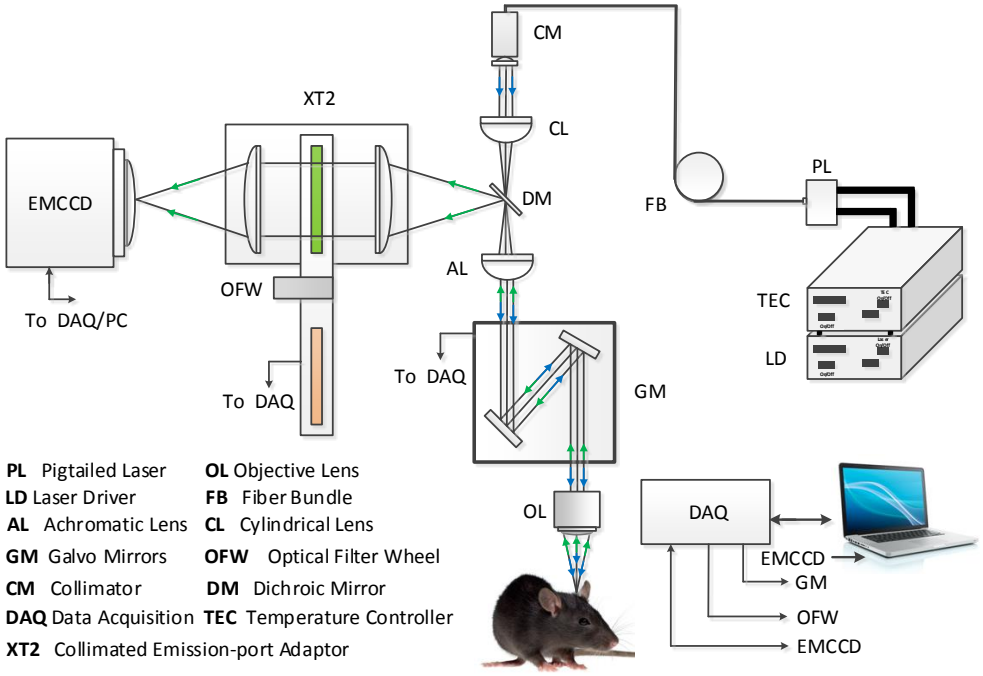

Figure 3.5: Schematic of the developed FLOT system.

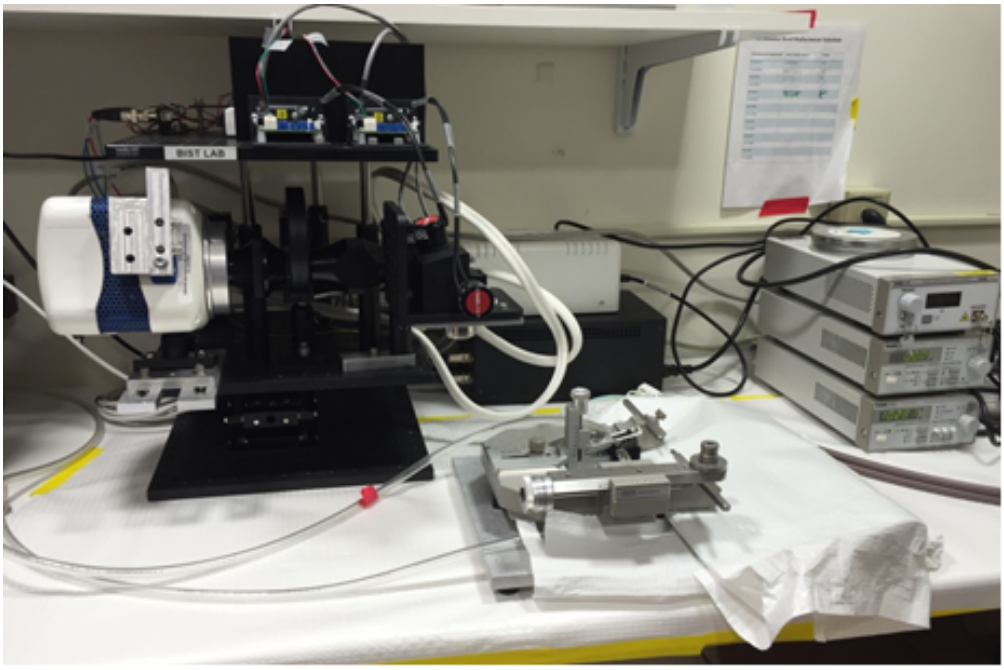

Figure 3.6: Developed FLOT system.

mode pigtailed laser diode, Thorlabs Inc., Newton, NJ) was collimated by a fiber collimating lens achieving the output beam diameter of $10mm$. To reshape the collimated beam to a line pattern, a cylindrical lens is employed (LJ1695RM, Thorlabs Inc., Newton, NJ). After

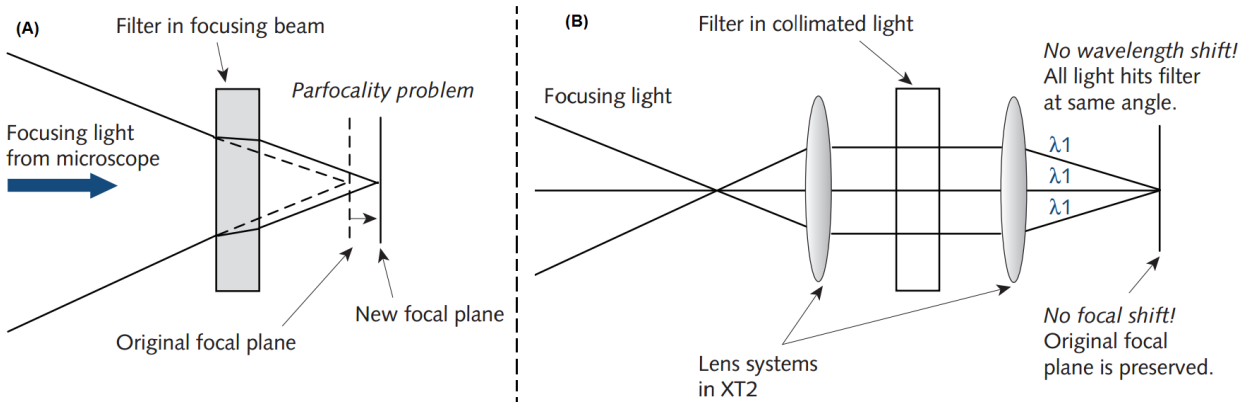

Figure 3.7: Schematic of the XT2 collimated emission-port adapter, adapted with some modifications from [75].

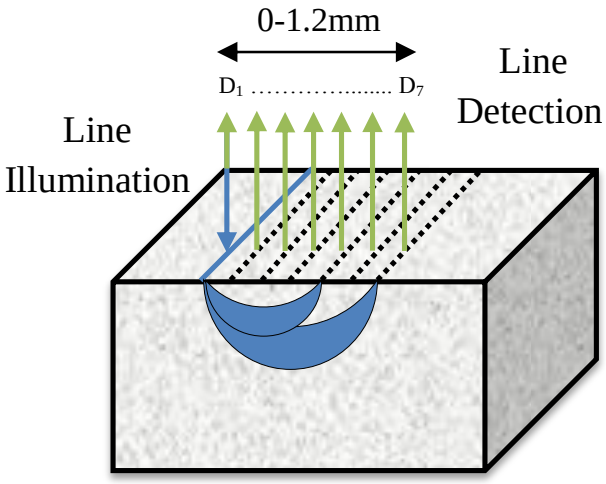

Figure 3.8: Source-detector configuration in a line-patterned FLOT system [62].

passing through a dichroic mirror (FF440/520-Di01, Semrock, Rochester, NY) and before reaching a scan lens, an achromatic doublet lens (AC254-060-A-ML, Thorlabs Inc., Newton, NJ) with the focal length of $f_2 = 60mm$ was placed in a way that the distance between the cylindrical and achromatic lens was $f_1 + f_2$. The excitation light, after passing through the dichroic mirror, hits a pair of moving X and Y galvanometer mirrors (GVS212, Thorlabs Inc., Newton, NJ). The galvanometer mirrors are controlled by the computer software prepared under LabVIEW (National Instruments, Austin, TX) to steer the collimated beam through a scan lens. The scan lens (LSM03-VIS, Thorlabs Inc., Newton, NJ) focuses the line-beam on the surface of the tissue to scan the predefined field of view (FOV) by converting the angular changes on one of the galvanometer mirrors into a horizontal translation of the scanning line.

The re-emitted light from the fluorophores inside the tissue travels back through the same scan lens and is de-scanned by the galvanometer mirrors. To this point, the excitation and detection path are the same; however, after reaching the dichroic beam splitter, only the emitted fluorescence light is reflected toward the light detection components of the system. To completely reject the undesired wavelengths associated with the detected fluorescent signal, a narrow-band optical filter is placed in front of a detector (EMCCD, Evolve 512, Photometrics, Tucson, AZ). The light entering the optical filter is a converging beam, and placing optical devices such as filters or dichroic mirrors in front of a converging beam results in errors such as parfocality or bandpass variation [75]. Therefore, a two-piece collimated emission-port adapter was employed in the system which provides a collimated space to place the optical filter in the system without sacrificing the resolution (XT2, Photometrics, Tucson,AZ) (Fig. 3.7). A typical source-detector configuration in a line-patterned FLOT system is shown in Figure 3.8.

Phantom Experiments

Phantom Preparation

To test the performance of the system, first phantoms with optical properties close to the properties of the cortical tissue were fabricated ($\mu_a = 0.05mm^{-1}$, $\mu_s = 11mm^{-1}$, and $g = 0.9$ at $450nm$ wavelength). Polydimethylsiloxane (PDMS) was chosen as the base for our phantoms and microchannels were embedded inside this substrate and filled with a fluorescent solution (Fig. 3.9). To introduce scattering and absorption to the phantom, titanium dioxide (TiO2) and India ink were used, respectively. To develop an accurate forward model for the system, a good estimation of the phantom optical properties was required. Therefore, the double integrating setup discussed in chapter 2 was employed to obtained optical properties of fabricated phantoms.

(A) PDMS substarte

(B) Microchannel imaged by a microscope

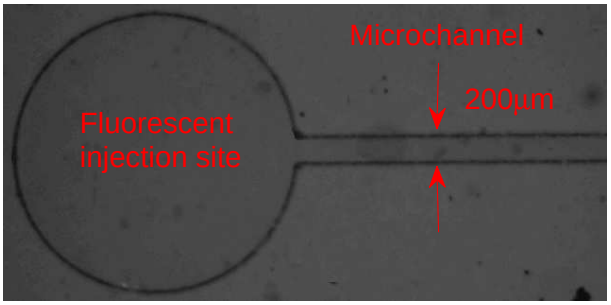

Figure 3.9: (A) Microchannels were fabricated on a PDMS substrate, (B) image of a microchannel layout captured by a microscope.

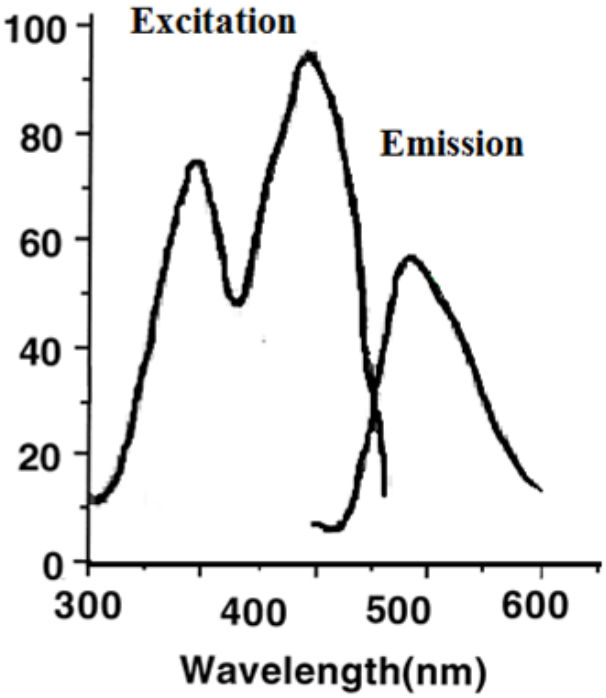

Figure 3.10: Excitation/emission spectrum of FAD.

Phantom Image Reconstruction Results

After fabricating the microchannel phantom, flavin adenine dinucleotide (FAD) fluorescent agent was injected into the channel. The excitation and emission spectrum of FAD is shown in

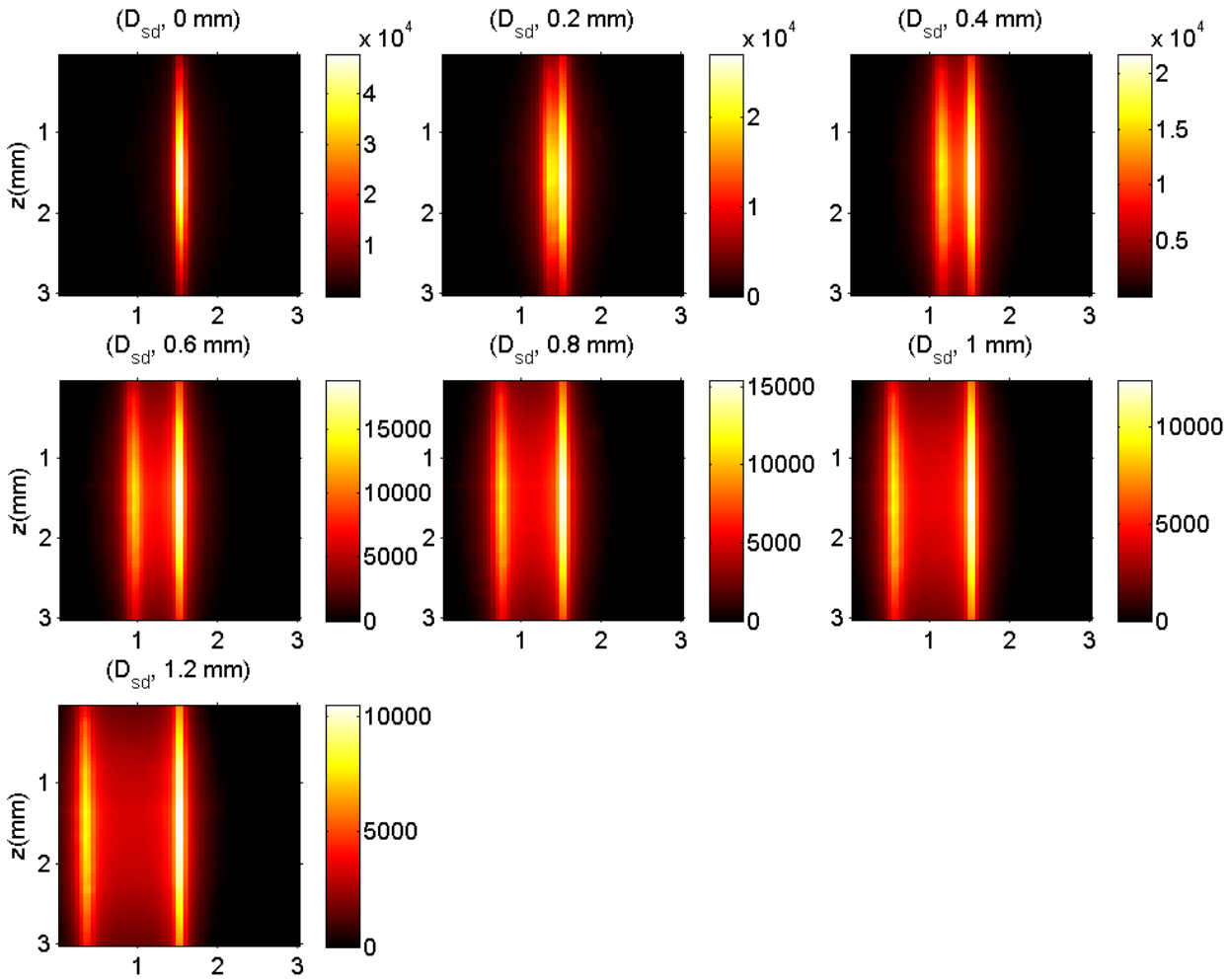

Figure 3.11: Experimental raw data obtained by the detectors number 1 through 7 for a micro-channel at the depth of $700\mu m$.

Figure 3.10. Then, an area of $3mm \times 3mm$ was scanned by a line-shaped laser beam at $450nm$ with the spatial resolution of $70lp/mm$. For each scan, an image was taken by the EMCCD camera and transfered to a computer for further processing and extracting the information of different detectors. In our system, seven (in some cases up to nine) lines of source-detectors (D_1 to D_7) were defined with $0.2mm$ separation from 0 to $1.2mm$ (in some cases up to $1.6mm$). The dataset consisting of $200 \times 200 \times 7$ measurements was down sampled to $60 \times 60 \times 7$ and used in our reconstruction algorithm. For a microchannel buried at the depth of $700\mu m$, the experimental raw data obtained by detectors number 1 through 7 are shown in Figure 3.11. These experimental raw data were employed in our reconstruction algorithm

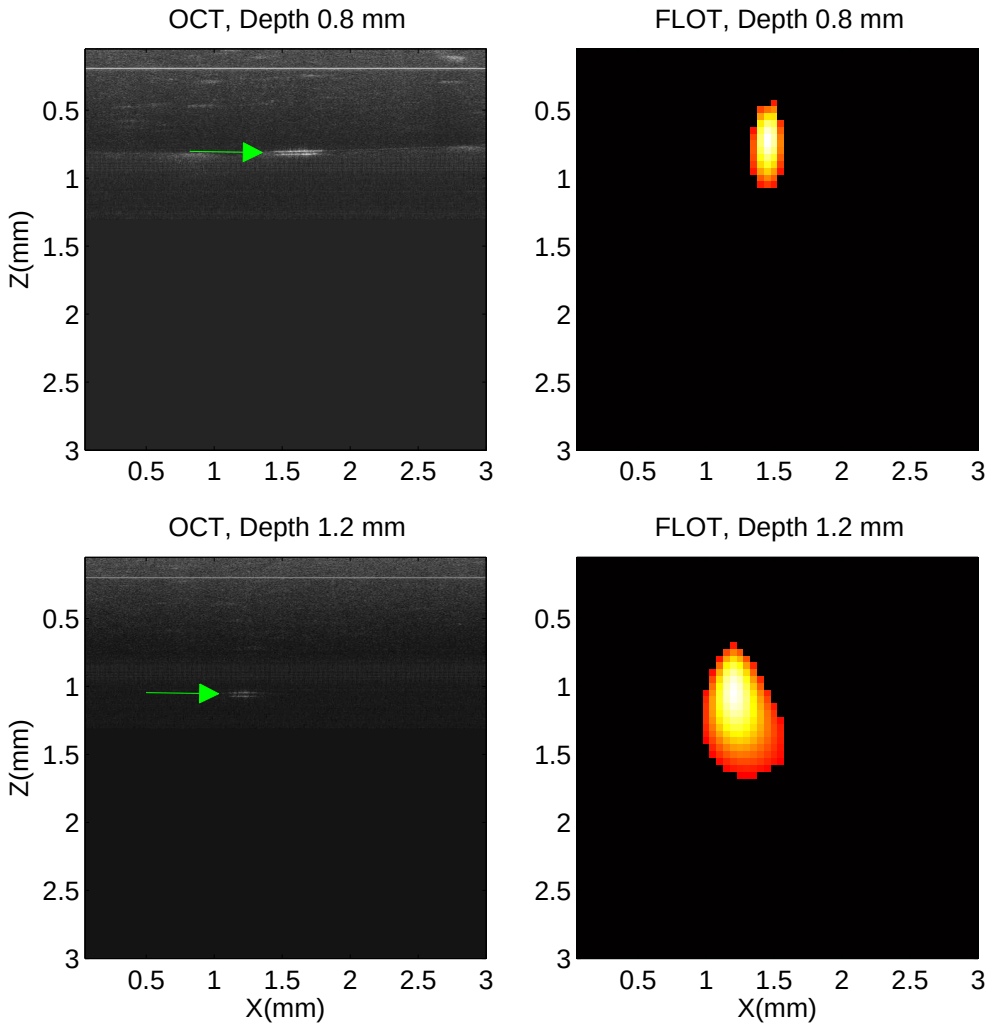

Figure 3.12: The accurate depth of the microchannels were measured by employing an OCT system which are shown on the left panels. A cross-section of the reconstructed fluorescent objects are shown in the right panels.

to reconstruct the image of the fluorescent object. To further confirm the actual depth of the microchannels, a Fourier-domain optical coherence tomography (FD-OCT) system which is developed in the lab was employed to image the samples. In Figure 3.12, the OCT images show the actual depth of two microchannels (left panels) buried at the depth of $800\mu m$ and $1200\mu m$, and the right panels show the fluorescent reconstruction results. By increasing the depth of microchannels, the point spread function (PSF) of the system increases and as a result, the diameter of the reconstructed channels increases as well. Reconstructions were performed in 2D planes and the 3D structure of the fluorescent object was obtained

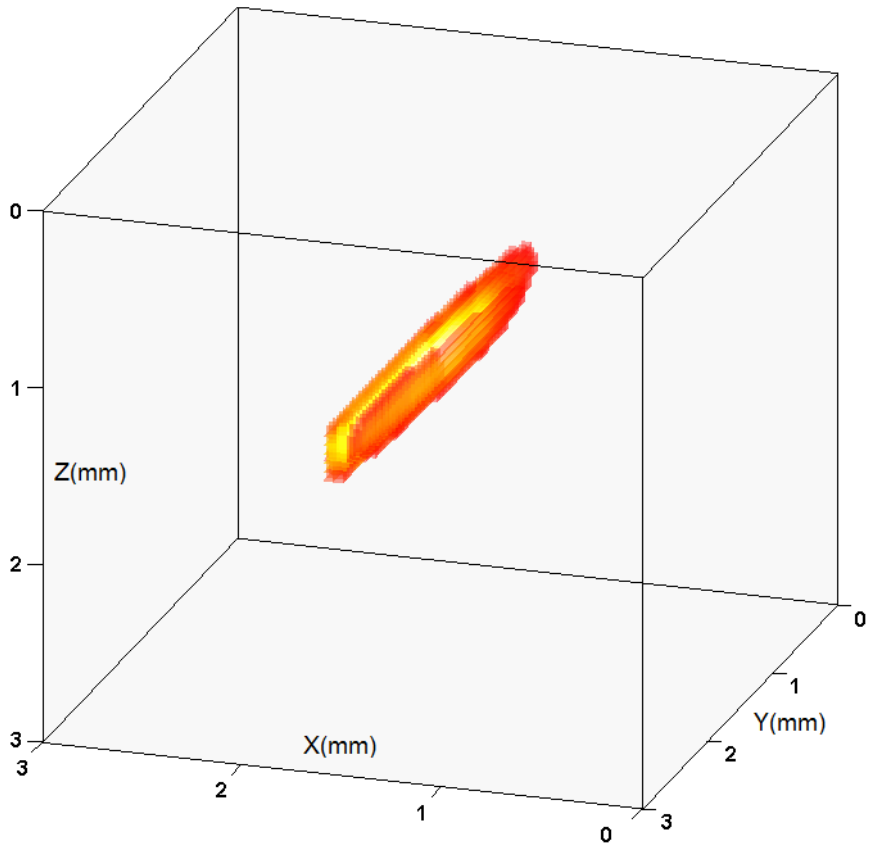

Figure 3.13: 3D reconstruction result of a microchannel filled with FAD located at the depth of $1.2mm$.

by stacking 2D images [62]. An example of the 3D reconstruction of a microchannel at the depth of $1.2mm$ is shown in Figure 3.13.

In-vivo Experiments

Surgical Procedures

All procedures were carried out in a facility accredited by the Association for Assessment and Accreditation and Laboratory Animal Care and approved by the University of Wisconsin-Milwaukee Institutional Animal Care and Use Committee (IACUC) and conducted within the ethical guidelines of the National Institutes of Health (NIH).

Animals were anesthetized with isoflurane in 100% oxygen (induction occurred with 4%

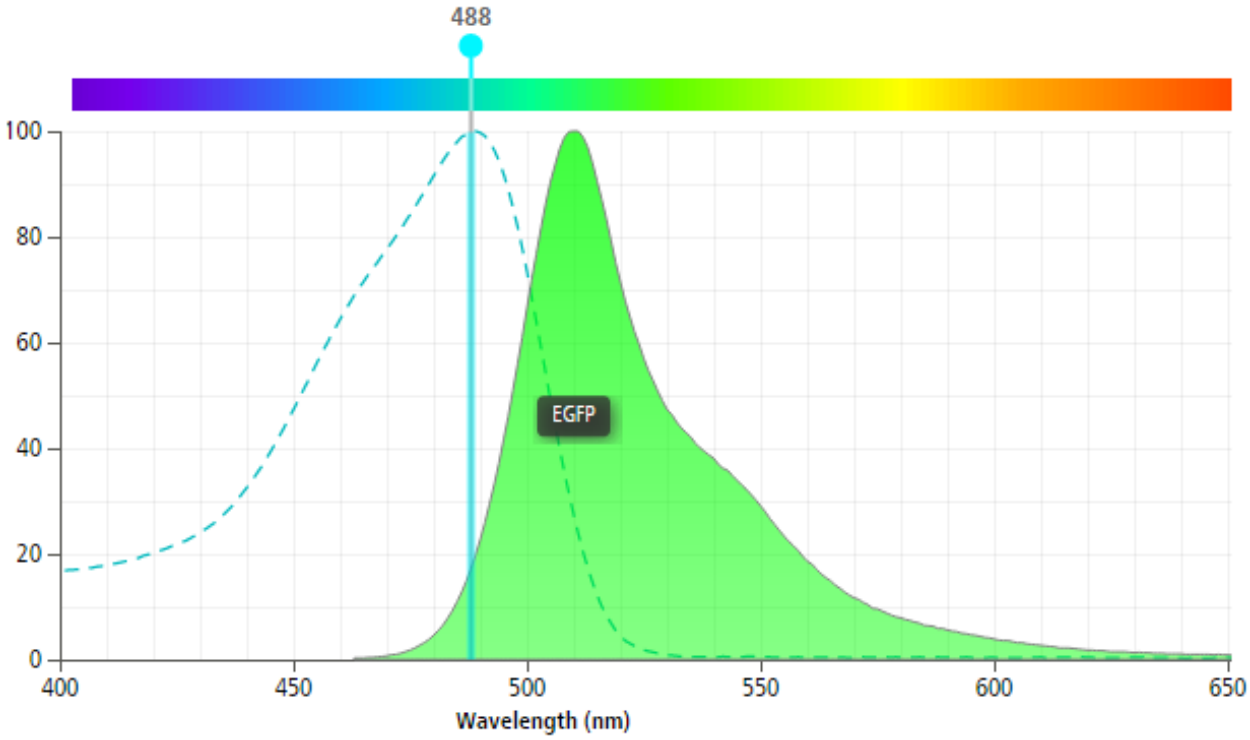

Figure 3.14: Excitation/emission spectrum of GFP, adapted with some modifications from [78].

isoflurane and maintained with 2%). Rats were mounted in a stereotaxic apparatus (Kopf Instruments). Purified viral vector AAV9-CAG-GFP was infused into the primary somatosensory cortex (forelimb) (A/P -1.0 mm, M/L + 3.8 mm) and the primary visual cortex (A/P -5.3 mm, M/L -3.8 mm). The depth of injection was systematically varied to include 0.8mm, 1.0 mm, 1.5mm, and 2.0mm. The injection volume was also systematically varied to include $0.2\mu l$, $0.5\mu l$, and $0.75\mu l$. The virus was infused using a $10\mu l$ syringe with a 34-gauge needle mounted to a stereotaxic automated injector at a rate of $0.05\mu l/min$. The injector was left in place for 10 minutes after the injection to allow diffusion of the virus away from the injector. Two to three weeks later, animals were ready for experiments.

Immediately following the completion of the experiment, animals were deeply anesthetized with isoflurane, transcardially perfused with 0.2M PBS followed by 10% buffered formalin. Brains were removed and post-fixed in 10% formalin for 24-hours before being transferred to 30% sucrose/PB. The brains were then frozen, sectioned into coronal slices

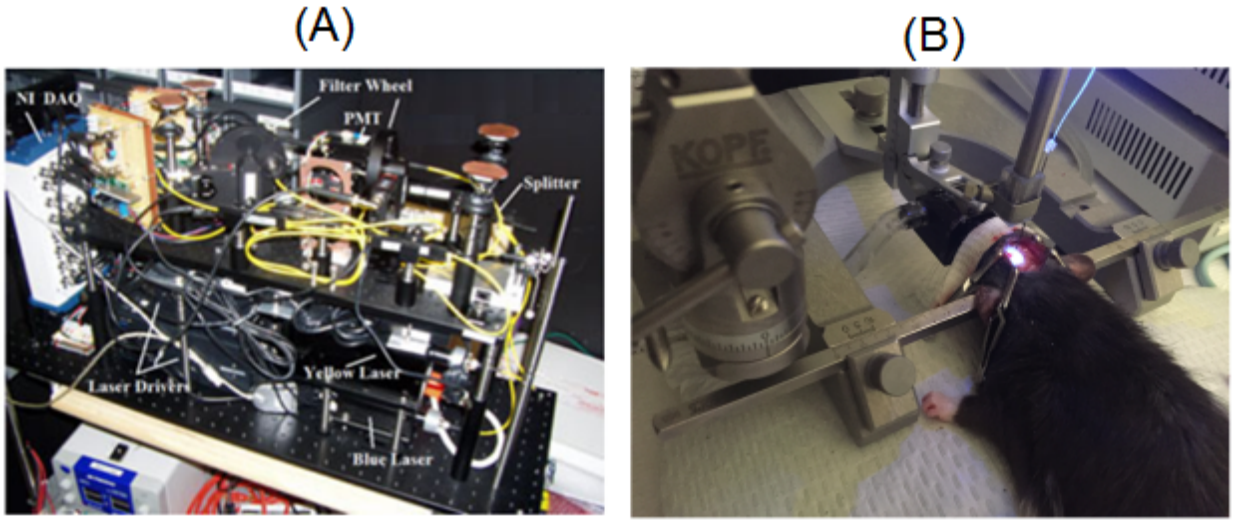

Figure 3.15: (A) Single optical fiber probe system for fluorescence detection and optogenetic stimulation [30], (B) a precise positioner was employed to guide the optical fiber inside the brain tissue.

of $200\mu m$ thickness, mounted on glass slides, and coverslipped with UltraCruz mounting medium (Santa Cruz, CA) containing $1.5\mu g/ml$ DAPI (for nuclear counter staining).

In-vivo Experimental Results

The *in-vivo* experiments were conducted in thinned-skull rats which were injected to express GFP in the cortical tissue at different depths and by different injection volumes. The excitation and emission spectrum of GFP are shown in Figure 3.14. Two separate mechanisms were employed to compare the FLOT results with actual expression of GFP. After gathering the required experimental data for the fluorescent tomography, the single optical fiber probe system which was developed in the lab [30], was employed to clarify the axial distribution of the GFP deep inside the brain at the injection site (Figure 3.15). In this system, a thin multimode fiber serves as the head of the probe to be inserted into the brain. This fiber is used to deliver blue laser pulse of $473nm$ wavelength to the region of interest and guide a sample of the emission signal back to a detector. A highly sensitive avalanche photodiode (APD) module or a photomultiplier (PMT) is used to detect the fluorescence emission signal. At the final step, the brain tissue was extracted and several slices of thickness $50\mu m$ were

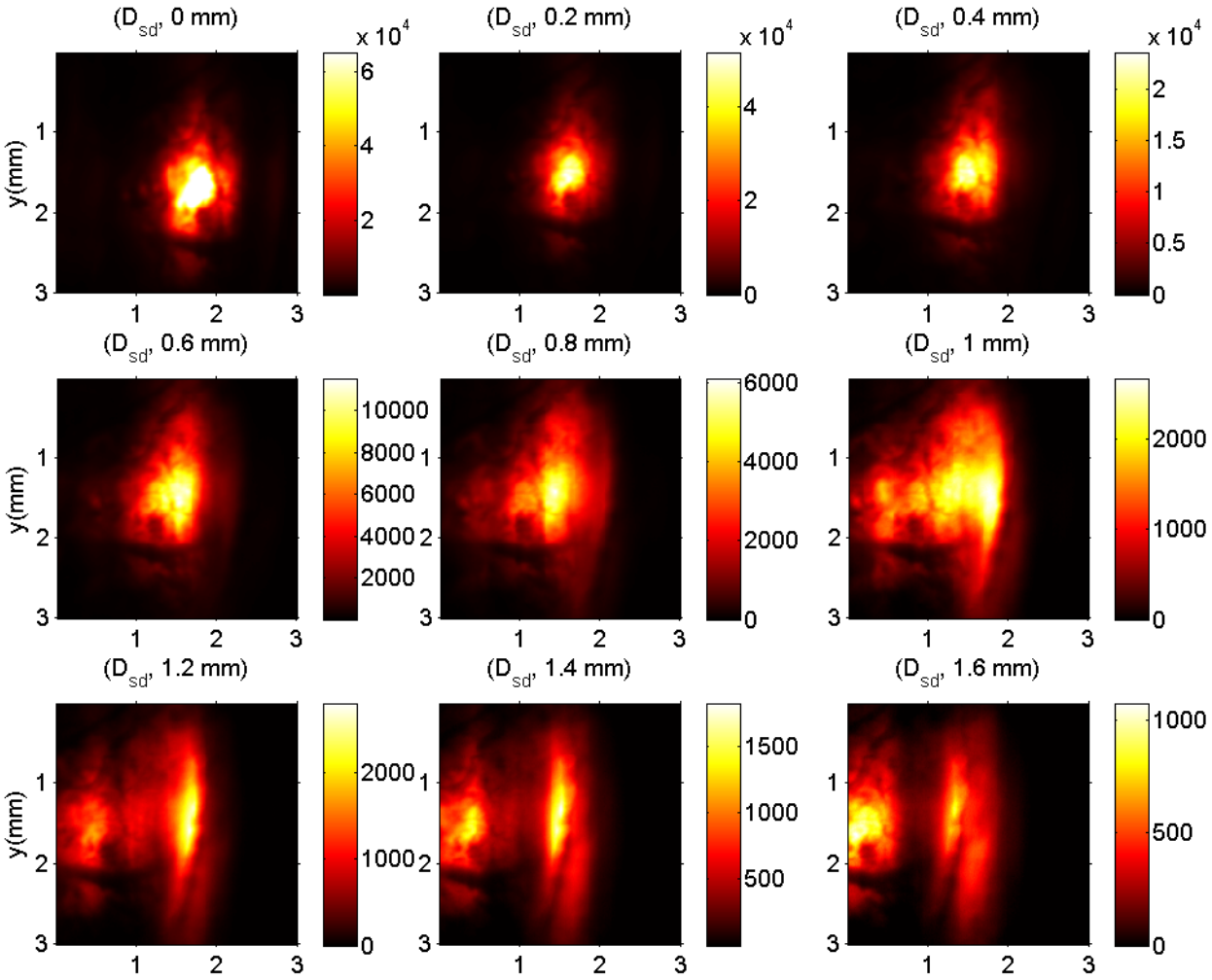

Figure 3.16: Experimental data of an in-vivo scan of a rat brain with the injection depth of $0.8mm$ and injection volume of $0.2\mu l$ in the right hemisphere and recorded through thinned skull.

prepared around the injection site and imaged under a confocal microscope.

In Figure 3.16, the experimental raw data from an in-vivo scan of a rat brain with the injection depth of $0.8mm$ and injection volume of $0.2\mu l$ in the right hemisphere is shown. For this experiment, the image reconstruction results are summarized in Figure 3.17. Panel (A) in this Figure shows the confocal image of the rat brain slice transfected by GFP and a 2D cross-section of the reconstructed fluorescent distribution is shown in panel (B). Panel (C) shows the axial distribution of GFP recorded by the single optical fiber probe system and the superimposed image of the reconstruction result and the confocal microscopy image

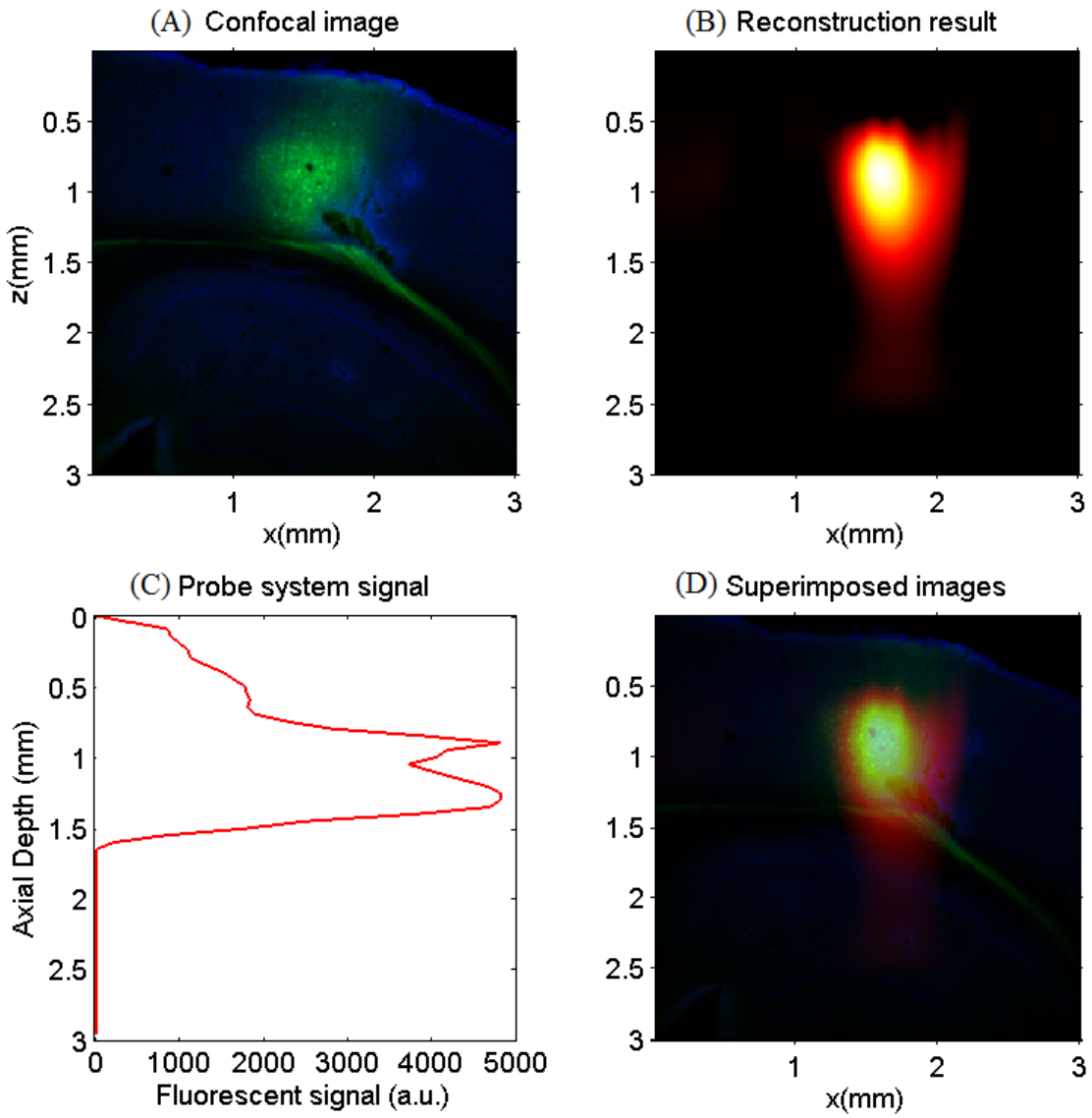

Figure 3.17: Experimental data from an in-vivo scan of a rat brain with the injection depth of $0.8mm$ and injection volume of $0.2\mu l$ in the right hemisphere, (A) a confocal image of a rat brain slice expressing GFP on the right hemisphere at the depth of $800\mu m$, (B) fluorescent reconstruction result, (C) curve displays fluorescence signal as a function of depth detected by the single optical fiber probe system, (D) the superimposed image of the reconstruction result and the confocal microscopy image.

is shown in panel (D). Another reconstruction result of *in-vivo* experiment is shown in Figure 3.18 where a rat brain was injected on the left hemisphere at the depth of $800\mu m$ with injection volume of $0.2\mu l$. In both experiments, the fluorescent reconstruction results are in good agreement with the data from the probe system and also the corresponding confocal

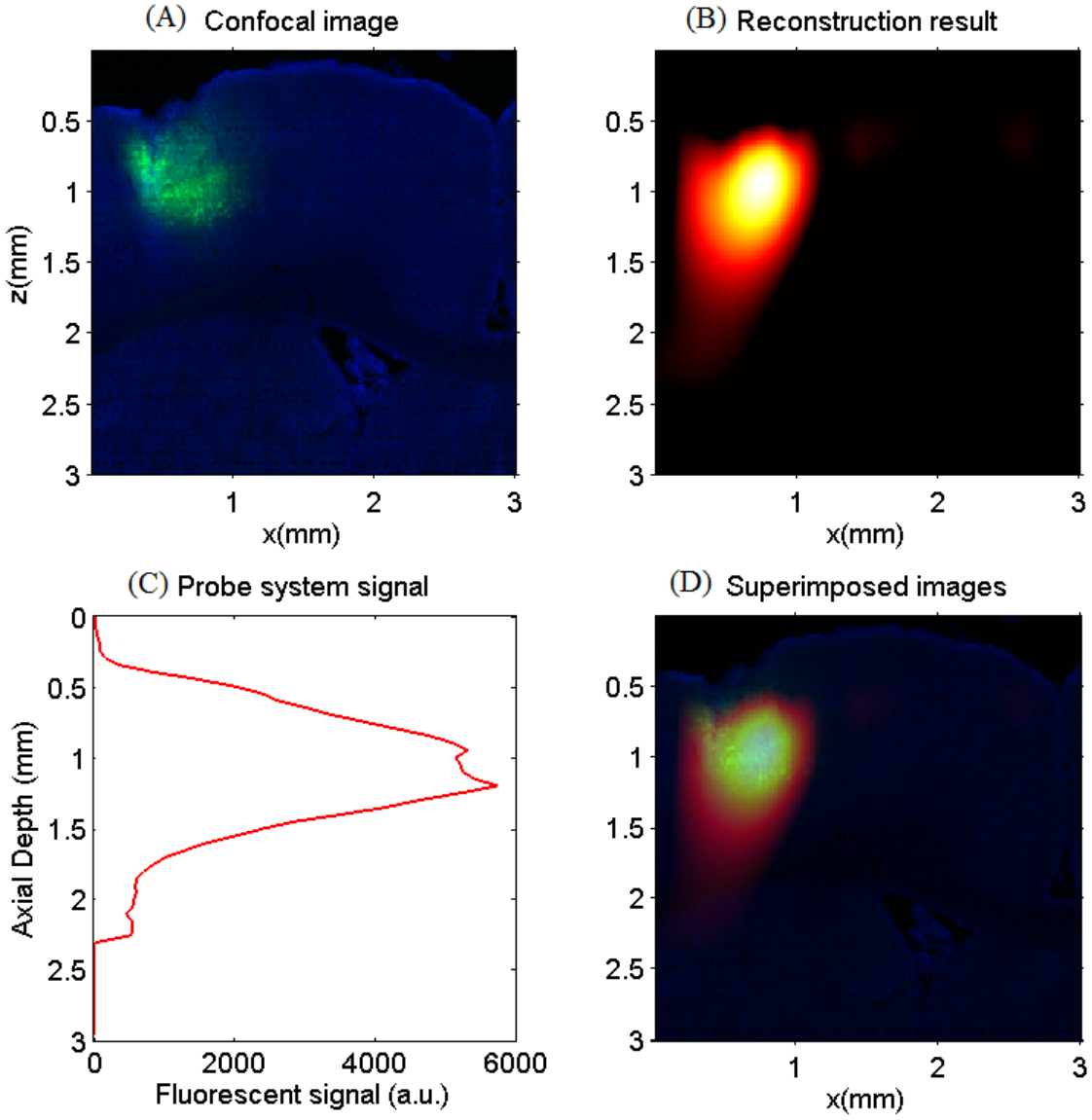

Figure 3.18: Experimental data from an in-vivo scan of a rat brain with the injection depth of $0.8mm$ and injection volume of $0.2\mu l$ in the left hemisphere, (A) a confocal image of a rat brain slice expressing GFP on the right hemisphere at the depth of $800\mu m$, (B) fluorescent reconstruction result, (C) curve displays fluorescence signal as a function of depth detected by the single optical fiber probe system, (D) the superimposed image of the reconstruction result and the confocal microscopy image.

microscopy images.

Despite the fact that all the animals were carefully injected at specific depth with pre-defined volumes, in few cases the gene delivery or expression were not successful and almost no fluorescent signal was detected by the FLOT system. Figure 3.19 shows the experimental

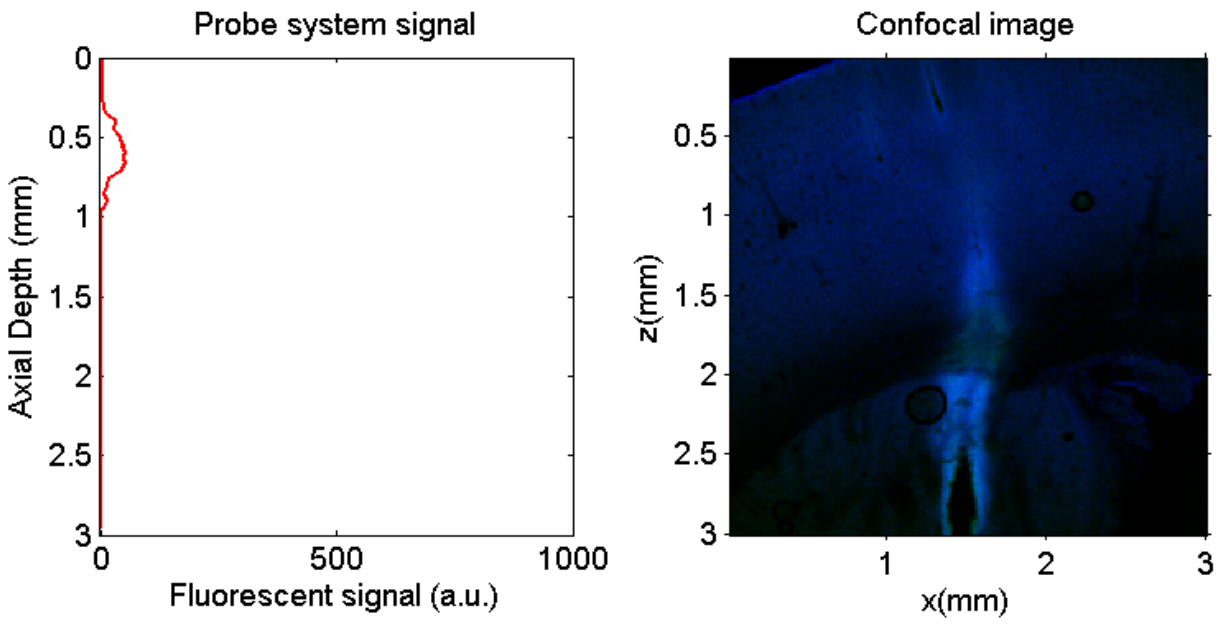

Figure 3.19: (A) Curve displays fluorescence signal as a function of depth detected by the single optical fiber probe system, (B) confocal image of a rat brain slice injected on the left hemisphere at the depth of $800\mu m$.

results from a case that almost no fluorescent signal was detected by the FLOT system. The probe system curve and also confocal microscopy image of the brain slice also confirms that the gene delivery or expression of fluorescence protein has not been successful. These experimental results prove that such a tomography system has the potential to provide valuable information regarding the depth and level of the expression of optogenetic proteins prior to the experiments.

Conclusion

In this chapter, the details of the developed fluorescent laminar optical tomography (FLOT) system was discussed and typical reconstruction results in both phantom and *in-vivo* rat experiments were presented. For phantom experiments, the actual depth of micro-channels buried inside a highly scattering medium was determined using a costume-made SD-OCT system and the reconstruction results using the FLOT system was in good agreement with the OCT measurements.

The *in-vivo* animal experiments were conducted in thinned-skull rats which were injected to develop green flourescent protein (GFP) in the cortical tissue at different depths. Two different mechanisms were employed to compare the FLOT results with the actual distribution of GFP. In the first step, a single optical fiber probe system which was developed in the lab [30] was employed during the experiments to define the axial distribution of the GFP from the injection site. Then, the brain tissue was extracted and several slices were imaged under a confocal microscope. The *in-vivo* experiments also showed promising results in employing the FLOT system for noninvasive imaging of fluorescent proteins during optogenetic experiments. One approach to increase the imaging depth is to use fluorescent proteins with red/near-infrared shifted excitation spectrum, such as tdTomato and mCherry [111, 112].

Such a tomography system has some advantages and shortcomings: it is a relatively simple and inexpensive system but only suitable for imaging superficial fluorescent samples. This system has a imaging depth limited to $2mm$ and its resolution drops by increasing the depth. Therefore, designing a fluorescent tomography system with deeper imaging capability and higher resolution is desirable. In the next chapter, details of a digital optical phase conjugation (DOPC) system [16] is discussed which is able to focus light far deep inside a highly scattering medium and perform deep brain fluorescent imaging. This system also provides a method to deliver light deep inside the brain tissue for neurostimulation applications which are not feasible using conventional techniques because of the high level of scattering in most tissue samples.

Chapter 4

Focusing Light Through and Inside Highly Scattering Mediums

4.1 Introduction

The high level of scattering in biological samples is known as the major obstacle in deep tissue optical imaging. Although scattering of diffused photons is a random process characterized by the optical properties of a turbid medium, it has been proved that the wavefront perturbation is partially time-reversible even in a highly scattering specimen. Empirical algorithms were developed recently to focus light through scattering samples by using iterative wavefront optimization [85] or open-loop digital optical phase conjugation (DOPC) [81] methods. To bring a coherent beam of light into focus inside a scattering medium, converging ultrasound waves synchronized with pulses of laser were used to generate virtual sources of light within the tissue at arbitrary depths [16]. The ultrasound waves tag diffusing photons that pass through the focal point of the system. Tagged photons are discernible at the surface and can be collected to measure the wavefront of photons that scatter from any depth inside the tissue. By reversing this wavefront, we can generate laser pulses that come into focus at the same depth [16, 103, 104]. Such a platform was used to produce three-dimensional fluorescent images inside biological tissue ex-vivo with lateral resolution of about $50\mu m$ covering the depth up to $2.5mm$ [16]. Bringing light into focus at further depths, particularly via DOPC, provides new opportunities to develop systems where the objective is to deliver most of the incident light to a target site inside tissue while minimizing the exposure at the off-target areas. Potential applications of this approach are laser surgery

and phototherapy or optogenetic stimulation of genetically targeted neurons in nervous systems of different species [23, 24, 25].

In this chapter, first we review different approaches proposed to focus light *through* and *inside* highly scattering mediums. Then, the results of the turbidity suppression in highly scattering mediums obtained from our custom-made digital optical phase conjugation (DOPC) system is presented. At the end of this chapter, conclusions and suggestions for future works are given.

4.2 Wavefront shaping

Focusing light *through* a scattering medium

It is shown that by modulating the wavefront of a coherent light source it is possible to suppress the turbidity and focus light through a highly scattering medium [85]. In this work, a spatial light modulator was employed to control the wavefront of a laser beam and focus it through an opaque medium. If a plane wave hits a highly scattering medium, the transmitted light constructs random speckle patterns on the detector, while by modulating the wavefront of the input beam, coherent light can be focused at an arbitrary spot on the other side of a highly scattering medium. In this method, the whole area of a spatial light modulator was divided to N super-pixels. The electric field at the target point,E, is the superposition of all N electric fields resulted from the defined super-pixels on the SLM [85]:

$$E_m = \sum_{i=1}^{N} t_{mn} A_n e^{i\phi_n}, \tag{4.1}$$

where A_n and ϕ_n are the amplitude and phase of the light reflected from the nth super-pixel of the SLM, respectively. In this equation, the impact of scattering medium on transmitted light is modeled using the complex number t_{mn}. Amplitude of the focused light is maximum if all fields at the target point have the same phase. In this method, the phase of each

segment was changed between 0 and 2π and by getting a feedback signal from a CCD camera, the optimum phase of the corresponding segment, which produces highest intensity, was recorded. By repeating this procedure for all the SLM segments, the optimal phase mask was obtained. By loading this phase mask on the SLM, the incident light is focused after passing through the scattering medium. The sequential nature of this algorithm translates to a time consuming optimization procedure. A parallel wavefront optimization algorithm is studied in [86] where the SLM area was divided into two random partitions, and while the light intensity was monitored using a CCD camera, the phase of each partition was changed with respect to other partition. At each iteration, half of the pixels were modulated; therefore, the change in light intensity at the target point was more than the case where just one super-pixel was modulated. Consequently, in this method, the signal to noise ratio was improved as well. In another attempt to reduce the optimization time [96], the SLM area was divided to 16 different super-pixels and by simultaneous phase modulation of each section at a unique frequency and recording the output signal using a CCD camera, a parallel wavefront optimization algorithm for focusing light through scattering mediums was developed. In a similar work [97], a parallel wavefront optimization technique based on spatial frequency modulation was proposed which is able to complete the optimization procedure in less than $400ms$.

By having the transmission matrix of a scattering medium, the relationship between the input and output optical modes are defined [87]. The transmission matrix (TM) of a medium can be defined using an array of sources and sensors. For acoustic waves, the sensors are simply an array of microphones used to reconstruct the transmission matrix and time reversal (TR) [84]. The reconstruction of TM for lightwave is discussed in [87]. In their method, pixels of a CCD camera were defined as sensors and a phase-only spatial light modulator is used as a wavefront shaping tool. The transmission matrix, K, is consisting of complex coefficients K_{mn} which relates the optical field (Amplitude and phase) of mth output mode to the nth input mode. In [87], SLM and CCD were divided to $N = 256$ different super-

pixels. To obtain the TM, the distorted sample wavefront was interfered with a reference wavefront (plane wave) and by employing phase shifting holography technique [95], the phase information of the unknown field was extracted. In phase shifting holography, the scattered wavefront with unknown profile (E_{sc}) is interfered with a reference beam E_{ref} and the complex field, consisting of amplitude and phase information, is calculated by employing equation 4.2 and 4.3, respectively:

$$|E_{sc}(x,y)| = \frac{abs[(I_0(x,y) - I_\pi(x,y) + j(I_{3\pi/2}(x,y) - I_{\pi/2}(x,y))]}{4|E_{ref}|}, \tag{4.2}$$

$$\delta\phi(x,y) = arg[(I_0(x,y) - I_\pi(x,y) + j(I_{3\pi/2}(x,y) - I_{\pi/2}(x,y))], \tag{4.3}$$

where $I_0, I_{\pi/2}, I_\pi, I_{3\pi/2}$ are the recorded intensities of interference patterns while the phase of the reference beam is shifted by $0, \pi/2, \pi, 3\pi/2$, respectively.

Even though this method is much faster than previous iterative methods [85], but for biological tissue where the decorrelation time is in the range of few milliseconds [88], still it cannot meet the criteria. In [88], a high-speed phase mask optimization technique, which utilizes off-axis binary-amplitude computer-generated holography based on a deformable mirror device (DMD) is proposed and the wavefront optimization was achieved in less than $40ms$.

In 2008, for the first time, the concept of optical phase conjugation (OPC) was employed for turbidity suppression and focusing laser through biological samples [83]. The basics of OPC is similar to holography techniques. Phase conjugate mirror (PCM) is a term used for devices that produce phase conjugate of a field [89]. The concept of PCM and its difference compared to a regular mirror is shown in Figure 4.1 where PCM reflects the incident beam along the incident direction but conjugated wavefront. Figure 4.2 illustrates the concept behind the optical phase conjugation process [90]. Analog PCM is basically a birefringent crystalline material and to perform as an OPC device, it requires two anti-parallel pumping beams where they fulfill the phase matching condition: $K_1 + K_2 = 0$. In the case of phase

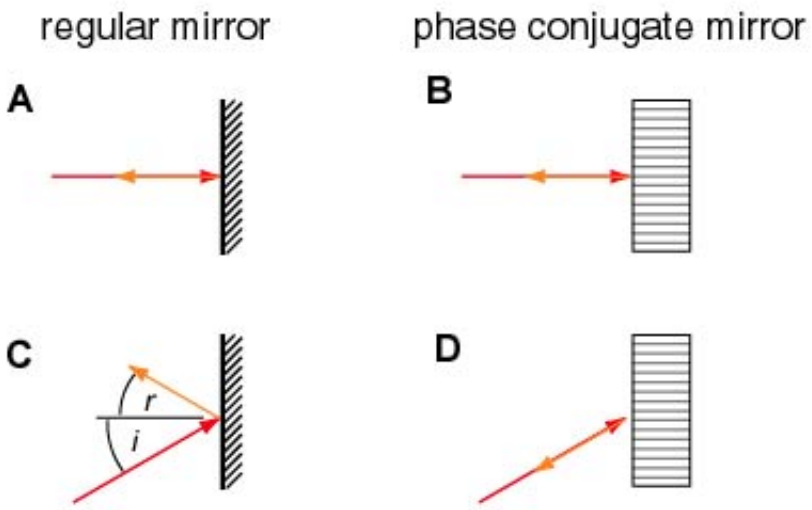

Figure 4.1: Difference between a regular mirror (A),(B) and a phase conjugate mirror (C),(D). Regardless of the incident angle, the PCM reflects the beam along the incident direction but conjugated wavefront [90].

matching between the pumping beams, if a probe wave, B_3, is projected on a PCM from any direction, it's phase conjugated version will be reflected from the mirror and it results in $K_3 + K_4 = 0$.

Focusing procedure using the OPC methods consists of two sequential steps: first recording the tissue turbidity information and then reconstructing the phase conjugated beam [83]. While using nonlinear optics based on OPC seems to be an attractive method for turbidity suppression, it still has some shortcomings [81]: it has a limited phase conjugate reflectivity which is defined as the power ratio of phase conjugated beam to the input beam. Besides, this method needs special light sources and nonlinear mediums. Therefore, a more flexible method capable of operating with different light source types and power levels is desirable [81].

In 2010, digital optical phase conjugation (DOPC) setup based on a liquid crystal spatial light modulator was developed [81]. This method has two main advantages over the nonlinear optics based optical phase conjugate approach: the efficiency of phase conjugation is independent of the input signal, the power of the conjugated beam can be adjusted based

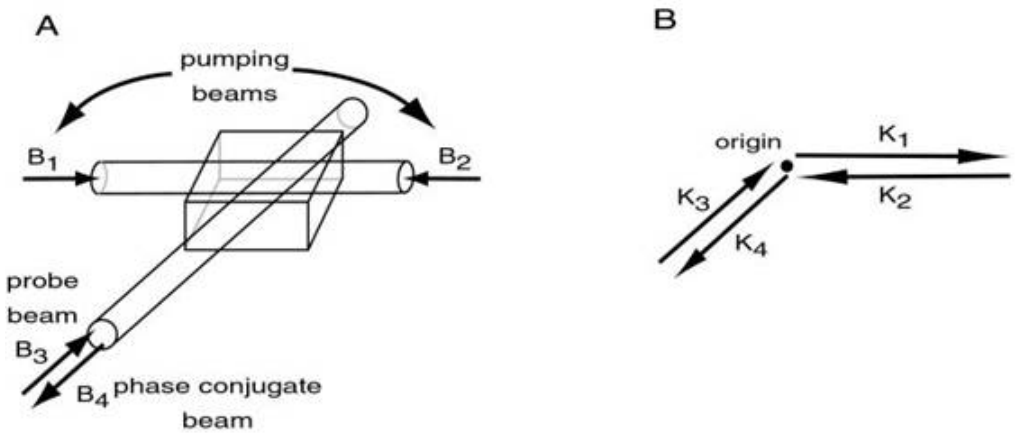

Figure 4.2: (A) The operation of PCM is based on illuminating a nonlinear optical element with two anti-parallel pumping beams, B_1 and B_2, (B) when $K_1 + K_2 = 0$, any probe beam (B_3), projected on the mirror, reflects in the same path with conjugated phase profile [90].

on specific applications, and it can operate using different types of light sources such as continuous wave (CW) or pulsed laser. This method is also consisting of two steps: recording the wavefront information of the scattered sample beam using a CCD camera, and then, generating the phase conjugated wavefront using a phase-only SLM. These two steps are described in Figure 4.3. Since our optical phase conjugation setup is based on DOPC, more details of its architecture is presented in section 4.3.

In a DOPC setup, the ideal case is to have a device which can extract the phase information (sensor), and at the same time, functions as a spatial light modulator (actuator) [81], like ultrasound transducers. But for optical applications, such a device does not exist. Therefore, in a DOPC system the sensor and actuator, which are two different devices, need to be perfectly aligned in a way that they form a virtual image on each other. As it is shown in Figure 4.3, first a sample beam which has unknown phase information is interfered with the reference beam and the resulted hologram is recorded by a sCMOS camera. By employing the phase shifting holography method [95], phase information of the scattered beam is extracted by equation 4.3. Desired phase shifts during phase shifting holography is produced by an electro-optic modulator (EOM). Then, the conjugated phase profile is loaded on the SLM and as the reference beam hits the surface of the SLM, the modulated wavefront is sent

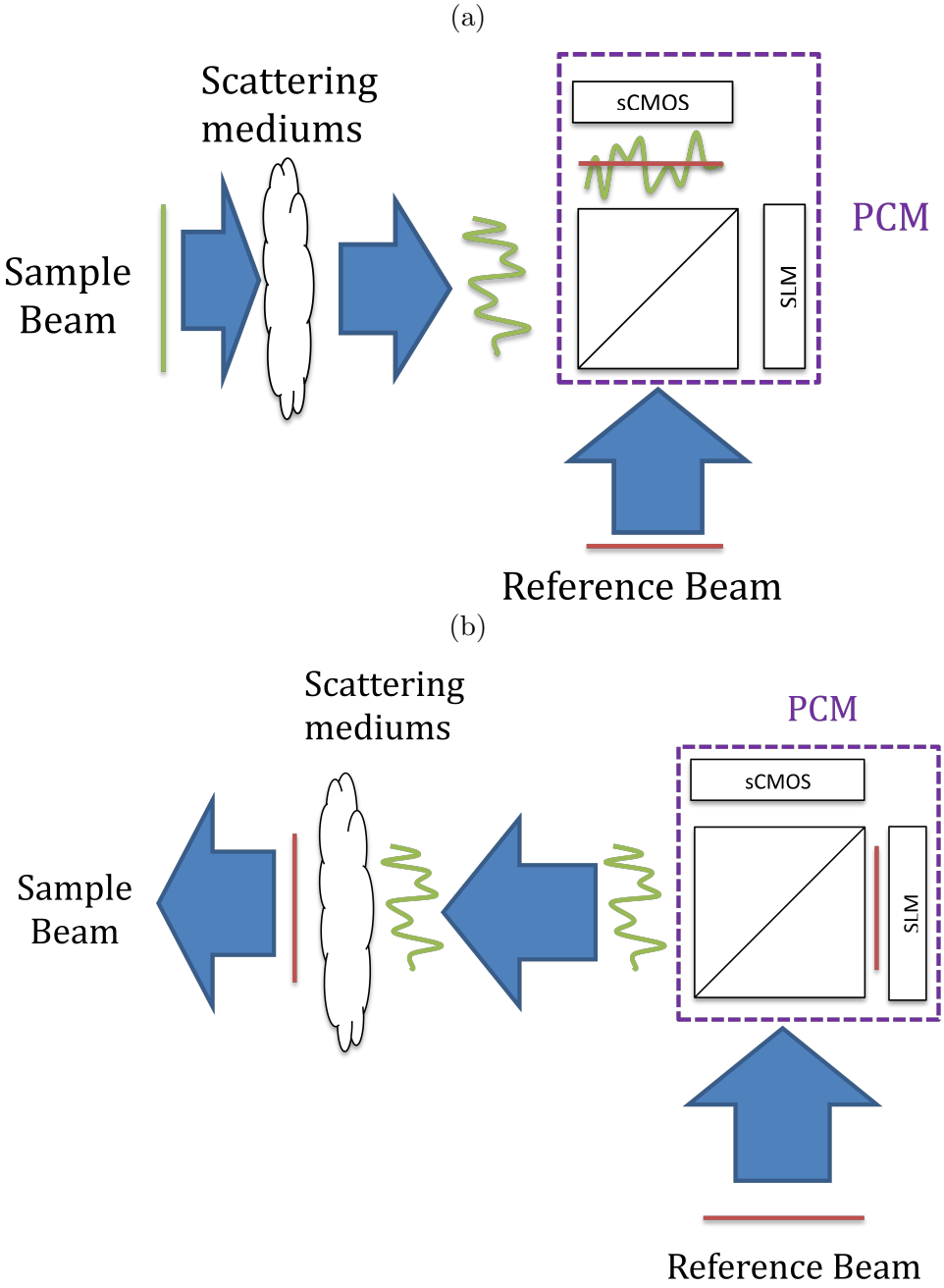

Figure 4.3: Optical phase conjugation consists of two steps, (A) extracting the phase information of distorted sample beam by employing techniques such as the phase shifting holography, (B) sending the phase conjugated version of the sample beam toward the scattering medium by employing spatial light modulators.

toward the sample.

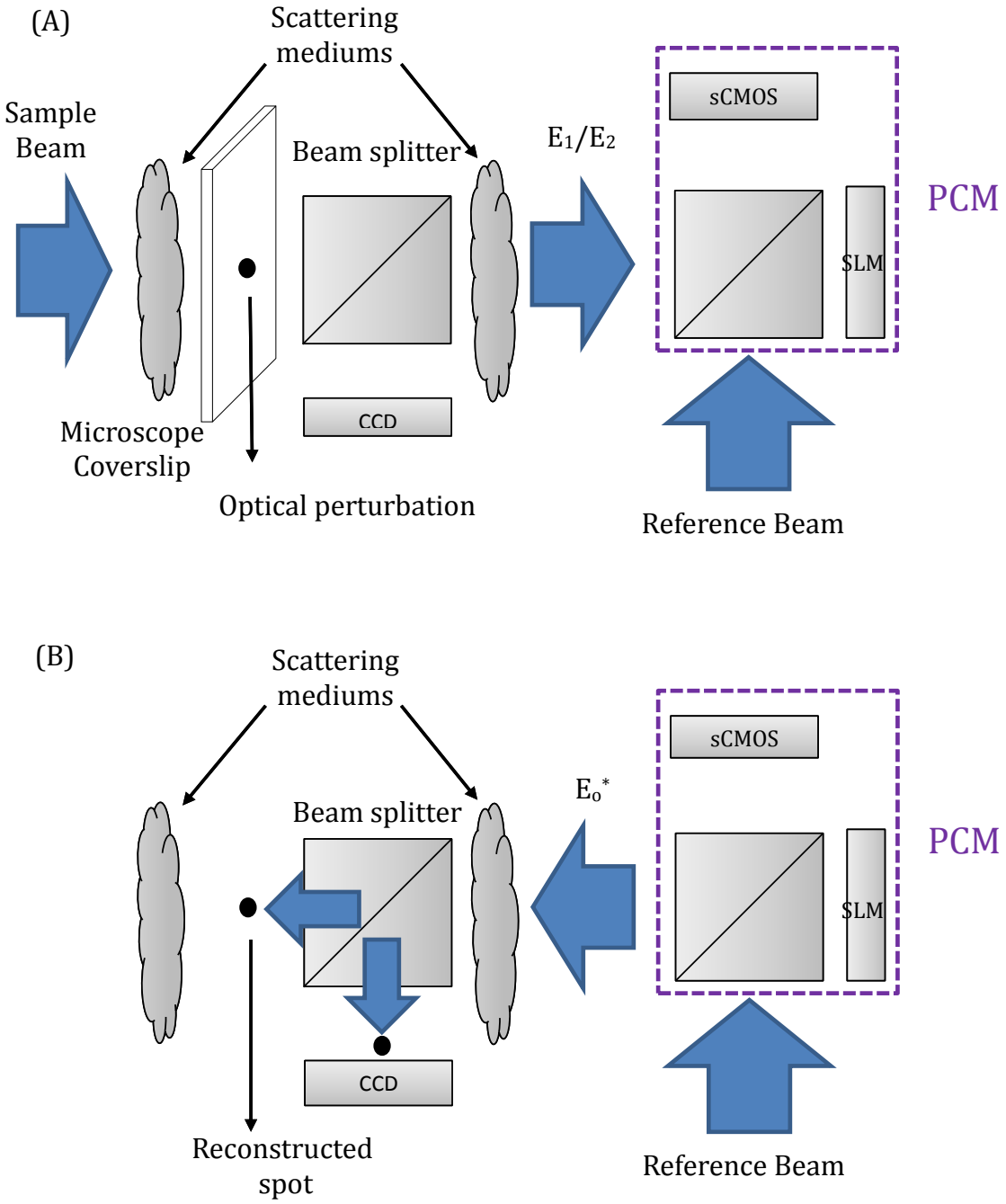

Figure 4.4: Schematic of the TRAP, TRACK systems [99, 100] to focus light inside a highly scattering medium: (A) recording step, where fields at time steps t_1 and t_1 are measured using phase shifting holography technique when sample was in the system and removed, respectively, (B) playback step, where the phase conjugated beam, $E_o{}^*$, is sent back toward a scattering medium.

Focusing light *inside* a scattering medium

In the last section, different methods for turbidity suppression and focusing light *through* scattering mediums were discussed. These methods are categorized into two different approaches, *closed-loop* and *open-loop*. Developed algorithms to focus light *inside* scattering mediums can also be classified to the same categories as discussed in the following section.

For optical imaging applications, mainly fluorescent imaging in this work, we need to focus light inside rather than through a scattering medium. In most methods proposed to focus light through a scattering medium, a CCD camera is employed to provide feedback signals to accomplish wavefront shaping. Therefore, to focus light inside a scattering medium where taking a direct feedback from the target area is not practical, which mechanism can be used? In [92], nano-scale fluorescent particles were buried inside a scattering medium to provide a feedback signal for the wavefront shaping procedure. Their setup and algorithm were similar to the iterative method employed for focusing light through a scattering medium [85]. The difference is that the feedback signal was provided indirectly from the amount of fluorescent signal emitted from the fluorescent particle captured by a detector (EMCCD camera). One drawback of the fluorescent guided method is that in practical applications, like biomedical imaging, delivering such fluorescent particles is an invasive procedure and it is not the best option.

Photoacoustic-guided approach was proposed in [98]. This approach uses iterative wavefront shaping algorithm similar to the one in [85, 91] and the feedback signal to evaluate the performance of the algorithm was provided by a photoacoustic signal at the target area. The photoacoustic effect is defined as the generation of ultrasound waves caused by irradiating a medium by ultrashort laser pulses [94]. When laser is absorbed by the medium, ultrasound waves are induced as a result of the transient thermoelastic expansion. The amplitude of this signal at each position is proportional to the energy deposited at that spot [94]. In their setup, deformable mirror is employed for wavefront shaping, and graphite particles are used as absorbers. During the wavefront shaping process, as the intensity of laser increases at

the target area, the transducer generates stronger signal and the optimum phase pattern to focus light inside the medium can be extracted. The advantage of this method is that it provides a *non-invasive* technique, but it is an iterative and time consuming process and cannot be applied to *in-vivo* experiments.

An open-loop approach to focus light inside a scattering medium, called *time-reversed ultrasonically encoded* (TRUE) method, was proposed in [15]. In this method, an ultrasound transducer is employed to encode photons passing through the focal point of a ultrasound transducer. Due to the acousto-optic modulation (AOM), photons passing through the focal point are frequency shifted ($f_0 + f_U$) and provide a virtual *guide star* inside a scattering medium. After extracting the phase information of the tagged photons, a phase conjugate mirror (PCM) is used to time reverse the tagged photons and focus the beam at the target spot. The principle of the TRUE method is similar to the approach in [83] which was discussed in last section with this difference that in the TRUE method, only ultrasonically encoded photons interfere with the reference beam. The drawback of this method is that the energy of the time reversed signal cannot exceed the energy of the ultrasonically encoded light which is a small portion of the whole irradiated light onto the sample. Hologram fixing could be a potential solution to increase the gain of system [15].

DOPC setup has this advantage that the gain of system is independent of the sample signal which usually is a weak signal. In [16], deep tissue fluorescent imaging based on ultrasonically encoded light and DOPC was proposed. In this method, ultrasound transducer was used to encode the light passing through the focal point of ultrasound transducer and in the phase conjugation step, DOPC method was employed. In this setup, high intensity nanosecond laser pulses of frequency f_0 irradiate the scattering sample and due to AOM phenomenon, a portion of the photons that pass through the focal point of the ultrasound transducer will be frequency shifted ($f_0 + f_U$). Phase information of the tagged photons is extracted by employing the phase shifting holography method. To generate a static interference pattern on the detector, the reference beam is frequency shifted using an AOM device.

The PBR of such a system is calculated by equation 4.4 :

$$PBR_{Phaseonly} = \frac{\pi(N-1)+1}{4M}, \tag{4.4}$$

where N is the number of available optical modes on the spatial light modulator and M is the number of uncorrelated optical modes modulated at the focal point of the transducer. To increase the PBR, the number of optical modes passing through the focal point are reduced by using a transducer with smaller focal point.

All optical approaches to focus light inside a scattering medium is discussed in [99, 100]. In the method described in [99], time reversal by analysis of changing wavefronts from kinetic targets (TRACK), motion of a target area is employed as a guide star. In a similar approach, the time-reversed adapted-perturbation (TRAP)[100] was used to focus light dynamically on moving targets buried inside a scattering medium. These approaches require recording dynamic light fields in two separate instances t_1 and t_2, when the field changes from E_1 to E_2, respectively. By subtracting these two fields and conjugating the resulted field, $[E_1 - E_2]^*$, light is focused on the target. Schematic of this method is shown in Figure 4.4. In the first step, $E_o = [E_1 - E_2]$ is measured, and in the second step, the phase conjugated version of the field, $E_o{}^*$, is sent back toward the sample and is focused on the target position. In this setup, part of the focusing beam is monitored by employing a CCD camera. Some potential applications of these methods are photoablation of angiogenic vessels in tumors [99] or *in-vivo* cytometry [100].

4.3 Experimental results

Focusing light *through* a scattering medium

Optical phase conjugation consists of two steps: extracting phase information of the scattered light passing through a sample by employing a scientific camera, and then, employing a SLM

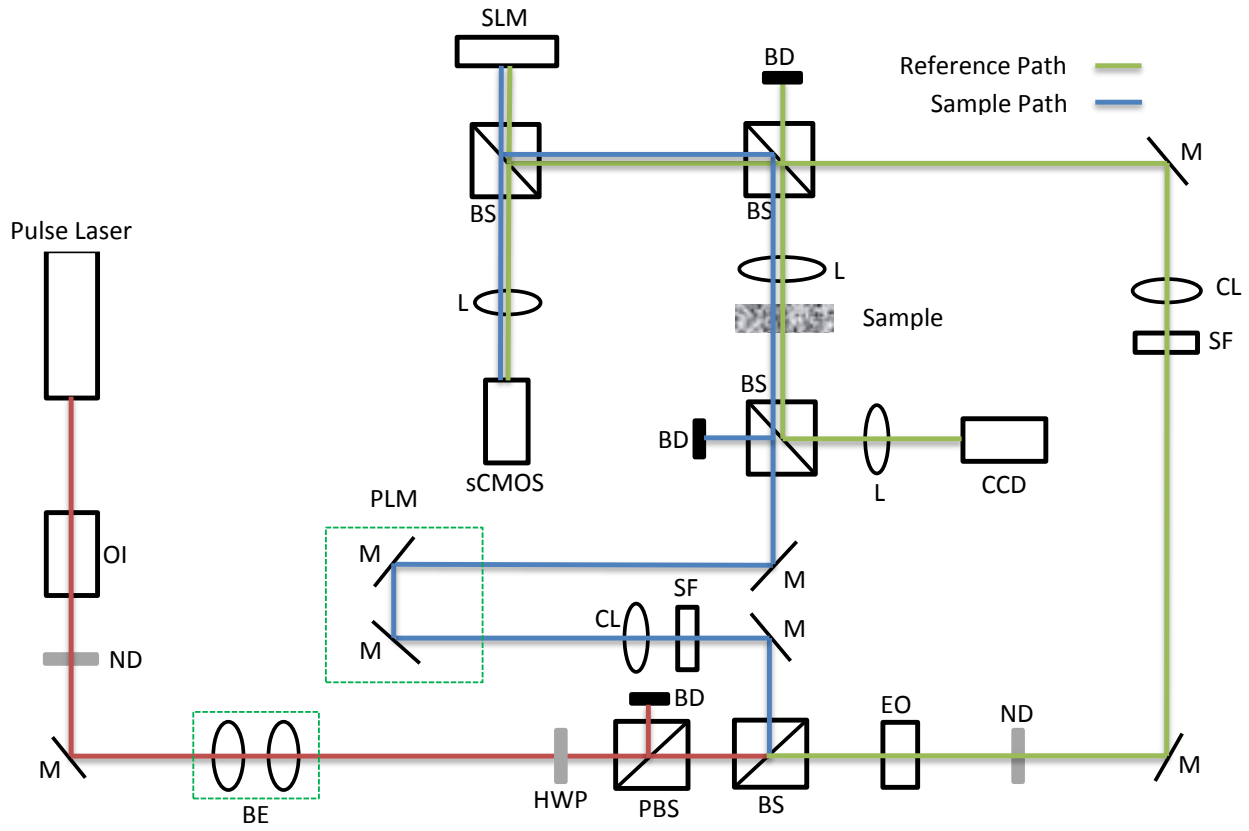

Figure 4.5: Schematic of the developed DOPC system: pulsed laser source (PLS), optical isolator (OI), mirror (M), beam expander (BE), half-wave plate (HWP), polarizing beam splitter (PBS), beam splitter (BS), electro-optic modulator (EO), neutral density filter (ND), spatial filter consist of a single mode optical fiber (SF), collimating lens (CL), microscope objective (MO), spatial light modulator (SLM), path length match (PLM), Beam dump (BD), scientific CMOS camera (sCMOS), sample (S), achromatic lens (L).

to modulate the reference beam and produce the conjugated version of the sample beam. Schematic of the implemented digital optical phase conjugation system is shown in Figure 4.5.

The active area of the SLM used in this study (LETO, Holoeye, Germany) consists of an array of 1080×1920 pixels which were registered pixel-to-pixel on a camera sensor array (sCMOS, Zyla, Andor) using an imaging lens mechanism made from two achromatic lenses in the form of a *Plossl* lens compound. To produce intensity pattern of the active area of SLM on the sCMOS, the whole area of SLM was divided to 54×96 blocks with 20×20 pixels in each block. Then, the phase difference between the adjacent blocks were set to π,

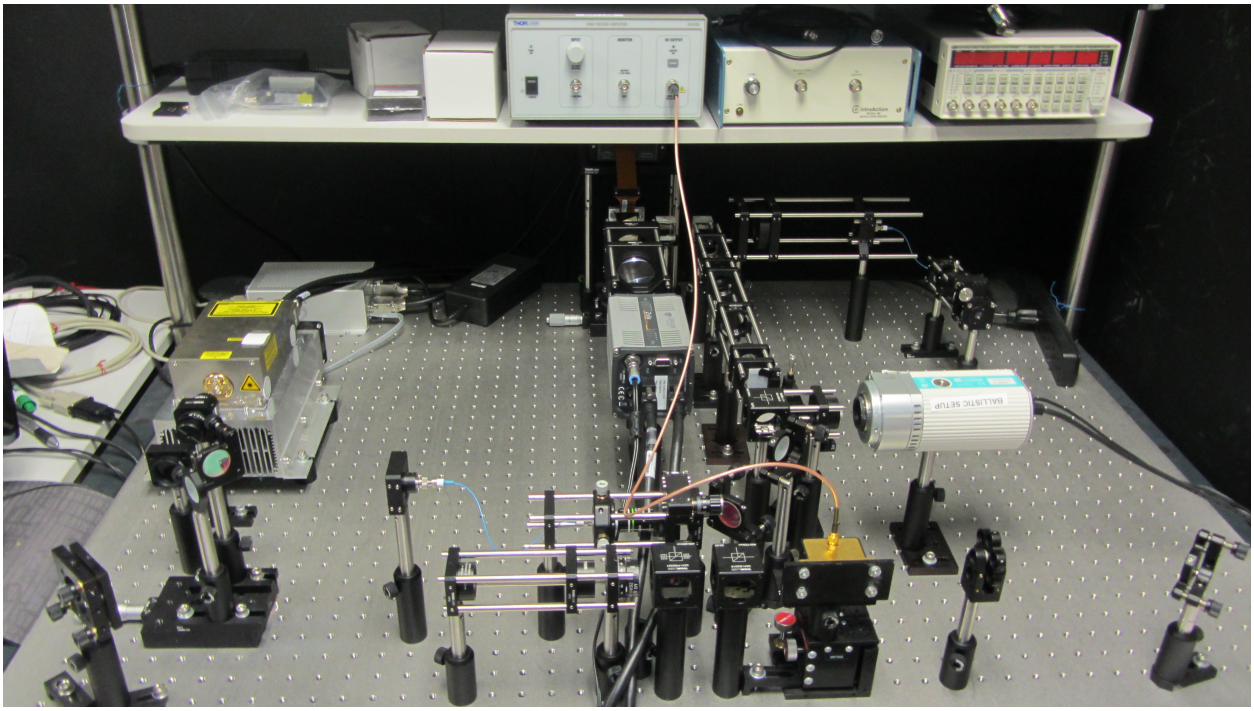

Figure 4.6: Experimental DOPC setup.

and as shown in Figure 4.7, it results in dark boundaries between the blocks on the captured image [81]. This intensity-based pattern is employed to detect some causes of misalignments between the SLM and sCMOS, such as tilt [101]. Since the SLM pixel size is smaller than the pixel size of the sCMOS, the distance between the SLM and the imaging lens was adjusted so that by providing the required magnification, the whole area of the SLM were exactly registered on the same number of pixels on the sCMOS. More details of the basic alignment steps are available in previously published papers [81, 82, 101].

A Q-switched laser source was pulsed at 40kHz (2W, 532 nm laser, Spectra-Physics) and its beam was split between a reference and a sample path via a beam splitter. To protect the laser from the back reflected beams, an optical isolator was used. Since the coherence length of the pulsed laser source is about $7mm$, a path length match arm consisting of two mirrors mounted on an one-axis positioner was used in the sample arm to match its optical path length with the reference arm to obtain a proper interference signal. The collimated sample beam was aimed toward a scattering medium and since there was a considerable

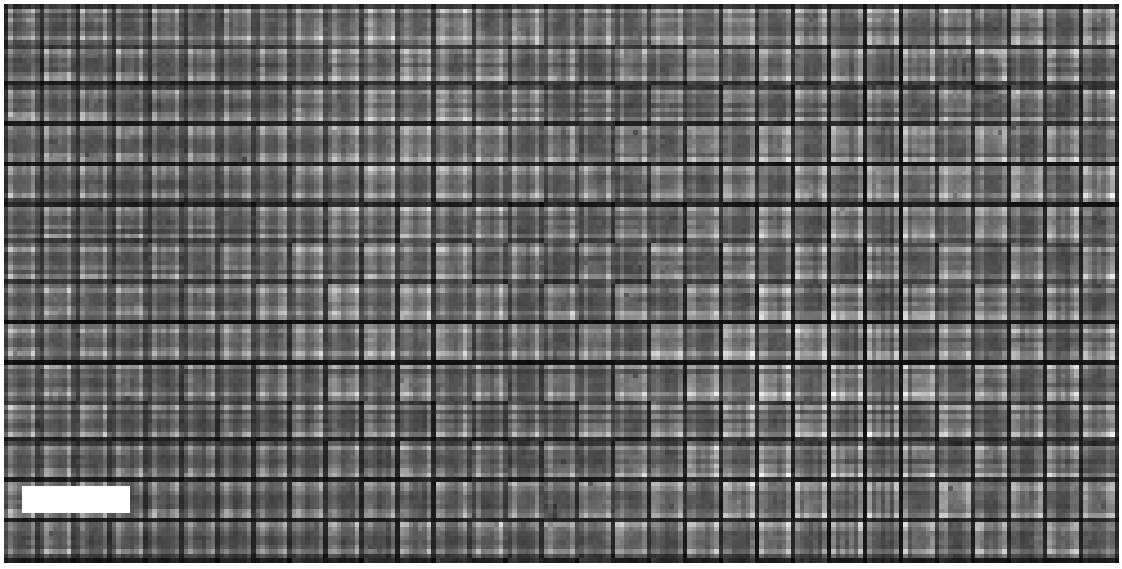

Figure 4.7: Intensity pattern of the SLM pixels imaged by the sCMOS camera. Scale bar, $380\mu m$.

distance between the sample and the optical phase conjugating (OPC) module (consisting of the sCMOS and SLM), the intensity of the scattered beam drops significantly. Therefore, a light collecting lens with focal length of $50mm$ was employed to image the light scattered from the surface of the sample to the SLM active area. To extract the phase information of the distorted light, the sample beam was interfered with the reference beam and the resulted hologram was recorded with the sCMOS camera. This step was performed based on the four-phase shifting digital holography technique [95], where the Electro-optic (EO) module is used to cycle the phase difference between the reference and sample beam $(0, \pi/2, \pi, 3\pi/2)$ and the resulted holograms were transferred to a computer to extract the phase information. To reduce the noise of the calculated phase, 10 holograms were recorded for each phase shift and averaged. After extracting the phase information, its conjugated phase profile was loaded on the SLM. In the play back step, the SLM reflects the modulated reference beam toward the sample.

To monitor the efficiency of the system in phase conjugation, quantified by the peak to background ratio (PBR), a beam splitter was placed in the sample path to reflect a portion of the reconstructed beam toward another CCD camera (QImaging EXi Aqua) which is

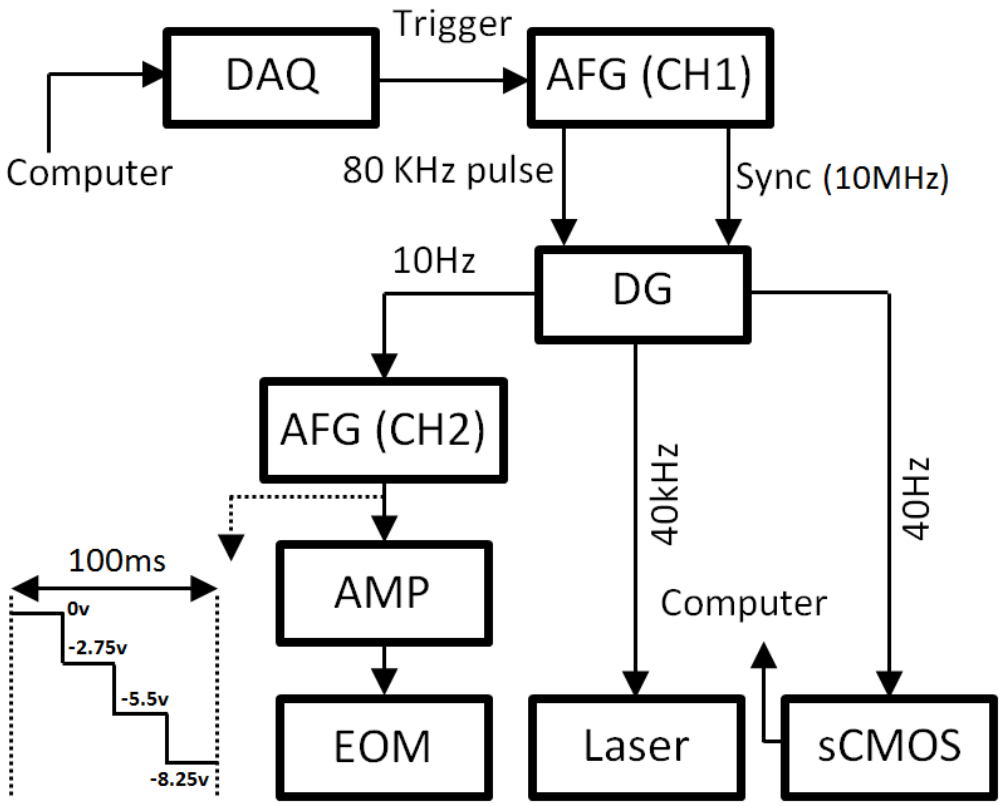

Figure 4.8: Timing block diagram of the implemented DOPC system. DAQ, data acquisition; AFG, arbitrary function generator; DG, delay generator; AMP, power amplifier; EOM, electro-optic modulator.

placed at the focal point of a lens. The PBR is defined by the ratio of the peak intensity at the focal point of the phase conjugated beam to the averaged background intensity when a random phase is loaded to the SLM [85]. The block diagram shown in Figure 4.8 illustrates the synchronization details of the system: the optical phase conjugation process starts by sending a trigger signal to an arbitrary function generator (AFG) through a data acquisition board which generates square pulses with frequency of 80kHz. A delay generator (DG645, Stanford Research Systems) generates three rescaled pulses with frequencies $40kHz$, $40Hz$, and $10Hz$ to drive the laser, scientific camera and the electro-optic modulator, respectively. Capturing and transferring the 40 holograms was completed within one second. In Figure 4.9, panel (A) shows the extracted phase profile of a Scotch tape sample, panel (B) and (C) are the images recorded by the CCD camera when a random phase pattern was loaded on the SLM and, after phase conjugation followed by the calibration process, respectively.

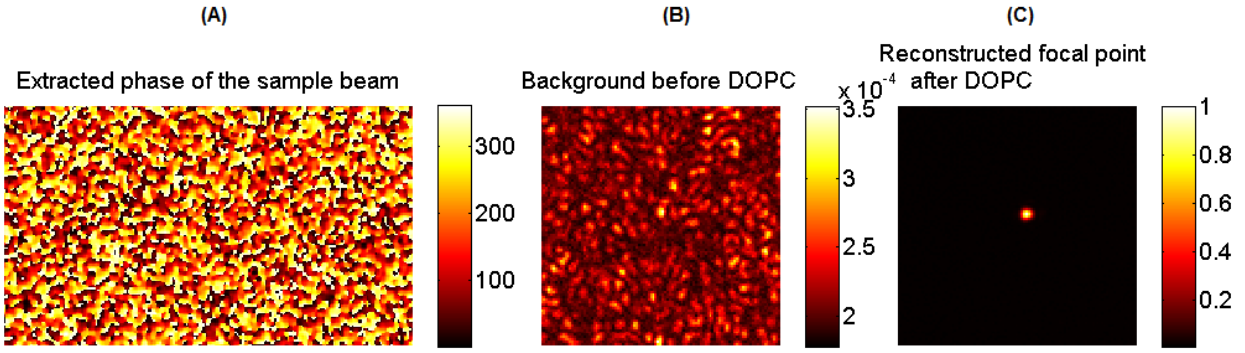

Figure 4.9: (A) Extracted phase information of the field passing through a scattering medium (five layers of Scotch tape) by employing four step digital holography technique, captured signal by the CCD camera (B) when a random phase pattern was loaded on the SLM, (C) after optical phase conjugation.

The theoretical value of the PBR can be calculated by $\frac{\pi P}{4S}$, where P and S are the numbers of active pixels on the SLM and autocorrelation area of the speckle pattern on the SLM [82], respectively. For the results shown in Figure 4.9, the measured PBR is ~ 32000. The autocorrelation area in this experiment was 3×3 pixels; therefore, the theoretical PBR is:

$$PBR_{Phaseonly} = \frac{\pi(1920 \times 1080)/(3 \times 3)}{4} \approx 181000. \tag{4.5}$$

The difference between the theoretical and experimental values is the result of misalignments in the system, the SLM curvature, and vibrations in the system.

Focusing light *inside* a scattering medium

The basic DOPC setup was modified slightly to implement the TRAP/TRACK system and the schematic is shown in Figure 4.4. In this experiment, two ground glass diffusers (DG10-600-MD, Thorlabs, NJ, USA) were used as scattering mediums and the guide star was created by adding drops of India ink on a small area on top of a microscope coverslip. To image the reconstructed spot, a beam splitter was placed between the scattering mediums, equidistant from the guide star and the CCD camera. In the first step, four phase shifting method was employed to extract fields while the absorber was absent (E_1) and when it was

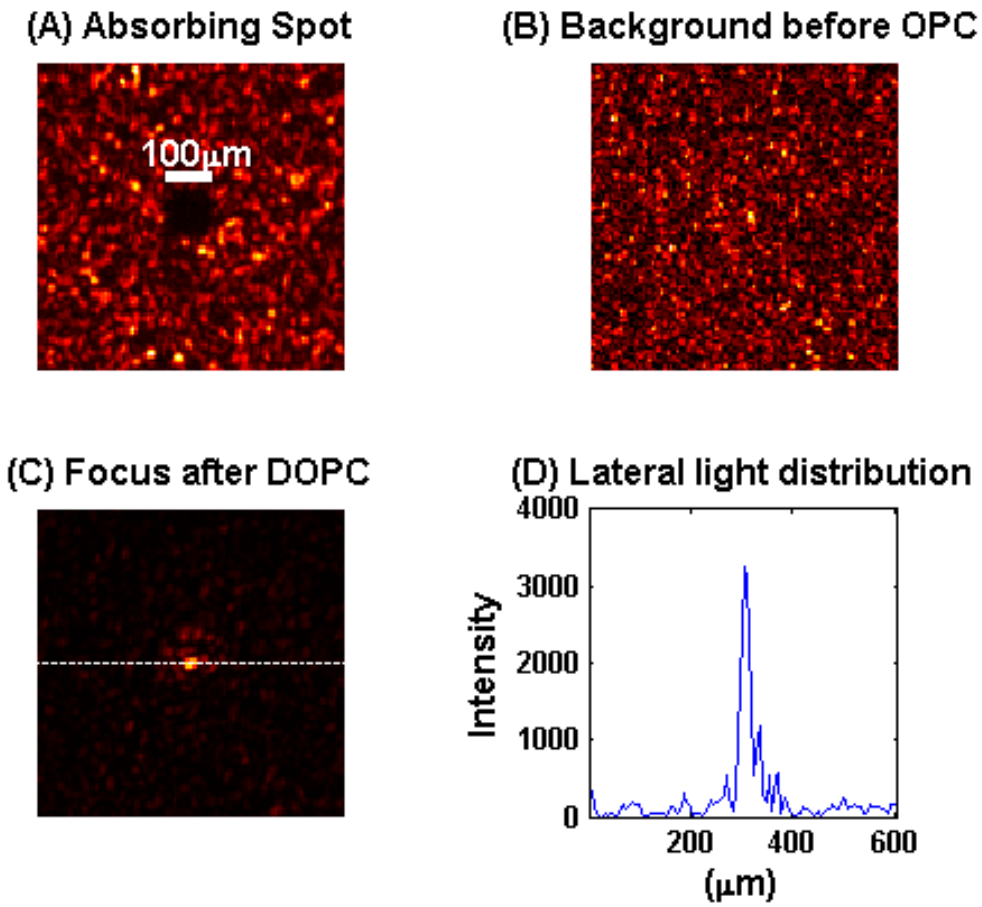

Figure 4.10: An absorber with diameter of $100\mu m$ was placed on top of a microscope slide and placed in the system which its schematic is shown in Fig. 4.4. (A) Image of the light perturbing object taken by the sCMOS camera, captured signal by the CCD camera (B) when a random phase pattern was loaded on the SLM, (C) after optical phase conjugation, (D) light intensity distribution along the line shown in panel (C).

present in the system (E_2). Then, the first field was subtracted from the second field and after extracting its phase information, the conjugated wavefront was sent back toward the sample.

Experimental results are shown in Figure 4.10 where panel (A) shows the dimension of the light perturbing sample on top of a microscope cover slide; panel (B) is the captured signal by the CCD camera while a random pattern was loaded on the SLM; the reconstructed focal point between the two scattering mediums after optical phase conjugation is shown in panel (C) and the lateral distribution of the reconstructed field along the focal point is shown

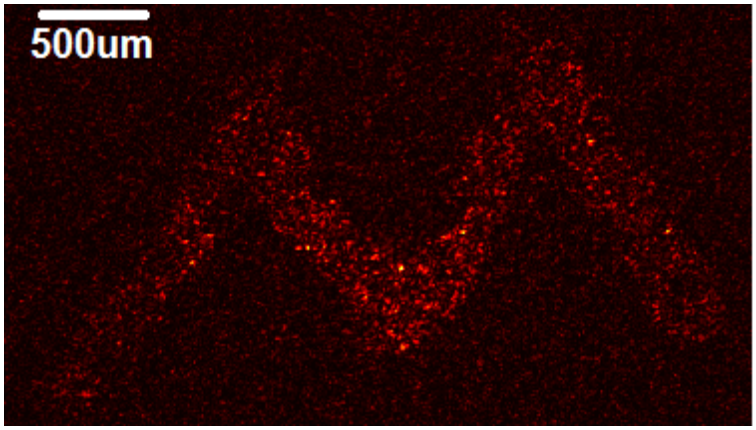

Figure 4.11: An absorptive pattern (letter 'M') was printed on a microscope slide and placed between two ground glass diffusers. Then, the DOPC system was employed to focus light on the virtual source.

in panel (D). For the results shown in Figure 4.10, the measured PBR was ~ 30. Based on equation 4.4, PBR of the system while focusing inside a scattering medium is related to the number of modulated optical modes by the guide star. By decreasing the area of virtual source and consequently the number of modulated optical modes, the PBR of the system can be increased [16].

In another experiment, an absorptive pattern (letter 'M') was employed in the system and the same procedure was repeated. The experimental results are shown in Figure 4.11.

4.4 Calibration of DOPC Setup Based on Orthonormal Rectangular Polynomials

This section is reproduced with some adaptations from the manuscript [102]:
Mehdi Azimipour, Farid Atry, and Ramin Pashaie, "Calibration of Digital Optical Phase Conjugation Setups Based on Orthonormal Rectangular Polynomials," Appl. Opt. 55, 2873-2880 (2016). Doi:10.1364/AO.55.002873

http://dx.doi.org/10.1364/AO.55.002873

High performance DOPC setups require meticulous alignment to precisely read the wavefront of the coherent light scattered by a turbid medium and to play back the conjugated beam toward the target region. Misalignments and imperfections of the optical components immensely reduce the capability of a DOPC setup. This section introduces a systematic calibration process based on orthonormal rectangular polynomials [105] to determine the potential optical misalignments and imperfections in the system and eliminate such effects through a mechanical fine tunning process at the first step [102].

Because of the finite resolution of the alignment tools used in the system, there will be some limitations in the mechanical fine tuning process. At the second step and after achieving the best possible alignment through the mechanical fine tuning procedure, the remaining imperfections are compensated through an iterative software based algorithm which helps to improve the performance of a typical DOPC setup. The improvement was quantitatively assessed by measuring the system's peak to background ratio (PBR) when focusing light through a scattering medium.

Impact of optical aberrations on the DOPC performance

Besides precise alignment between the SLM and sCMOS camera, performance of the DOPC is highly dependent on the quality of the laser's wavefront since any aberration that deviates the beam from a plane wave causes systematic distortion in the wavefront recording as well

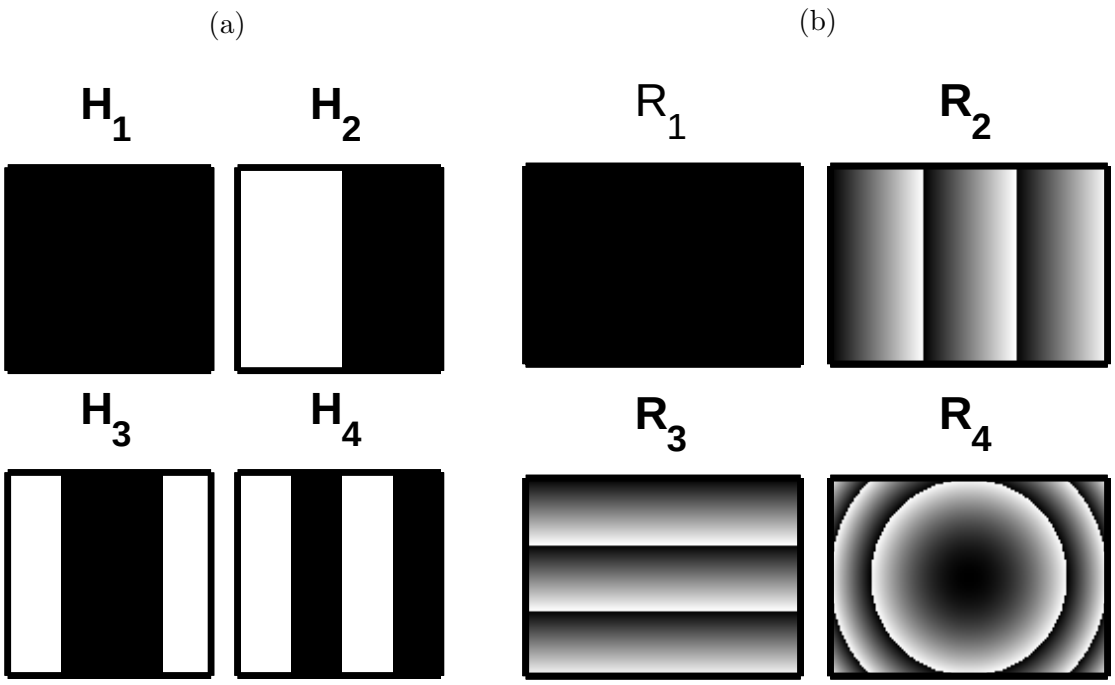

Figure 4.12: Two types of orthogonal patterns were used during the optimization procedure, (A) Hadamard basis and (B) orthonormal rectangular polynomials.

as the phase conjugation process. Other factors that impact the performance of the setup are the substrate curvature of the SLM that originates from imperfections in its fabrication process such as the limited precision in polishing the silicon backplane used in LCoS-SLM (Liquid Crystal on Silicon SLM) technology and also the nonuniformity of the SLM cover glass [107, 108, 109]. Deformation of the spatial light modulators is mainly spherical and its peak to valley distortion is about 3 to 4 wavelengths at $633nm$ (HOLOEYE Systems Inc., Germany). The overall wavefront distortion in a DOPC setup is mostly caused by the superposition of the SLM curvature and the reference beam abberation. Detection and correction of such imperfections should be achieved at subwavelength scale which is a tedious process and in some cases infeasible because of the finite spatial resolution offered by most alignment devices or the inherent aberrations of the optical components. Consequently, a more practical solution is using the SLM itself and developing software calibration algorithms to automatically compensate the effect of imperfections and aberrations in the system. To see how aberrations in the reference beam can affect the optical phase conjugation process,

suppose that the reference and sample beams on the detector plane are represented by the complex amplitudes: $U_R(x,y) = A_R exp[i\phi_R(x,y)]$ and $U_S(x,y) = A_S exp[i\phi_S(x,y)]$, where (x,y) is the coordinates of SLM pixels. The intensity of the interference pattern on the detector for this case is:

$$I(x,y) = |U_R + U_S|^2 = A_R^2 + A_S^2 + 2A_R A_S cos[\phi_R(x,y) - \Phi_S(x,y)]. \tag{4.6}$$

Using this equation, the phase information can be calculated by the phase shifting holography technique [95]:

$$\phi_S(x,y) - \phi_R(x,y) = tan^{-1}\left(\frac{I_{3\pi/2}(x,y) - I_{\pi/2}(x,y)}{I_0(x,y) - I_\pi(x,y)}\right), \tag{4.7}$$

where $I_0, I_{\pi/2}, I_\pi$ and $I_{3\pi/2}$ are the intensities of the interference patterns recorded by the camera when the phase of the reference beam is shifted by $0, \pi/2, \pi$ and $3\pi/2$ respectively. In the next step, the conjugate of the extracted phase map is loaded on the SLM. If the reference beam with the phase $\phi_R(x,y)$ hits the SLM, the phase of the modulated beam will be $[2\phi_R(x,y) - \phi_S(x,y)]$, which corresponds to a systematic error equal to $-2\phi_R(x,y)$. As it is shown, the reference beam aberrations appear by a factor of two in the system and the reason is that the reference beam serves in both wave front measurement step and also phase modulation procedure. For example, if the reference beam has a defocus aberration with the peak-to-valley of one wave, the conjugated sample beam will have added defocus aberration error with the peak-to-valley of two waves. To completely compensate this aberration, the calibration algorithm should add a phase map of $-2\phi_R(x,y)$ to the sample phase information. The same analysis can be extended to the SLM's aberrations as well. Assume that the reference beam is an ideal plane wave and the aberrations introduced by the SLM's surface is modeled by $\phi_{SLM}(x,y)$. In this case, the modulated beam will have a phase profile of $[\phi_{SLM}(x,y) - \phi_S(x,y)]$. Compared to the reference beam aberrations, imperfections introduced by the SLM curvature have a less impact to the performance of the system.

Hadamard patterns (Figure 4.12(A)) have been employed previously to improve the performance of a DOPC system [82]. In this algorithm, an iterative calibration procedure was employed to use Hadamard basis and compensate for backplane curvature of the SLM and reference beam optical aberrations. During the iteration process, the reflected light was coupled back to the same single-mode fiber that the reference light was emitting from. By adding a beam splitter and photodiode into the reference beam path, the intensity of the back coupled beam was monitored. This intensity would be maximized if the compensation phase pattern guarantees the wavefront flatness between the reference beam and SLM.

Zernike circle polynomials [106] are widely employed to model aberrations in optical systems, such as defocus, tilt, and astigmatism. These polynomials are originally defined over circular pupils; therefore, applying them to a rectangular area, such as a SLM, might not compensate the optical aberrations at the corners. Even if the radius of the patterns are chosen in such a way that it can cover the whole area of the SLM, the orthogonality of these polynomials over noncircular pupils is lost. In this paper, we introduce a calibration process based on orthogonal rectangular polynomials [105]. By compensating considerable portion of imperfections, this algorithm improves the performance of the system. The orthogonal rectangular polynomials (Figure 4.12(B)) are based on the Zernike circle polynomials and the details can be found in [105]. The proposed calibration process is done without adding extra complexity or optical components to the existing system and the improvement is directly observed via tracking changes in the PBR as a standard measure in quantifying the performance of DOPC setups. The proposed method uses high spatial resolution rectangular patterns to find the optimal compensation phase profile through a relatively small number of iterations. If the Hadamard basis is used, achieving a similar resolution and accuracy in describing distortions in the system becomes challenging and usually many more number of iterations are needed. As will be discussed in the next section, the proposed algorithm based on the rectangular patterns was about an order of magnitude faster than the similar calibration procedure based on Hadamard basis. The proposed algorithm based on the

rectangular polynomials can also provide more insight regarding the possible misalignments and imperfections in the system and help eliminating them through a mechanical fine tuning procedure. This would help to develop a systematic procedure for the calibration process which is discussed in section 4.3.

4.4.1 Rectangle Polynomial-Based Calibration Algorithm

General Calibration Procedure

The pseudocode description of the implemented calibration process is shown in table 4.1. In this algorithm, the first ten rectangular polynomials ($M = 10$) were chosen. For each polynomial, 1080×1920 pixels phase profiles with $N = 20$ different peak-to-valley phase differences were generated (ϕ_{MN}). In the rest of the paper we use amplitude to refer to the peak-to-valley phase differences where an amplitude of 1 corresponds to a peak-to-valley phase difference of 2π. Amplitudes were in the range of -2 to 2 with the step size of 0.2, unless specified. The range and step size can be assigned according to the required calibration accuracy and speed.

After extracting the phase information of a scattering sample (ϕ_S) and recording the initial peak intensity of the phase conjugated beam (I) using the CCD camera, the calibration procedure was performed. The algorithm starts with the first aberration type and among the N patterns, it selects the one that produces the largest intensity on the CCD camera when added to ϕ_S. The same procedure repeated sequentially for other types of aberration ($M = 1, ..., 10$). After compensating the first aberration type, the calibration algorithm proceeds with the next aberration types. To reduce effects of camera noise and intensity fluctuations, each measurement was repeated several times ($MaximumTrial = 5$) and the corresponding CCD images were averaged. Further discussions on the intensity fluctuations are presented later in this section.

To test the proposed algorithm, a scattering sample was made by stacking five layers of

Table 4.1: Calibration algorithm based on the rectangular polynomials

ϕ_S : Extracted phase profile of the scattering sample,
ϕ_{SLM} : Phase profile displayed on the SLM,
ϕ_{Comp} : Optimal compensation phase profile,
I : Intensity of the detected phase conjugated beam on the CCD,
1. Select $'M'$ different aberration types (tilt, defocus, coma,),
2. For each aberration type, generate $'N'$ phase profiles with different amplitudes (ϕ_{MN}),
3. Execute the phase conjugation procedure and measure $'I'$ and assign $I_{max} = I$,
4. Start calibration procedure:
 for i=1:M
  for j=1:$MaximumTrial$
   for k=1:N
   $\phi_{SLM} = \phi_S + \phi_{Comp} + \phi_{MN}$;
   Intensity(k,j)= I;
   end
  end
  Intensity(1:N,1)= Mean value of matrix $'Intensity'$;
  L=Find index of [max(Intensity)];
   if ($Intensity(L, 1) > I_{max}$)
    $I_{max} = Intensity(L, 1)$;
    $\phi_{Comp} = \phi_{Comp} + \phi_{ML}$;
  end
 end
5. $\phi_{SLM} = \phi_S + \phi_{Comp}$;

a scattering material (Scotch Magic Tape, 810, 3M Inc.) on a microscope cover glass and placed in the sample path (Figure 4.5). Ballistic beam transmittance (M_u), the amount of light that passes through a sample without being scattered or absorbed, was measured to quantify the $\mu_s l$ parameter of our sample [42]:

$$M_\mu = exp(-\mu_s l), \tag{4.8}$$

where μ_s and l are the scattering coefficient and thickness of the sample, respectively. To measure M_μ, first, a collimated laser beam of diameter $\sim 1.3mm$ was aimed toward the sample while an aperture of the same diameter was precisely aligned with the laser beam and placed before a detector (S130C-PM100D, Thorlabs, NJ, USA) to reject the scattered

light at $2m$ distance from the sample. The background measurement was made by replacing the sample with a microscope cover glass to take into account effects such as the refraction or reflection caused by the glass. According to the method described in [42], the $\mu_s l$ for our sample was ~ 10.8.

After the phase conjugation step for this sample, the calibration process was performed. A factor of 8.5 increase in the PBR was observed after the calibration step in this test. Figure 4.13, shows the improvement in the PBR as the iterations proceeds. The PBR value at each iteration is normalized to the initial PBR value which was measured immediately before starting the calibration procedure. The calibration process with 200 rectangular patterns took less than two minutes (64 bit operating system, Windows 7 home premium, 8GB RAM, Intel core(TM)i3 CPU@3.3 GHz).

For comparison, a similar algorithm was developed based on the Hadamard basis. For this experiment, 16×16 Hadamard basis was used ($M = 256$) where the whole area of the SLM (1080×1920 pixels) was divided to super pixels each consisting of 67×120 pixels. For each Hadamard base, phases of the SLM pixels corresponding to the positive entries of the Hadamard basis were changed from 0 to 2π in discrete steps of $\pi/8$ ($N = 8$). The calibration algorithm was similar to the one shown in table 4.1 except that Hadamard bases were used instead of rectangular polynomials. As it is shown in Figure 4.13 (A), the Hadamard basis increased the PBR by a factor of ~ 3. The smaller increase in the PBR with Hadamard basis, in comparison with the rectangular polynomials, can be due to the fact that optical aberrations are sparsely represented by rectangle (Zernike) polynomials. In contrast, modeling each of these aberrations with Hadamard basis requires a large number of patterns. This makes the iteration process more time consuming than the proposed algorithm and in practice, inefficient to compensate major aberrations with a limited number of calibration patterns.

Increasing the scattering coefficient or thickness of a sample can significantly decrease the efficiency of the phase conjugation process in the presence of optical imperfections in the

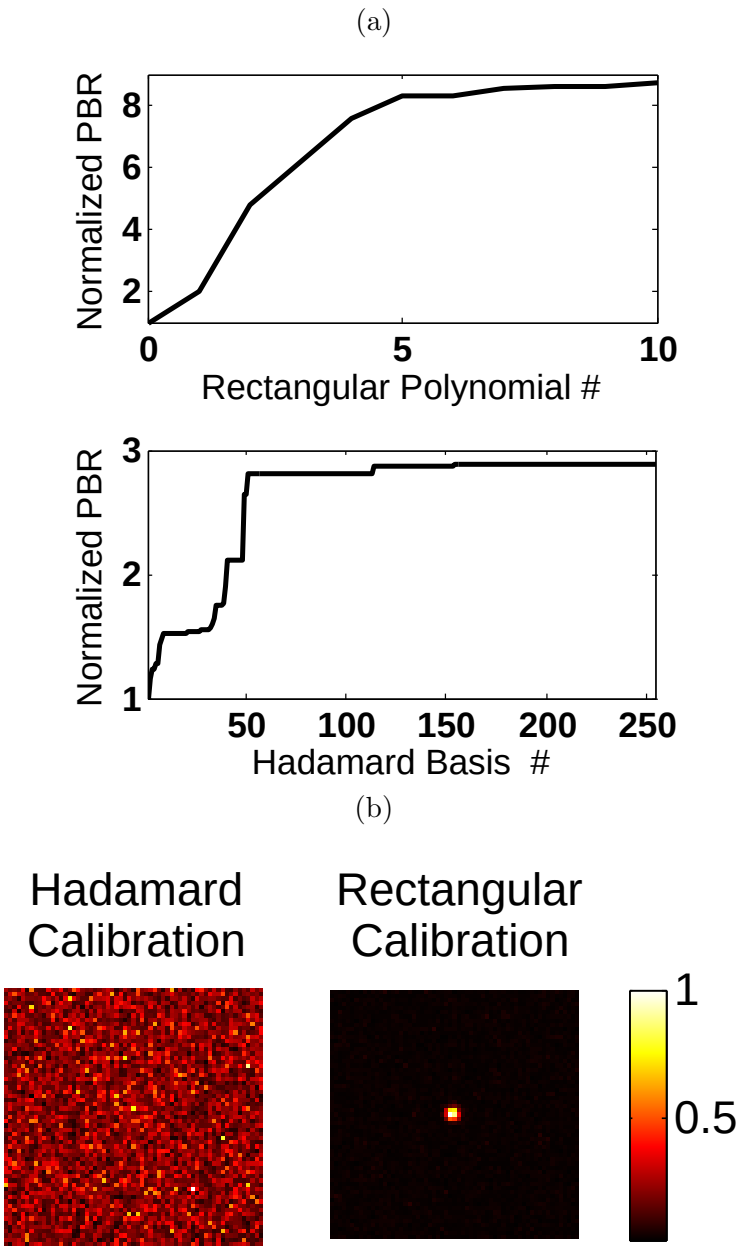

Figure 4.13: A comparison between the performance of the calibration process using rectangle polynomials and Hadamard basis for two different samples, (A) five layers of Scotch tape, (B) three ground glass diffusers at the distance of $8mm$ from each other.

system. For such samples, the performance of the system becomes much more sensitive to the misalignments and aberrations and the proper calibration of the system has considerable impact on the final PBR. To evaluate the performance of the proposed calibration algorithm in such conditions, a more challenging sample, consisting of three ground glass diffusers

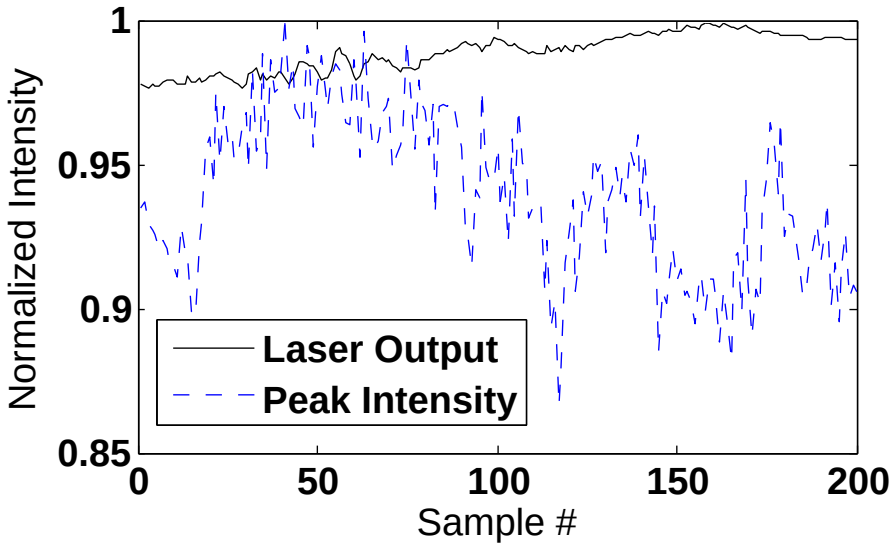

Figure 4.14: Fluctuations of the laser's output power and the peak intensity monitored by a CCD camera after phase conjugation process.

(DG10-600-MD, Thorlabs, NJ, USA) at the distance of $8mm$ from each other. Then, optical aberrations such as defocus and tilt were introduced to the system so that no focal point was observed on the camera after phase conjugation. Next, the calibration algorithms based on the rectangular polynomials and Hadamard basis were employed. As it is shown in Figure 4.13 (B), the proposed algorithm based on the rectangular polynomials was able to recover the focal point.

In the proposed iterative algorithm, the criterion for selecting a compensation phase profile was based on the increase in the intensity detected by the CCD camera. However, fluctuations in the intensity of the laser source or mechanical vibrations in the system can also induce changes on the measured PBR. Figure 4.14 shows the fluctuation of the peak intensity of the conjugated beam monitored by the camera as well as the laser power instability over 20 seconds (sampling rate of $10Hz$). The instability in the laser output intensity is less than 2.5% and can be ignored. However, mechanical vibration in the system produces significant intensity fluctuations. Due to such fluctuations, the calibration process might produce different compensation phase profiles and different level of PBR improvements for each trial. As an example, for a sample consisting of two ground glass diffusers placed at

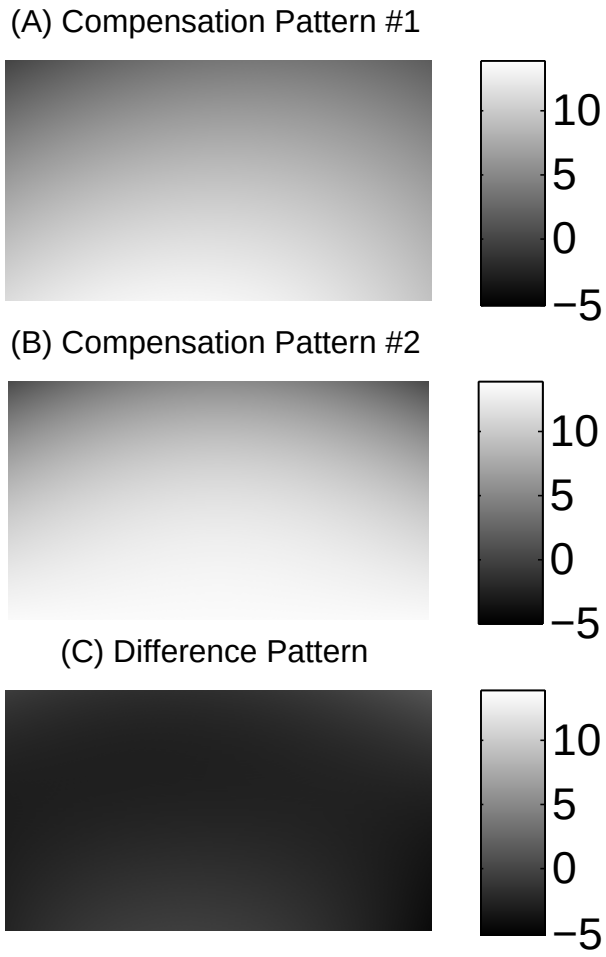

Figure 4.15: Compensation phase profiles obtained for two different sample types (A) two and (B) three ground glass diffusers at $8mm$ separation distances, (C) difference between patterns shown in panels (A) and (B), all units are in radians.

$8mm$ distance, the calibration process was repeated 10 times and the improvement factor varied from 2.93 to 3.23. A practical approach to alleviate the impact of fluctuations on the proposed algorithm was to perform multiple recordings for each calibration phase pattern (ϕ_{MN}) at different time points and average them. Experimental results showed that averaging can also improve the consistency of the compensation phase profiles obtained for different trials.

Since the proposed iterative calibration procedure was employed while a sample was presented in the system, a potential question would be whether the extracted compensation phase profile is sample dependent or not? Here, we designed a two-step experiment to

confirm that the calibration process is independent of the sample. First, two ground glass diffusers (DG10-600-MD, Thorlabs, NJ, USA) separated by $8mm$ distance were used as a scattering sample and the calibration process was performed to extract and record the optimum compensation phase profile to be used later. In the next step, the sample was replaced by three ground glass diffusers at the distance of $8mm$ from each other. After completing the calibration process, the maximum light intensity on the CCD camera was recorded (I_1). Without moving the sample, the compensation phase profile extracted in the first experiment (sample #1) was used for the second sample and again the maximum light intensity on the CCD camera was recorded (I_2). For this experiment, on average, $I_2 \simeq 0.94 \times I_1$, which confirms that the compensation phase profile does not depend on the sample type. We also directly compared the obtained compensation phase profiles for these two different samples. Figure 4.15 (A) and (B) show the unwrapped compensation phase profiles achieved for sample #1 and #2, respectively. The root-mean-square (RMS) error corresponding to the difference between the phase profiles (panel (C) in the same figure) was about 0.07λ. The RMS error varies slightly between different trials. For instance, for these two sample types, the calibration algorithm was repeated 5 times and the average RMS error value was 0.15λ. This error value is almost twice the diffraction limited aberration level (0.0745λ). Our experiments also showed that this relatively small error does not have a considerable impact on the system's performance. Based on these two validation procedures, we can conclude that the compensation phase profile is independent of the sample type and it just depends on the misalignment and optical aberrations in the system. Therefore, compensation phase profile can be obtained once and as long as no change is applied to the setup, the same phase profile can be employed in future experiments.

Quantification and Compensation of the Reference Beam Aberrations

To see how the reference beam aberrations degrades the PBR and to quantify the performance of the proposed calibration procedure, a sequence of simulations and experiments were performed. In two different experiments, two types of aberrations, including defocus and tilt were introduced to the reference beam separately and in each experiment, the PBR was recorded before and after introducing the aberration. The defocus aberration was introduced by shifting the collimating lens along the optical axis from the ideal position. In the reference arm, an achromatic doublet lens with the focal length of $150mm$ (Edmundoptics, 50mm Dia. x 150mm FL, NJ, USA) was placed in front of a single mode optical fiber. Zemax simulations (Zemax LLC, WA, USA) show that $2mm$ offset in the position of the lens toward the optical fiber causes defocus aberration with the peak-to-valley of 3.05 waves (at $532nm$) on the surface of the SLM with the length of $12.5mm$, placed at the distance of $150mm$ from the collimating lens. Simulation results are shown in Figure 4.16(A). Then, the same offset was introduced experimentally to the DOPC system and for a sample consisting of five layers of Scotch tape, the PBR dropped to 1/5 of its initial value before introducing the aberration. After employing the calibration procedure, the PBR reached to 95% of the initial value. The unwrapped phase profile of the estimated aberration in the system after applying the calibration algorithm is shown in Figure 4.16(A).

For the second experiment, a 0.04 degree horizontal tilt was introduced in the reference beam. For this case, Zemax simulation shows an aberration with the peak-to-valley of 16.4 waves (Figure 4.16(B)). For the same sample, tilt aberration reduced the PBR by a factor of 9, but the calibration procedure was able to improve the PBR up to 93% of the initial PBR. The unwrapped phase profile of the estimated aberration in the system after applying the calibration algorithm is shown in Figure 4.16(B). As the experimental results show, the calibration algorithm was able to compensate the main part of the reference beam aberrations and improved the PBR.

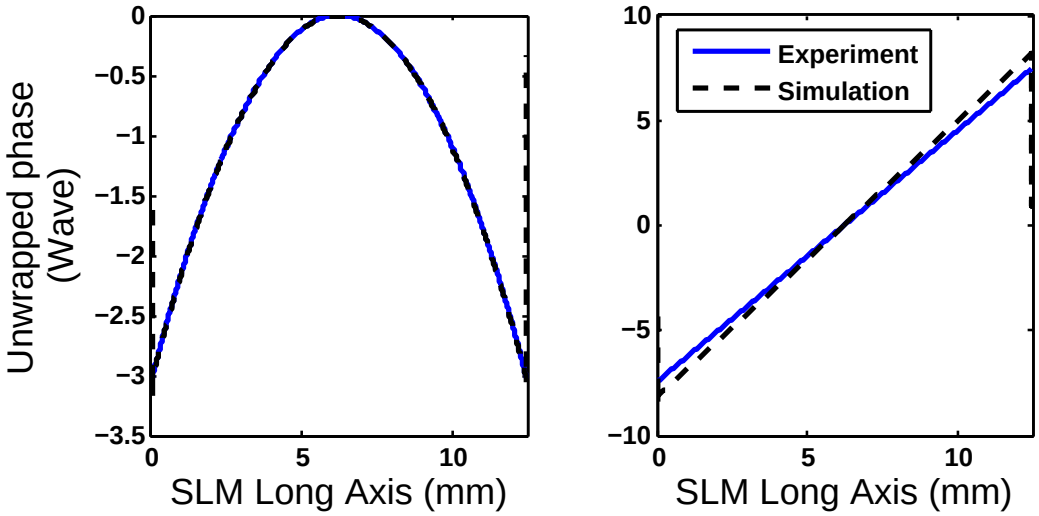

Figure 4.16: Systematic optical misalignments were introduced to the DOPC system and optical aberrations were simulated using Zemax software. Capability of the calibration algorithm to estimate aberrations in the system was evaluated experimentally. (A) The defocus aberration was introduced by applying $2mm$ offset in the position of the collimating lens in the reference path and (B) a 0.04 degree horizontal tilt was introduced in the reference beam. Results show that the calibration algorithm can determine and compensate the introduced optical aberrations with high precision.

Systematic Alignment of the DOPC System

In the previous section, we showed how the proposed calibration algorithm quantifies possible misalignments and aberrations in the system. In this section, we show how this information can be used to design a two step systematic calibration procedure after initial alignment of DOPC setups. The first step includes estimation of different aberrations in the system (such as tilt and defocus) and then alleviating them through a mechanical fine tuning procedure. Part of these imperfections may remain in the system due to the limitations of alignment tools. At the second step, the software-based calibration algorithm compensates the remaining imperfections.

Figure 4.17 shows the improvements achieved by following the mechanical fine tuning procedure for the Scotch tape sample. Due to imperfections in the initial alignment of the setup, the reconstructed spot was deteriorated (Figure 4.17 (A)). By employing the calibration algorithm, the level of aberrations in the system was estimated. At this step, calibration

phase patterns were generated over a wide range of amplitudes (-10 to 10 at the step size of 0.5) to asses severe aberrations. As an example, Figure 4.17 (B) shows the defocus calibration pattern extracted by the algorithm. According to Zemax simulation, such a defocus aberration can be corrected by mechanically decreasing the distance between the optical fiber and collimating lens by $\sim 2mm$. We used a Z-axis translation mount (SM1Z, Thorlabs, NJ, USA) to adjust the distance according to the simulation results. To demonstrate the effect of this fine tunning, the phase conjugation step was repeated to reconstruct the spot (Figure 4.17 (C)). The comparison between the results achieved before and after compensating this defocus aberration shows a PBR improvement by a factor of ~ 20. Figure 4.17 (D) shows the remaining defocus aberration after mechanical fine tuning. Similar mechanical fine tining procedures were applied to reduce other aberrations in the system such as horizontal and vertical tilt.

At the second step, since there were mechanical displacements in the setup, it was necessary to obtain a new sample phase profile (Figure 4.18 (A)). Then, the remaining imperfections in the system were compensated using the software based calibration algorithm. To increase the accuracy of the calibration algorithm, the step size of the applied patterns was reduced to 0.1 and the amplitude range was set between -2 and 2. The compensation phase profile obtained in this step were recorded for future use. For this sample, when the compensation phase pattern was added to the sample phase profile, the result showed 4.5 fold increase in the PBR and the reconstructed spot is shown Figure 4.18 (C). Panel (B) in the same figure represents the image recorded by the CCD camera when a random phase pattern was loaded on the SLM. The theoretical value of the PBR can be calculated by $\pi P/4S$, where P and S are the number of active pixels and the autocorrelation area of the speckle pattern on the SLM, respectively [82] . The mean speckle size was estimated by calculating 1D autocorrelation of the speckle patterns along the x- and y-axis. The measured speckle size was $\sim 2.8 \times 3$ SLM pixels ($17.9\mu m \times 19.2\mu m$). For the results shown in Figure 4.18, the measured PBR is $\sim 121,000$. The horizontal and vertical FWHM of the focused beam

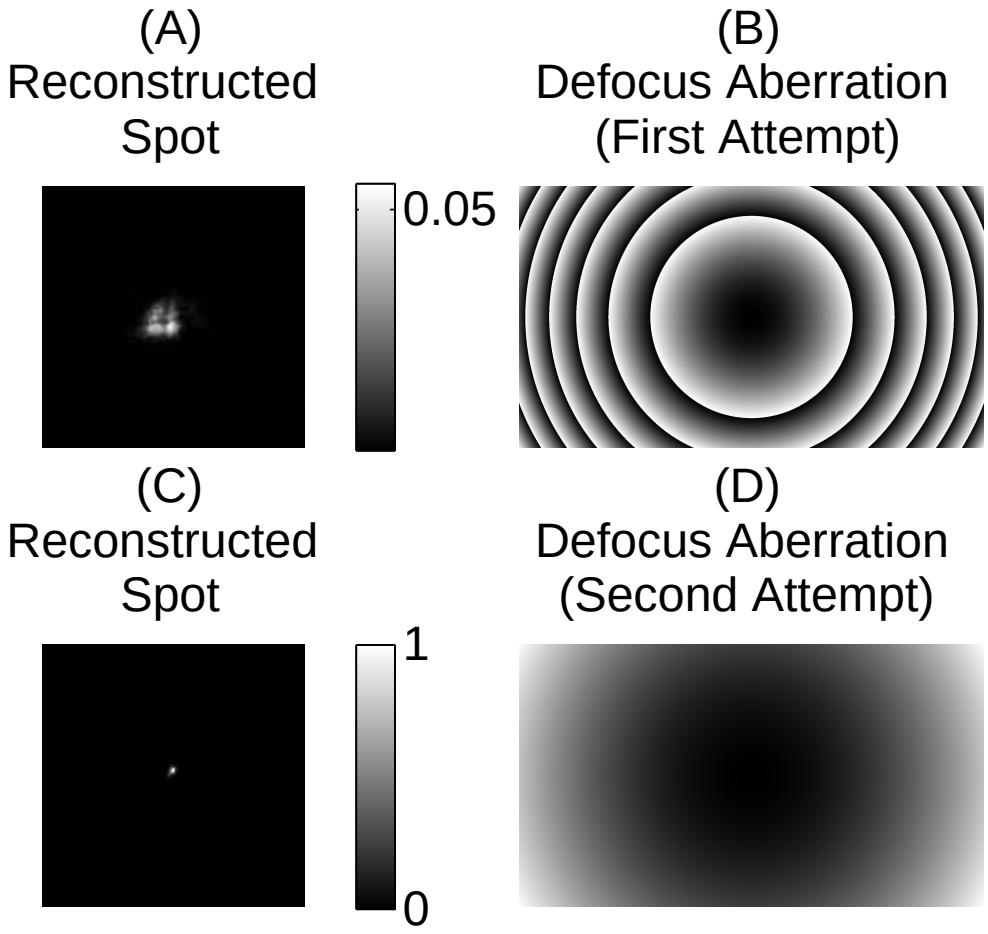

Figure 4.17: Top panel shows the reconstructed spot right after rough alignment of the system and the compensation phase profile extracted by the algorithm. Bottom panel shows the reduction in defocus aberration and improvement of the reconstructed spot after the second mechanical fine tuning attempt.

were estimated by fitting a 2D Gaussian function to the data and were $12\mu m$ and $16.7\mu m$, respectively. Under the assumption of perfect Gaussian beam propagation, the FWHM at the focal would be $9.49\mu m$.

Conclusion and discussion

In 2010, digital optical phase conjugation (DOPC) based on liquid crystal spatial light modulators was developed [81]. This method has two main advantages over the nonlinear optics based optical phase conjugate approach: the efficiency of the phase conjugation is indepen-

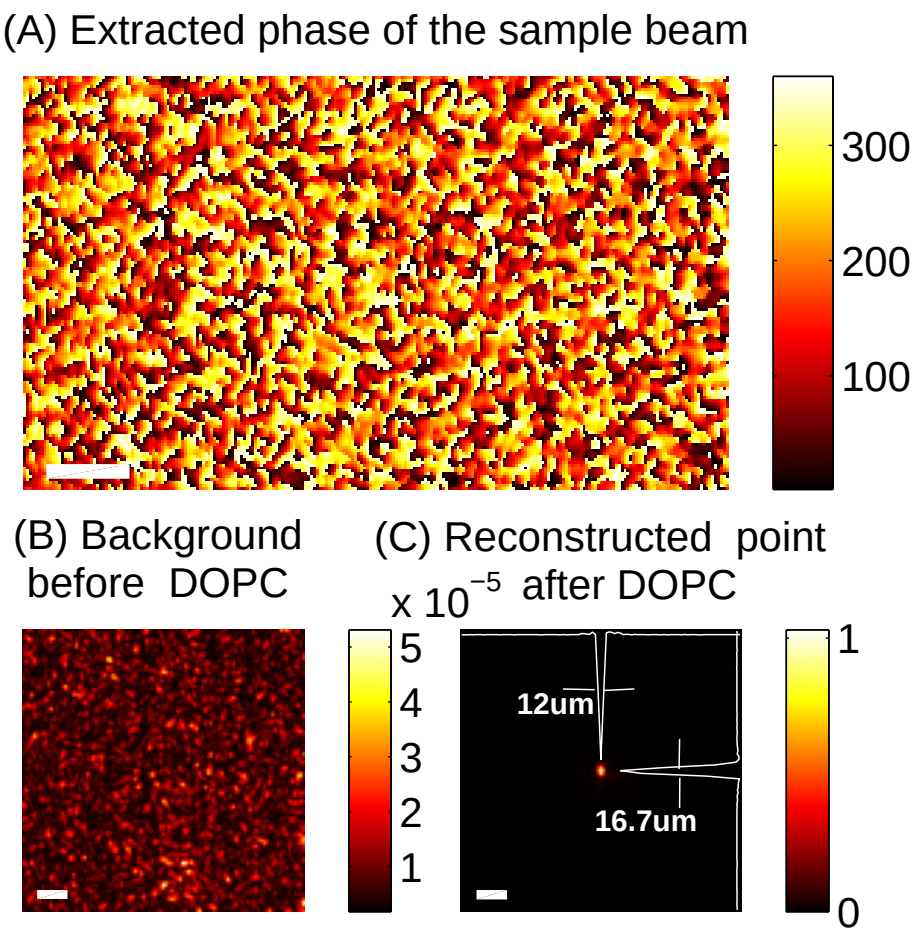

Figure 4.18: (A) Phase profile of the light passed through the scattering medium (five layers of Scotch tape) extracted by the four step digital holography method. Image captured by the CCD camera (B) when a random phase pattern was loaded on the SLM and (C) after optical phase conjugation followed by the calibration process. Scale bars are, (A) 200μm, (B) and (C) 50μm.

dent of the input signal and the power of the conjugated beam can be adjusted based on the specific applications; and the setup is operational with different light sources like CW or pulsed laser. In this chapter, details of the implemented DOPC system was described and the performance of the system in focusing light through and inside scattering mediums were quantified.

In this chapter, we also showed how misalignments and imperfections of the optical components can immensely reduce the capability of a DOPC setup. Then, a systematic calibration algorithm was proposed and experimentally applied to a digital optical phase

conjugation (DOPC) system to compensate main aberrations in the setup such as aberrations of the reference beam and also backplane curvature of the spatial light modulator (SLM). At the first step of the calibration procedure, different aberrations in the system were estimated which provide guidance to alleviate major part of them through a mechanical fine tuning procedure. Then, the software-based calibration algorithm compensates the remaining imperfections in the system. Simulation results using Zemax software showed that some imperfections in the alignment of the system which might be ignored in most optical systems can cause considerable error in a DOPC setup. For example, tilt misalignment of the reference beam from the ideal perpendicular position with respect to the surface of the SLM, in the range of 0.04 degree, can cause up to 16 waves error in the optical phase conjugation procedure (at $532nm$). Also, as an example of the reference beam aberrations, simulation results indicated that $2mm$ offset in the position of the collimating lens with the focal length of $150mm$ can cause a defocus aberration with the peak-to-valley of about 3.05 waves in the reference beam. On the other hand, a typical SLM does not have a perfect flat surface and its deviation could be up to 4 waves (at $633nm$, HOLOEYE Systems Inc.). Our experimental results confirmed that such errors were enough to degrade the performance of the DOPC system significantly for highly scattering samples. Therefore, fine tuning and calibration of the DOPC system seems to be an essential step. The proposed iterative calibration algorithm based on rectangular polynomials helps to find an optimum compensation phase profile and once added to the phase information of the sample beam, increased the peak-to-background ratio. In a highly scattering sample, the calibration algorithm achieved up to 8 fold increase in the PBR. This algorithm did not require any extra optical component; furthermore, the feedback signal during the iterative calibration process was based on the PBR which is a standard measure to quantify the performance of the optical phase conjugation procedure.

The advantage of rectangular polynomials over other orthogonal patterns such as Hadamard basis, which previously was employed to calibrate a DOPC system [82], is the fact that it matches the common optical aberrations, such as defocus, tilt, coma and astigmatism. A

reasonable number of terms in rectangular polynomials can model most optical aberrations. Therefore, the proposed algorithm searches only among a limited number of high resolution rectangular calibration patterns that match the aberrations in the system. Generating high resolution Hadamard basis and randomly searching among the set could be a time consuming procedure. Moreover the proposed calibration algorithm estimates misalignments and aberrations in the system. This information assisted to improve the alignment of the DOPC setup through a systematic mechanical fine tuning process.

Chapter 5

Conclusions and Future Works

In this project, three different optical systems were designed and implemented for optogenetic experiments: an electro-optical scanning system to extract optical properties of the brain tissue with high spatial resolution; a fluorescent tomography system for the reconstruction of fluorescent distributions in rodents brain; and a digital optical phase conjugation (DOPC) system which can potentially be employed for fluorescent imaging and deep brain optogenetic stimulation. In the following section, the concluding remarks and potential future directions for these projects are given.

Extraction of optical properties and prediction of light distribution in rat's brain tissue

In chapter 2, the design and implementation of an electro-optical scanner used to extract optical properties of the brain tissue with high spatial resolution were explained. In this system, diffuse reflectance and diffuse transmittance variables were measured simultaneously using the double integrating system shown in Fig. 2.2 (setup 1) and the ballistic transmittance measurements were performed by the optical setup 2 in the same Figure. Since two separate setups were employed to collect this information, it was required to implement a registration algorithm to match these two sets of measurements for the subsequent reconstruction step. Since the accuracy of the registration algorithm is limited, design and development of a single setup to acquire all data points in one round of experiments is highly preferred. This can be accomplished by applying some modifications to the existing setup (setup (1) in Fig. 2.2) where the bottom integrating sphere is replaced by a new sphere which has a third

port on the opposite side of the entrance port to measure the ballistic beam that exits the integrating sphere [41]. Such a configuration eliminates the physical movement of the sample during measurements and improves the precision of the reconstructed optical properties.

In the next step, the database of the extracted optical properties was linked to a three-dimensional (3D) Monte Carlo toolbox [49] to simulate light-tissue interactions and estimate the light distribution inside tissue. In the current version of the Monte Carlo software, the refractive index is assumed to be identical for all voxels, i.e., mismatched voxel boundaries (such as air-tissue mismatched boundary) have not been considered in the current implementation [49]. The accuracy of the simulation results can be improved by addressing this assumption which might cause some errors in final results.

Previous experiments have shown that mammalian blood has relatively high absorption and scattering coefficients and incorporating the optical properties of the blood in tissue models can improve the precision of the predictions. In section 2.5, a costume-made optical coherence tomography system (OCT) was employed to scan the cortical tissue of a rat and generate a 3D angiogram of blood vessels. Then, the extracted network of blood vessels was integrated into the extracted optical properties of the brain tissue to develop a more realistic model of the sample. In this case, the issue with employing the OCT system is that the imaging depth is limited to few hundred microns. In addition, superficial blood vessels can cause optical shadowing that obscures the underlying network of blood vessels. To practically overcome these shortcomings, other imaging modalities such as computed tomography angiography (CTA) or magnetic resonance angiography (MRA) can be employed to extract the network of blood vessels. It should be mentioned that even though these imaging modalities have considerable imaging depth, but their resolution is less than OCT systems.

Another important aspect during optogenetic experiments is the heat generation as a result of optical irradiation of the brain tissue. Brian tissue and network of blood vessels have considerable absorption coefficients particularly in the visible spectrum where the main optogenetic proteins have maximum sensitivity. The light induced temperature increase in

the brain tissue can cause permanent damage or induce abnormal neural activity. Currently, one ongoing project in the lab is to develop a simulation platform to predict heat distribution followed by optical stimulation. In this project, first, the light distribution is simulated using our 3D Monte Carlo software for different light source configurations. Then, the Pennes bioheat equation [110] is numerically solved to estimate the thermal response of the tissue.

Design and implementation of a fluorescent tomography system for brain studies

The design and implementation of a fluorescent tomography scanner for brain studies was discussed in chapter 3. Fluorescent proteins are used as bio-markers to confirm the expression of light-sensitive proteins, such as ChR2 or NpHR, after viral transfection. If these fluorescent proteins are illuminated with appropriate wavelengths of light, they emit fluorescent signal which indirectly confirms the expression of the light sensitive opsins. Our aim in this part of the project was to develop a fluorescent optical tomography system, both hardware and software, to be used for *in-vivo* optogenetic experiments and to confirm the expression of light sensitive opsins in rodent's brain.

The *in-vivo* experiments were conducted on thinned-skull rats which received viral transfection to express green flourescent protein (GFP) in their cortex. Based on its excitation spectrum, shown in Fig. 3.14, GFP has maximum sensitivity around 490nm. In our system, blue laser at 445nm was employed for the excitation where GFP still has considerable sensitivity. Our experimental results in chapter 2 show that the brain tissue has high absorption coefficient in this range of wavelengths which limits the penetration depth of the excitation light. One potential solution to increase the imaging depth is by using red-shifted fluorescent proteins, such as tdTomato and mCherry [111, 112]. As an example, the excitation/emission spectrum of mCherry protein is shown in Fig. 5.1 where the excitation peak is around 590nm. Based on the generic model of the brain tissue [59], the absorption coefficient for the yellow light at 590nm is about 3 times less than the blue laser at 445nm which was

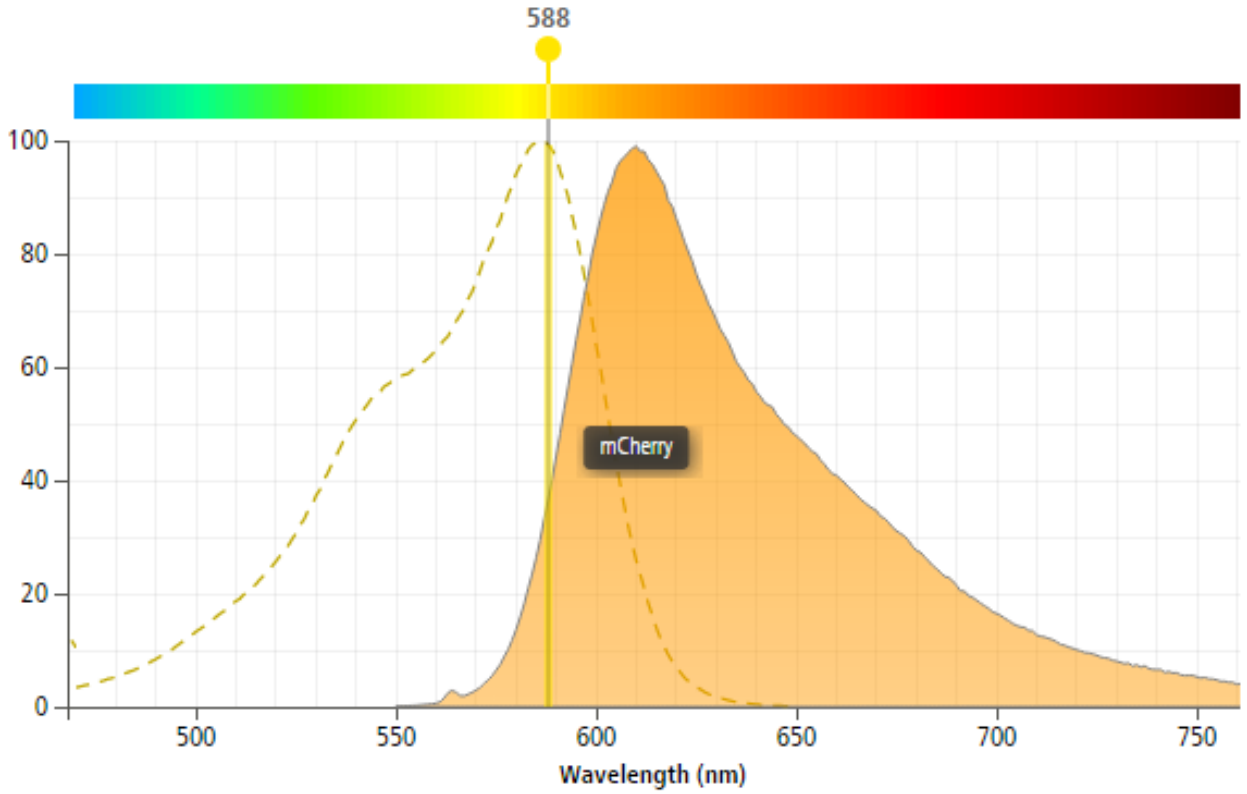

Figure 5.1: Excitation/emission spectrum of mCherry, adapted with some modifications from [78].

used in our experiments. Therefore, by switching to red-shifted proteins, the imaging depth can be improved. Nevertheless, it should be mentioned that based on the application and specifications of an experiment, and some critical factors, such as brightness (determined by factors including the extinction coefficient and quantum yield) or photostability needs to be considered before choosing a specific fluorescent protein. As a comparison, GFP has a brightness factor of 690 whereas for mCherry, this factor is 96 [111]. At the time, this factor was one of the reasons we chose GFP for our experiments.

A challenge in *in-vivo* fluorescent imaging is the tissue background fluorescence (autofluorescence) due to existence of substances such as flavins and porphyrins [114]. Several techniques are proposed to reduce the amount of autofluorescent signal emitted from tissue samples in fluorescent microscopy [114, 115], but only few groups ultimately dealt with *in-vivo* autofluorescent cancellation [116]. The technique proposed in [115, 116] is based on the

fact that most autofluorescence substances have broadband excitation spectrum in contrast with fluorescence proteins in which usually the spectrum is narrower. In [115], the target area was first illuminated by a light of wavelength that matches the peak sensitivity of the fluorescent proteins under test. Therefore, the recorded signal consisted both the desired fluorescence signal and the tissue autofluorescence (U_{totl}). The second illumination wavelength was chosen so that the fluorescence protein had negligible sensitivity while the same wavelength still excites autofluorescence molecules (U_{au}). At the final step, the autofluorescence images were scaled by a dimensionless factor, α, and then subtracted pixel-by-pixel from the fluorescence images to yield the autofluorescence-free images (U_{fl}):

$$U_{fl} = U_{totl} - \alpha U_{au}. \tag{5.1}$$

Here the scaling factor α takes a value within the range [0 1].

Designing appropriate readout strategy is another important step during optogenetic experiments. An appealing approach for recording the neural activity during optogenetic stimulation is based on using fluorescent proteins. Fluorescent proteins can convert a physiological signal, such as a specific ion concentration or membrane voltage and pH level changes, to a fluorescent output [12]. Genetically encoded FPs provide a optical mechanisms for specific cell-type fluorescent readouts. Such optical recordings can provide valuable information regarding the spatial distribution of neural activity. One potential application of the developed fluorescent tomography system is extracting 3D maps of the neural activity distribution during optogenetic/electrode-based stimulation of the brain. Fluorescent indicators, such as genetically-encoded protein sensors, can offer relatively fast kinetics. Therefore, tracking the fluorescent signal of theses proteins requires a tomography system with fast scanning, recording and data transferring mechanisms. The existing tomography system needs some modifications to fulfill the speed requirements. The current detector (EMCCD) needs to be replaced by a much faster and sensitive detector such as photo-multiplier.The employed

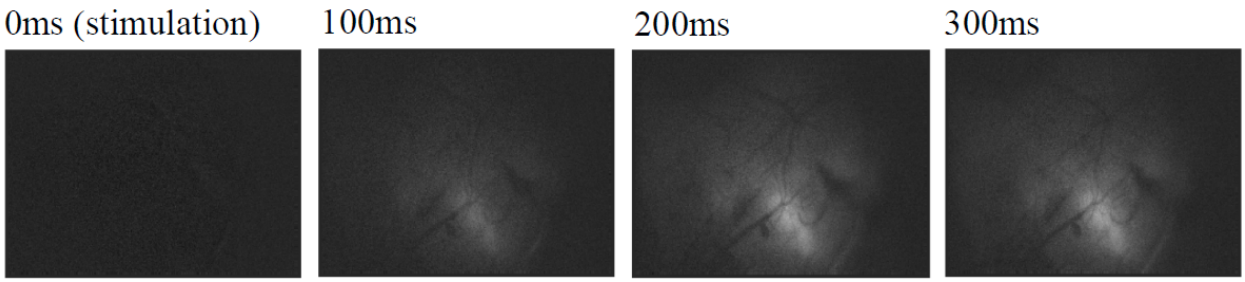

Figure 5.2: Spatial and temporal distribution of fluorescent signal due to injection of $100\mu A$ electrical stimulation through a graphene array with $150\mu m$ site diameter in a transgenic $GCaMP6f$ mouse brain [117].

scanning Galvo system (GVS012) has a maximum speed of 1k A-scan per second, which needs to be replaced by faster models. An example of spacial and temporal distribution of fluorescent signal due to injection of $100\mu A$ electrical stimulation through a graphene array with $150\mu m$ site diameter [117] in the brain of a transgenic $GCaMP6f$ mouse is shown in Fig. 5.2 [117].

Deep tissue light delivery and fluorescent imaging using the optical phase conjugation technique

In chapter 4, details of the implemented digital optical phase conjugation (DOPC) system was discussed and the performance of the system in focusing light *through* and *inside* scattering mediums was quantified. In this chapter, we also showed how misalignments and imperfections of the optical components can immensely reduce the capability of a DOPC setup. Then, a systematic calibration algorithm was proposed and experimentally applied to a digital optical phase conjugation (DOPC) system to compensate main aberrations such as the reference beam aberrations and the backplane curvature of the spatial light modulator (SLM). In a highly scattering sample, the calibration algorithm achieved up to 8 fold increase in the PBR. At the first step of the calibration procedure, different aberrations in the system were estimated to provide some guidance and alleviate the major contributing factors through a mechanical fine tuning procedure. Then, the software-based calibration algorithm

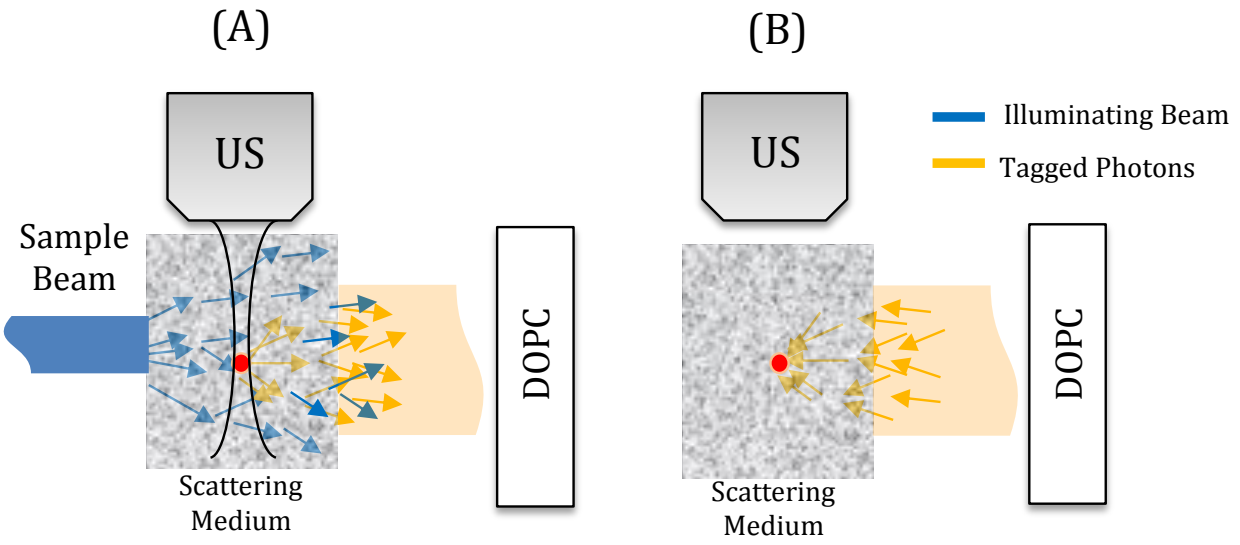

Figure 5.3: Schematic of the digitally time reversed ultrasonically-encoded light for focusing light inside a scattering medium [16], (A) recording step, where phase information of the tagged photons was extracted by using phase shifting holography, (B) playback step, where the phase conjugated beam was sent back to the focal point of the ultrasound transducer.

were applied to compensate the remaining imperfections in the system. In this step, the advantage of rectangular polynomials over other orthogonal patterns, such as Hadamard basis, which was previously employed to calibrate a DOPC system [82], is that these polynomials match well with common optical aberrations such as defocus, tilt, coma, and astigmatism. A reasonable number of terms in the rectangular polynomial expansion can model most optical aberrations. Therefore, the proposed algorithm searches only among a limited number of high resolution rectangular calibration patterns that match the aberrations in the system. Generating high resolution Hadamard basis and randomly searching among the set could be a time consuming procedure. Moreover the proposed calibration algorithm estimates misalignments and aberrations in the system. This information also assisted in improving the alignment of the DOPC setup through a systematic mechanical fine tuning process.

As a part of the effort to focus light *inside* scattering mediums, light perturbation method was discussed in details and experimental phantom results were presented. This approach requires recording a dynamic light filed in two different instances t_1 and t_2, over which the field changes from E_1 to E_2. By subtracting these two fields and time reversing

the resulted field,$[E_1 - E_2]^*$, light can be focused on the position of the moving target. A potential application of these methods is the photoablation of angiogenic vessels in tumors [99] or *in-vivo* cytometry [100]. Nevertheless, for applications such as deep tissue fluorescent imaging or deep brain optogenetic stimulations, no biological phenomenon exists which can be used as a virtual source. In [16], deep tissue fluorescent imaging based on ultrasonically encoded light and DOPC method was proposed. In this method, an ultrasound transducer was used to encode the light passing through the focal point of the ultrasound transducer. After extracting the phase information of the tagged photons , a phase-only SLM was employed to modulate the reference beam and send it back to the focal point of the ultrasound transducer. Schematic of this method is shown in Fig. 5.3. This method has two separate steps: extracting the phase information of the ultrasonically encoded photons and then playing back the phase conjugated version of the sample beam as shown in Figures 5.3(a) and (b), respectively. In the first step, a sequence of high intensity nanosecond laser pulses of frequency f_0 irradiate the scattering sample and due to acousto-optic (AO) phenomenon, a portion of the photons which pass through the focal point of the ultrasound transducer will be frequency shifted $(f_0 + f_U)$. The phase information of the tagged photons are extracted by the phase shifting holography method. Since the tagged photons have frequency of $(f_0 + f_U)$, the reference beam should have equal frequency shift to produce a static interference pattern on the detector. The reference beam can be frequency shifted by using an acousto-optic modulator (AOM). After successfully implementing the DOPC system and achieving a large PBR, currently we are adding other required components into the system, such as ultrasound module and acousto-optic-modulator (AOM).

For the implemented DOPC system, the overall required time for recording and transferring 40 holograms, processing and extracting the phase information, and finally loading the conjugated wavefront on the SLM is in the range of 15 seconds (64 bit operating system, Windows 7 home premium, 8GB RAM, Intel core(TM)i3 CPU@3.3 GHz). For *in-vivo* applications where the tissue decorrelation time is less than few milliseconds, [88], the required

time for the phase conjugation procedure needs to be reduced considerably. The processing time, which is the most time consuming step during OPC procedure, can be reduced significantly by employing a graphic processing unit (GPU) or a field-programmable gate array (FPGA).

Bibliography

[1] Edward S. Boyden, Feng Zhang, Ernst Bamberg, Georg Nagel, and Karl Deisseroth. "Millisecond-timescale, genetically targeted optical control of neural activity." Nature neuroscience 8, no. 9 (2005): 1263-1268.

[2] Yizhar O, Fenno LE, Davidson TJ, Mogri M, Deisseroth K, "Optogenetics in neural systems", Neuron. 2011 Jul 14;71(1):9-34.

[3] Zhang F, Aravanis AM, Adamantidis A, de Lecea L, Deisseroth K., "Circuit-breakers: optical technologies for probing neural signals and systems", Nat Rev Neurosci. 2007 Aug;8(8):577-81.

[4] Georg Nagel, Tanjef Szellas, Wolfram Huhn, Suneel Kateriya, Nona Adeishvili, Peter Berthold, Doris Ollig, Peter Hegemann, and Ernst Bamberg. "Channelrhodopsin-2, a directly light-gated cation-selective membrane channel." Proceedings of the National Academy of Sciences 100, no. 24 (2003): 13940-13945.

[5] Feng Zhang, Li-Ping Wang, Martin Brauner, Jana F. Liewald, Kenneth Kay, Natalie Watzke, Phillip G. Wood *et al.* "Multimodal fast optical interrogation of neural circuitry." Nature 446, no. 7136 (2007): 633-639.

[6] R. Pashaie et al., Optogenetic brain interfaces, IEEE J. Rev. Biomed. Eng, Vol. 7, p 3-30 (2014).

[7] Zhu P, Fajardo O, Shum J, Zhang Schrer Y-P, Friedrich RW, "High-resolution optical control of spatiotemporal neuronal activity patterns in zebrafish using a digital micromirror device", Nat. Protocols. 2012; 7:14101425.

[8] A. M. Leifer, C. Fang-Yen, M. Gershow, M. J. Alkema, and A. D. T. Samuel, Optogenetic manipulation of neural activity in freely moving Caenorhabditis elegans, Nat. Methods, vol. 8, pp. 147152, 2011.

[9] Nikolenko, V. et al. SLM microscopy: scanless two-photon imaging and photostimulation with spatial light modulators. Front Neural Circuits 2, 5(2008).

[10] Richner TJ, Thongpang S, Brodnick SK, Schendel AA, Falk RW, Krugner-Higby LA, Pashaie R, Williams JC, "Optogenetic micro-electrocorticography for modulating and localizing cerebral cortex activity", J Neural Eng. 2014 Feb;11(1).

[11] Gradinaru, V., Thompson, K.R., Zhang, F., Mogri, M., Kay, K., Schneider, M.B., and Deisseroth, K., "Targeting and readout strategies for fast optical neural control in vitro and in vivo", J. Neurosci. 27, 1423114238.

[12] Thomas Knpfel, Michael Z. Lin, Anselm Levskaya, Lin Tian, John Y. Lin, and Edward S. Boyden, "Toward the Second Generation of Optogenetic Tools", The Journal of Neuroscience, 10 November 2010, 30(45): 14998-15004

[13] James Butler, "Optogenetics: shining a light on the brain", Bioscience Horizons, pp. 1-8, (2012).

[14] http://en.wikipedia.org/wiki/Channelrhodopsin

[15] Xiao Xu, Honglin Liu and Lihong V. Wang, "Time-reversed ultrasonically encoded optical focusing into scattering media", Nature Photonics 5, 154157 (2011)

[16] Wang YM, Judkewitz B, Dimarzio CA, Yang C, "Deep-tissue focal fl uorescence imaging with digitally time-reversed ultrasound-encoded light", Nat Commun. 2012 Jun 26;3:928

[17] Azimipour M, Baumgartner R, Liu Y, Jacques SL, Eliceiri K, Pashaie R; Extraction

of optical properties and prediction of light distribution in rat brain tissue. J. Biomed. Opt. 0001;19(7):075001. doi:10.1117/1.JBO.19.7.075001.

[18] E. S. Boyden, F. Zhang, E. Bamberg, G. Nagel, and K. Deisseroth, "Millisecond-timescale, genetically targeted optical control of neural activity," Nature Neuroscience, Vol. 8, pp. 1263-1268, 2005.

[19] F. Zhang, A. M. Aravanis, A. Adamantidis, L. de Lecea, K. Deisseroth K, "Circuit-breakers: optical technologies for probing neural signals and systems," Nat Rev Neurosci., 8, 577-581, 2007.

[20] F. Zhang, L. P. Wang, M. Brauner, J. F. Liewald, K. Kay, N. Watzke, P. H. Wood, E. Bamberg, G. Nagel, A. Gottschalk, K. Deisseroth "Multimodal fast optical interrogation of neural circuitry," Nature, 446, 633-39, 2007.

[21] Feng Zhang, Viviana Gradinaru, Antoine R Adamantidis, Remy Durand, Raag D Airan, Luis de Lecea, Karl Deisseroth, "Optogenetic interrogation of neural circuits: technology for probing mammalian brain structures," Nature Protocol, Vol. 5, No. 3, pp. 439-456 , 2010.

[22] Deisseroth, K., Optogenetics. Nat Meth, 2011. 8(1): p. 26-9.

[23] Fenno, L., O. Yizhar, and K. Deisseroth, The development and application of optogenetics. Ann Rev Neurosci, 2011. 34: p. 389-412.

[24] Yizhar,O., Fenno, L. E.,Davidson, T. J.,Mogri, M., and Deisseroth, K. (2011). Optogenetics in neural systems. Neuron, 71(1), 9-34.

[25] R. Pashaie, P. Anikeeva, J. H. Lee, R. Prakash, O. Yizhar, M. Prigge, D. Chander, T. Richner, and J. Williams, "Optogenetic Brain Interfaces," IEEE J. Reviews on Biomedical Engineering, Jan. 2014.

[26] Mattis J, Tye KM, Ferenczi EA, Ramakrishnan C, O'Shea DJ, Prakash R, Gunaydin LA, Hyun M, Fenno LE, Gradinaru V, Yizhar O, Deisseroth K. "Principles for applying optogenetic tools derived from direct comparative analysis of microbial opsins," Nat Methods. 2011 Dec 18;9(2):159-72.

[27] D. Dudley, W. Duncan, and J. Slaughter, "Emerging Digital Micromirror Device (DMD) Applications," Proc. SPIE, 4985, 14-25, 2003.

[28] R. Prakash, O. Yizhar, B. Grewe, C. Ramakrishnan, N. Wang, I. Goshen, A. M. Packer, D. S. Peterka, R. Yuste, M. J. Schnitzer, K. Deisseroth, "Two-photon optogenetic toolbox for fast inhibition, excitation and bistable modulation," Nature Methods, Vol. 9, pp. 1171-1179, 2012.

[29] V. Nikolenko, B. O. Watson, R. Araya, A. Woodruff, D. S. Peterka, and R. Yuste, "SLM Microscopy: Scanless Two-Photon Imaging and Photostimulation with Spatial Light Modulators," Front Neural Circuits. 2008; 2: 5.

[30] Ramin Pashaie, Ryan Falk, "Single Optical Fiber Probe for Fluorescence Detection and Optogenetic Stimulation," IEEE Transaction Biomedical Engineering, Vol. 60, No. 2, pp. 268-280, Feb. 2013

[31] Ramin Pashaie, Ryan Falk, "Spectral Analysis of Whisking Output via Optogenetic Modulation of Vibrissa Cortex in Rat," Biomed. Optics Express, Vol. 4, No. 1, Jan. 2013

[32] Aravanis A, Wang LP, Zhang F, Meltzer L, Mogri M, Schneider MB, Deisseroth K., "An optical neural interface: in vivo control of rodent motor cortex with integrated fiberoptic and optogenetic technology", J. Neural Eng. 2007 Sep;4(3):S143-56. Epub 2007

[33] Tuan Vo-Dinh, "Biomedical Photonics Handbook," ISBN-10: 0849311160, Ed. 1, March 2003.

[34] Stark E, Koos T, Buzsaki G, "Diode probes for spatiotemporal optical control of multiple neurons in freely moving animals", J Neurophysiol 108: 349-363 2012

[35] Al-Juboori SI, Dondzillo A, Stubblefield EA, Felsen G, Lei TC, et al., "Light Scattering Properties Vary across Different Regions of the Adult Mouse Brain", PLoS ONE 8(7): e67626. doi:10.1371/journal.pone.0067626 (2013)

[36] Steven L. Jacques, Ravikant Samatham, Niloy Choudhury, Yongji Fu, David Levitz, "Measuring tissue optical properties in vivo using reflectance-mode confocal microscopy and OCT," Proc. SPIE 6864, Biomedical Applications of Light Scattering II, 68640B (February 15, 2008); doi:10.1117/12.761803.

[37] Steven L Jacques, Optical properties of biological tissues: "A review, Physics in Medicine and Biology", Volume 58, Number 11, 2013.

[38] M. S. Patterson, B. Chance, and B. C. Wilson, "Time resolved reflectance and transmittance for the noninvasive measurement of tissue optical properties," Appl. Opt. 28, 2331-2336 (1989).

[39] M. S. Patterson, J. D. Moulton, B. C. Wilson, K. W. Berndt, and J. R. Lakowicz, "Frequency-domain reflectance for determination of the scattering and absorption properties of tissue," Appl. Opt. 30, 4474-4476, (1991).

[40] T. J. Farrell, M. S. Patterson, and B. C. Wilson, "A diffusion theory model of spatially resolved, steady-state diffuse reflectance for the noninvasive determination of tissue optical properties in vivo," Med. Phys. 19, 879-888 (1992).

[41] Pickering J W, Prahl S, van Wieringen N, Beek J F and van Gemert M J C, "A double integrating sphere system to measure the optical properties of tissue Appl". Opt. 32 399-410 (1993)

[42] S. A. Prahl, M. J. C. van Gemert, and A. J. Welch, "Determining the optical properties of turbid media by using the adding-doubling method," Appl. Opt., 32, pp. 559-568, 1993.

[43] www.mathworks.com

[44] http://www.ni.com/labview/

[45] http://www.edmundoptics.com/technical-resources-center/imaging/telecentricity-and-telecentric-lenses-in-machine-vision/

[46] Robert G. Keys, "Cubic Convolution Interpolation for Digital Image Processing," IEEE TRANS. ACOUSTICS, SPEECH, AND SIGNAL PROCESSING, VOL. ASSP-29, NO. 6, DECEMBER 1981 1153

[47] Johnson GA, Calabrese E, Badea A, Paxinos G, Watson C, "A multidimensional magnetic resonance histology atlas of the Wistar rat brain", Neuroimage 62(3), pp. 1848-1856, 2012.

[48] Ishimaru, "Wave Propagation and Scattering in Random Media", Academic, New York, 1978.

[49] http://omlc.ogi.edu/software/mc/mcxyz/index.html.

[50] Wang, L., Jacques, S. L. and Zheng, L. "MCML-Monte Carlo modeling of light transport in multi-layered tissues", Comput. Methods Programs Biomed. 47, pp. 131-146, 1995.

[51] Tejeda, H., Li, T. and Mohanty, S., "Comparison between Bessel and Gaussian beam propagation for in-depth optogenetic stimulation", in SPIE BiOS 85860G-85860G, 2013.

[52] B. C. Wilson, "Measurement of tissue optical properties: methods and theories", in Optical-Thermal Response of Laser Irradiated Tissue, A. J. Welch and M. J. C. van Gemert, Eds., Chap. 8, pp. 233-274, Plenum, New York 1995.

[53] Bosschaart N, Edelman GJ, Aalders MC, van Leeuwen TG, Faber DJ, "A literature review and novel theoretical approach on the optical properties of whole blood", Lasers Med Sci. 2014 Mar;29(2):453-79

[54] T. Richner, R. Baumgartner, S. Brodnick, M. Azimipour, L. Krugner-Higby, K. Eliceiri, J. Williams, and R. Pashaie, "Patterned optogenetic modulation of neurovascular and metabolic signals," J. Cereb. Blood Flow Metab., **35**, 140 (2015).

[55] M. Azimipour, R. Baumgartner, Y. Liu, S. Jacques, K. Eliceiri, and R. Pashaie, "Extraction of Optical Properties and Prediction of Light Distribution in Rat Brain Tissue", J. Biomed. Optics, **19** 075001 (2014).

[56] J. Lee, V. Srinivasan, H. Radhakrishnan, and D. Boas, "Motion correction for phase-resolved dynamic optical coherence tomography imaging of rodent cerebral cortex" Opt. Express, **19**, 21258 (2011).

[57] V. Srinivasan, J. Jiang, M. Yaseen, H. Radhakrishnan, W. Wu, S. Barry, A. Cable, and D. Boas, Rapid volumetric angiography of cortical microvasculature with optical coherence tomography, Opt. Lett., **35**, 43 (2010).

[58] F. Atry, S. Frye, T. Richner, S. Brodnick, A. Soehartono, J. Williams, and R. Pashaie, "Hemodynamic Response of Cortical Tissue to Optogenetic Stimulation In Transgenic Mice," IEEE Trans. Biomed. Eng., **62**, 766 (2015).

[59] Yuming Liu, Steven L. Jacques, Mehdi Azimipour, Jeremy D. Rogers, Ramin Pashaie, and Kevin W. Eliceiri, "OptogenSIM: a 3D Monte Carlo simulation platform for light delivery design in optogenetics," Biomed. Opt. Express 6, 4859-4870 (2015)

[60] R. Pashaie, R. Baumgartner, TJ. Richner, SK. Brodnick, M. Azimipour, KW. Eliceiri, JC. Williams, "Closed-Loop Optogenetic Brain Interface," in IEEE Transactions on Biomedical Engineering, vol. 62, no. 10, pp. 2327-2337, Oct. 2015. doi: 10.1109/TBME.2015.2436817

[61] Mehdi Azimipour, Farid Atry, and Ramin Pashaie, "Effect of blood vessels on light distribution in optogenetic stimulation of cortex," Opt. Lett. 40, 2173-2176 (2015). doi:10.1364/OL.40.002173

[62] Chen Y. et al., Integrated optical coherence tomography (OCT) and fluorescence laminar optical tomography (FLOT), IEEE J. Sel. Top. Quantum Electron. 16, (4), 755 766 (2010).

[63] Huang, D., Swanson, E. A., Lin, C. P., Schuman, J. S., Stinson, W. G., Chang, W., Hee, M. R., Flotte, T., Gregory, K., Puliafito, C. A., Fujimoto, J. G. (1991) Science 254, 1178

[64] Gibson A and Dehghani H 2009 Diffuse optical imaging Phil. Trans. R. Soc. A 367 3055-72

[65] Elizabeth M. C. Hillman, David A. Boas, Anders M. Dale, and Andrew K. Dunn, "Laminar optical tomography: demonstration of millimeter-scale depth-resolved imaging in turbid media," Opt. Lett. 29, 1650-1652 (2004)

[66] T. Durduran, R. Choe, W.B. Bake, A.G. Yodh, "Diffuse optics for tissue monitoring and tomography", Rep. Prog. Phys., 73 (2010), p. 076701

[67] D. Huang, E. A. Swanson, C. P. Lin, J. S. Schuman, W. G. Stinson, W. Chang, M. R. Hee, T. Flotte, K. Gregory, C. A. Puliafito, and J. G. Fujimoto, "Optical coherence tomography", Science, vol. 254, pp.1178 -1181 1991

[68] O'Leary MA, Boas DA, Chance B, Yodh AG. Experimental images of heterogeneous turbid media by frequency-domain diffusing-photon tomography. Opt Lett. 1995 Mar 1; 20(5):426-8.

[69] Markel V A, Mital V and Schotland J C 2003 Inverse problem in optical diffusion tomography: III. Inversion formulas and singular-value decomposition J. Opt. Soc. Am. A 20 890902

[70] R. Gordon , R. Bender and G. T. Herman "Algebraic reconstruction techniques (ART) for three-dimensional electron microscopy and X-ray photography", J. Theor. Biol., vol. 29, pp.471 -481 1970

[71] Anderson A and Kak A 1984 Simultaneous algebraic reconstruction technique (SART): a superior implementation of the ART algorithm, Ultrason. Imaging 6 81-94

[72] Gilbert P. Iterative methods for the 3D reconstruction of an object from projections. J. Theor. Biol. 1972;76:105117

[73] Stigler, Stephen M. (1981). "Gauss and the Invention of Least Squares". Ann. Statist. 9 (3): 465474. doi:10.1214/aos/1176345451

[74] Avinash C. Kak, Malcolm Slaney, "Principles of Computerized Tomographic Imaging", IEEE Press, 1988

[75] http://www.photometrics.com/products/adapters/xt2.php

[76] Ramin Pashaie, Ryan Falk, "Single Optical Fiber Probe for Fluorescence Detection and Opto-genetic Stimulation," IEEE Transaction Biomedical Engineering, Vol. 60, No. 2, pp. 268-280, Feb. 2013.

[77] Ramin Pashaie, Ryan Falk, "Spectral Analysis of Whisking Output via Optogenetic Modulation of Vibrissa Cortex in Rat," Biomed. Optics Express, Vol. 4, No. 1, Jan. 2013

[78] http://www.bdbiosciences.com/

[79] Venkaiah C. Kavuri, Zi-Jing Lin, Fenghua Tian, and Hanli Liu, "Sparsity enhanced spatial resolution and depth localization in diffuse optical tomography," Biomed. Opt. Express 3, 943-957 (2012)

[80] Haijing Niu, Fenghua Tian, Zi-Jing Lin, and Hanli Liu, "Development of a compensation algorithm for accurate depth localization in diffuse optical tomography," Opt. Lett. 35, 429-431 (2010)

[81] Meng Cui and Changhuei Yang, "Implementation of a digital optical phase conjugation system and its application to study the robustness of turbidity suppression by phase conjugation", Optics Express, Volume 22, Issue 10, Page 11918

[82] Jang M, Ruan H, Zhou H, Judkewitz B, Yang C, "Method for auto-alignment of digital optical phase conjugation systems based on digital propagation", Opt Express. 2014 Jun 16;22(12):14054-71

[83] Zahid Yaqoob, Demetri Psaltis, Michael S. Feld and Changhuei Yang, "Optical phase conjugation for turbidity suppression in biological samples", Nature Photonics 2, 110 - 115 (2008)

[84] Mathias Fink, "Time-Reversed Acoustics", Scientific American November 1999. pp. 91-97. Zahid Yaqoob, Demetri Psaltis1, Michael S. Feld and Changhuei Yang, "Optical phase conjugation for turbidity suppression in biological samples", Nature Photonics 2, 110 - 115 (2008)

[85] I. M. Vellekoop and A. P. Mosk, "Focusing coherent light through opaque strongly scattering media", Optics Letters, Vol. 32, Issue 16, pp. 2309-2311 (2007)

[86] I. M. Vellekoop and A. P. Mosk,"Phase control algorithms for focusing light through

turbid media", Optics Communications Volume 281, Issue 11, 1 June 2008, Pages 30713080

[87] S. M. Popoff, G. Lerosey, R. Carminati, M. Fink, A. C. Boccara, and S. Gigan, "Measuring the Transmission Matrix in Optics: An Approach to the Study and Control of Light Propagation in Disordered Media", Phys. Rev. Lett. 104, 100601 Published 8 March 2010

[88] Donald B. Conkey, Antonio M. Caravaca-Aguirre, and Rafael Piestun, "High-speed scattering medium characterization with application to focusing light through turbid media", Optics Express, Volume 20, Issue 2, Page 1733, 2012

[89] http://en.wikipedia.org/wiki/Nonlinear-optics

[90] http://cns-alumni.bu.edu/ slehar/PhaseConjugate/PhaseConjugate.html

[91] Ivo M. Vellekoop and Christof M. Aegerter , "Scattered light fluorescence microscopy: imaging through turbid layers", Optics Letters, Vol. 35, Issue 8, pp. 1245-1247 (2010)

[92] I. M. Vellekoop, E. G. van Putten, A. Lagendijk, and A. P. Mosk, "Demixing light paths inside disordered metamaterials", Optics Express, Vol. 16, Issue 1, pp. 67-80 (2008).

[93] Fanting Kong, Ronald H. Silverman, Liping Liu, Parag V. Chitnis, Kotik K. Lee, and Y. C. Chen, "Photoacoustic-guided convergence of light through optically diffusive media", Optics Letters, Vol. 36, Issue 11, pp. 2053-2055 (2011)

[94] Hao F Zhang, Konstantin Maslov, George Stoica, Lihong V Wang, "Functional photoacoustic microscopy for high-resolution and noninvasive in vivo imaging", Nature Biotechnology 24, 848 - 851 (2006)

[95] Ichirou Yamaguchi and Tong Zhang,"Phase-shifting digital holography", Optics Letters, Vol. 22, Issue 16, pp. 1268-1270 (1997)

[96] Meng Cui, "Parallel wavefront optimization method for focusing light through random scattering media",Optics Letters, Vol. 36, Issue 6, pp. 870-872 (2011)

[97] Meng Cui,"A high speed wavefront determination method based on spatial frequency modulations for focusing light through random scattering media", Optics Express, Vol. 19, Issue 4, pp. 2989-2995 (2011)

[98] Fanting Kong, Ronald H. Silverman, Liping Liu, Parag V. Chitnis, Kotik K. Lee, and Y. C. Chen,"Photoacoustic-guided convergence of light through optically diffusive media", Optics Letters, Vol. 36, Issue 11, pp. 2053-2055 (2011)

[99] Zhou EH, Ruan H, Yang C, Judkewitz B. Focusing on moving targets through scattering samples. Optica. 2014;1(4):227-232. doi:10.1364/OPTICA.1.000227.

[100] Ma C, Xu X, Liu Y, Wang LV. Time-reversed adapted-perturbation (TRAP) optical focusing onto dynamic objects inside scattering media. Nature photonics. 2014;8(12):931-936. doi:10.1038/nphoton.2014.251.

[101] Wang, Ying Min (2013) Deep tissue fluorescence imaging with time-reversed light. Dissertation (Ph.D.), California Institute of Technology. http://resolver.caltech.edu/CaltechTHESIS:04282013-103938118

[102] Mehdi Azimipour, Farid Atry, and Ramin Pashaie, "Calibration of Digital Optical Phase Conjugation Setups Based on Orthonormal Rectangular Polynomials," Appl. Opt. 55, 2873-2880 (2016). Doi:10.1364/AO.55.002873

[103] X. Xu, H. Liu, and L. V. Wang, "Time-reversed ultrasonically encoded optical focusing into scattering media", Nature Photonics **5**, 154157 (2011)

[104] K. Si, R. Fiolka, M. Cui, "Fluorescence imaging beyond the ballistic regime by ultrasound-pulse-guided digital phase conjugation", Nature Photon. **6**, 657661 (2012).

[105] V. N. Mahajan and G. m. Dai, "Orthonormal polynomials in wavefront analysis: analytical solution", J. Opt. Soc. Am. A., **24**, 29943016 (2007).

[106] M. Born, E. Wolf, "Principles of Optics", 7th ed., Cambridge University, (1999).

[107] D. J. Cho, S. T. Thurman, .J T. Donner, and G. M. Morris, "Characteristics of a 128×128 liquid crystal spatial light modulator for wavefront generation", Opt. Lett. **23**, 969971 (1998).

[108] X. Xun and R. W. Cohn, "Phase calibration of spatially nonuniform spatial light modulators", Appl. Opt., **43**, 64006406 (2004).

[109] J. Harriman, A. Linnenberger, and S. Serati, "Improving spatial light modulator performance through phase compensation", Proc. SPIE, **5553**, 58-67 (2004)

[110] H. H. Pennes, Analysis of tissue and arterial blood temperature in the resting human forearm, J. Appl. Physiol., vol. 1, pp. 93122, Aug. 1948.

[111] Shaner, N.C., Steinbach, P.A., Tsien, R.Y. A guide to choosing fluorescent proteins. Nat. Methods 2, 905909 (2005).

[112] Shaner, N. C. et al. Improved monomeric red, orange and yellow fluorescent proteins derived from Discosoma sp. red fluorescent protein. Nature Biotechnol. 22, 15671572 (2004)

[113] Qingchun Guo, Jingfeng Zhou, Qiru Feng, Rui Lin, Hui Gong, Qingming Luo, Shaoqun Zeng, Minmin Luo, and Ling Fu, "Multi-channel fiber photometry for population neuronal activity recording," Biomed. Opt. Express 6, 3919-3931 (2015).

[114] Neumann M, Gabel D. Simple method for reduction of autofluorescence in fluorescence microscopy. J Histochem Cytochem 2002; 50: 437439.

[115] van de Lest, C. H. A.; Versteg, E. M. M.; Veerkamp, J. H.; van Kuppevelt, T. H. Elimination of Autofluorescence in Immunofluorescence Microscopy with Digital Image Processing. J. Histochem. Cytochem. 1995, 43, 727730.

[116] Deliolanis NC, Wurdinger T, Pike L, et al. In vivo tomographic imaging of red-shifted fluorescent proteins. Biomedical Optics Express. 2011;2(4):887-900. doi:10.1364/BOE.2.000887.

[117] S.K. Brodnick et al., "In vivo imaging of spacial and temporal propagation of neural activity after stimulation with a CLEAR microECoG array in GCaMP6f mice", Proceding of society for neuroscience (SFO), 2015.

Appendix I: Abstract of Journal Papers

Journal of Biomedical Optics 19(7), 075001 (July 2014)

Extraction of optical properties and prediction of light distribution in rat brain tissue

Mehdi Azimipour,[a] Ryan Baumgartner,[a] Yuming Liu,[b] Steven L. Jacques,[c,d] Kevin Eliceiri,[b] and Ramin Pashaie[a,*]
[a]University of Wisconsin-Milwaukee, Electrical and Computer Engineering Department, Milwaukee, Wisconsin 53211
[b]University of Wisconsin at Madison, Laboratory for Optical and Computational Instrumentation, 1675 Observatory Drive, Madison, Wisconsin 53706
[c]Oregon Health Science University, Department of Biomedical Engineering, 3303 SW Bond Avenue, Portland, Oregon 97239
[d]Oregon Health Science University, Department of Dermatology, 3303 SW Bond Avenue, Portland, Oregon 97239

Abstract. Predicting the distribution of light inside any turbid media, such as biological tissue, requires detailed information about the optical properties of the medium, including the absorption and scattering coefficients and the anisotropy factor. Particularly, in biophotonic applications where photons directly interact with the tissue, this information translates to system design optimization, precision in light delivery, and minimization of unintended consequences, such as phototoxicity or photobleaching. In recent years, optogenetics has opened up a new area in deep brain stimulation with light and the method is widely adapted by researchers for the study of the brain circuitries and the dynamics of neurological disorders. A key factor for a successful optogenetic stimulation is delivering an adequate amount of light to the targeted brain objects. The adequate amount of light needed to stimulate each brain object is identified by the tissue optical properties as well as the type of opsin expressed in the tissue, wavelength of the light, and the physical dimensions of the targeted area. Therefore, to implement a precise light delivery system for optogenetics, detailed information about the optical properties of the brain tissue and a mathematical model that incorporates all determining factors is needed to find a good estimation of light distribution in the brain. In general, three measurements are required to obtain the optical properties of any tissue, namely diffuse transmitted light, diffuse reflected light, and transmitted ballistic beam. In this report, these parameters were measured *in vitro* using intact rat brain slices of 500 μm thickness via a two-integrating spheres optical setup. Then, an inverse adding doubling method was used to extract the optical properties of the tissue from the collected data. These experiments were repeated to cover the whole brain tissue with high spatial resolution for the three different cuts (transverse, sagittal, and coronal) and three different wavelengths (405, 532, and 635 nm) in the visible range of the spectrum. A three-dimensional atlas of the rat brain optical properties was constructed based on the experimental measurements. This database was linked to a Monte Carlo toolbox to simulate light distribution in the tissue for different light source configurations. [DOI: 10.1117/1.JBO.19.7.075001]

Keywords: optogenetics; absorption coefficient; scattering coefficient; anisotropy factor; integrating sphere; inverse adding doubling; Monte Carlo simulation.

Paper 140237R received Apr. 14, 2014; revised manuscript received Jun. 4, 2014; accepted for publication Jun. 5, 2014; published online Jul. 4, 2014.

Research Article Vol. 55, No. 11 / April 10 2016 / Applied Optics 2873

applied optics

Calibration of digital optical phase conjugation setups based on orthonormal rectangular polynomials

MEHDI AZIMIPOUR, FARID ATRY, AND RAMIN PASHAIE*

Electrical and Computer Engineering Department, University of Wisconsin-Milwaukee, Milwaukee, Wisconsin 53211, USA
**Corresponding author: pashaie@uwm.edu*

Received 7 January 2016; revised 7 March 2016; accepted 7 March 2016; posted 8 March 2016 (Doc. ID 256602); published 5 April 2016

Digital optical phase conjugation (DOPC) has proven to be a promising technique in deep tissue fluorescence imaging. Nonetheless, DOPC optical setups require precise alignment of all optical components to accurately read the wavefront of scattered light in a turbid medium and playback the conjugated beam toward the sample. Minor misalignments and possible imperfections in the arrangement or the structure of the optical components significantly reduce the performance of the method. In this paper, a calibration procedure based on orthogonal rectangular polynomials is introduced to compensate major imperfections including the optical aberration in the wavefront of the reference beam and the substrate curvature of the spatial light modulator without adding extra optical components to the original setup. The proposed algorithm also provides a systematic calibration procedure for mechanical fine tuning of DOPC systems. It is shown experimentally that the proposed calibration process improves the peak-to-background ratio when focusing light after passing through a highly scattering medium.

OCIS codes: (190.5040) Phase conjugation; (090.1995) Digital holography; (220.1000) Aberration compensation; (230.6120) Spatial light modulators.

http://dx.doi.org/10.1364/AO.55.002873

Effect of blood vessels on light distribution in optogenetic stimulation of cortex

Mehdi Azimipour, Farid Atry, and Ramin Pashaie*

Electrical and Computer Engineering Department, University of Wisconsin-Milwaukee, Milwaukee, Wisconsin 53211, USA
**Corresponding author: pashaie@uwm.edu*

Received December 17, 2014; revised April 8, 2015; accepted April 9, 2015;
posted April 17, 2015 (Doc. ID 230883); published May 4, 2015

In this Letter, the impact of blood vessels on light distribution during photostimulation of cortical tissue in small rodents is investigated. Brain optical properties were extracted using a double-integrating sphere setup, and optical coherence tomography was used to image cortical vessels and capillaries to generate a three-dimensional angiogram of the cortex. By combining these two datasets, a complete volumetric structure of the cortical tissue was developed and linked to a Monte Carlo code which simulates light propagation in this inhomogeneous structure and illustrates the effect of blood vessels on the penetration depth and pattern preservation in optogenetic stimulation.

OCIS codes: (170.4500) Optical coherence tomography; (170.3880) Medical and biological imaging.
http://dx.doi.org/10.1364/OL.40.002173

Journal of Cerebral Blood Flow & Metabolism (2015) 35, 140–147

www.jcbfm.com

ORIGINAL ARTICLE

Patterned optogenetic modulation of neurovascular and metabolic signals

Thomas J Richner[1,3], Ryan Baumgartner[2,3], Sarah K Brodnick[1], Mehdi Azimipour[2], Lisa A Krugner-Higby[1], Kevin W Eliceiri[1], Justin C Williams[1] and Ramin Pashaie[2]

The hemodynamic and metabolic response of the cortex depends spatially and temporally on the activity of multiple cell types. Optogenetics enables specific cell types to be modulated with high temporal precision and is therefore an emerging method for studying neurovascular and neurometabolic coupling. Going beyond temporal investigations, we developed a microprojection system to apply spatial photostimulus patterns *in vivo*. We monitored vascular and metabolic fluorescence signals after photostimulation in Thy1-channelrhodopsin-2 mice. Cerebral arteries increased in diameter rapidly after photostimulation, while nearby veins showed a slower smaller response. The amplitude of the arterial response was depended on the area of cortex stimulated. The fluorescence signal emitted at 450/100 nm and excited with ultraviolet is indicative of reduced nicotinamide adenine dinucleotide, an endogenous fluorescent enzyme involved in glycolysis and the citric acid cycle. This fluorescence signal decreased quickly and transiently after optogenetic stimulation, suggesting that glucose metabolism is tightly locked to optogenetic stimulation. To verify optogenetic stimulation of the cortex, we used a transparent substrate microelectrode array to map cortical potentials resulting from optogenetic stimulation. Spatial optogenetic stimulation is a new tool for studying neurovascular and neurometabolic coupling.

Journal of Cerebral Blood Flow & Metabolism (2015) **35,** 140–147; doi:10.1038/jcbfm.2014.189; published online 12 November 2014

Keywords: cerebral hemodynamics; electrophysiology; intrinsic optical imaging; microscopy; neurovascular coupling

Biomedical Optics EXPRESS

OptogenSIM: a 3D Monte Carlo simulation platform for light delivery design in optogenetics

Yuming Liu,[1] Steven L. Jacques,[2,3] Mehdi Azimipour,[4] Jeremy D. Rogers,[1] Ramin Pashaie,[4] and Kevin W. Eliceiri[1,5,*]

[1]*Laboratory for Optical and Computational Instrumentation, Department of Biomedical Engineering, University of Wisconsin at Madison, 1675 Observatory Drive, Madison, WI 53706,USA*
[2]*Department of Biomedical Engineering, Oregon Health and Science University, 3303 SW Bond Ave, Portland, OR 97239, USA*
[3]*Department of Dermatology, Oregon Health and Science University, 3303 SW Bond Ave, Portland, OR 97239, USA*
[4]*Electrical Engineering Department, University of Wisconsin-Milwaukee, 3200 N Cramer St., Milwaukee, Wisconsin 53211, USA*
[5]*Morgridge Institute for Research, 330 North Orchard Street, Madison, WI 53715, USA*
[*]*eliceiri@wisc.edu*

Abstract: Optimizing light delivery for optogenetics is critical in order to accurately stimulate the neurons of interest while reducing nonspecific effects such as tissue heating or photodamage. Light distribution is typically predicted using the assumption of tissue homogeneity, which oversimplifies light transport in heterogeneous brain. Here, we present an open-source 3D simulation platform, OptogenSIM, which eliminates this assumption. This platform integrates a voxel-based 3D Monte Carlo model, generic optical property models of brain tissues, and a well-defined 3D mouse brain tissue atlas. The application of this platform in brain data models demonstrates that brain heterogeneity has moderate to significant impact depending on application conditions. Estimated light density contours can show the region of any specified power density in the 3D brain space and thus can help optimize the light delivery settings, such as the optical fiber position, fiber diameter, fiber numerical aperture, light wavelength and power. OptogenSIM is freely available and can be easily adapted to incorporate additional brain atlases.

OCIS codes: (170.3660) Light propagation in tissues; (170.2945) Illumination design; (080.1753) Computation methods; (170.4090) Modulation techniques.

Closed-Loop Optogenetic Brain Interface

Ramin Pashaie*, *Member, IEEE*, Ryan Baumgartner, Thomas J. Richner, Sarah K. Brodnick, Mehdi Azimipour, Kevin W. Eliceiri, and Justin C. Williams

***Abstract*—This paper presents a new approach for implementation of closed-loop brain–machine interface algorithms by combining optogenetic neural stimulation with electrocorticography and fluorescence microscopy. We used a new generation of microfabricated electrocorticography (micro-ECoG) devices in which electrode arrays are embedded within an optically transparent biocompatible substrate that provides optical access to the brain tissue during electrophysiology recording. An optical setup was designed capable of projecting arbitrary patterns of light for optogenetic stimulation and performing fluorescence microscopy through the implant. For realization of a closed-loop system using this platform, the feedback can be taken from electrophysiology data or fluorescence imaging. In the closed-loop systems discussed in this paper, the feedback signal was taken from the micro-ECoG. In these algorithms, the electrophysiology data are continuously transferred to a computer and compared with some predefined spatial-temporal patterns of neural activity. The computer which processes the data also readjusts the duration and distribution of optogenetic stimulating pulses to minimize the difference between the recorded activity and the predefined set points so that after a limited period of transient response the recorded activity follows the set points. Details of the system design and implementation of typical closed-loop paradigms are discussed in this paper.**

***Index Terms*—Brain interface, closed loop, fluorescence imaging, hemodynamic signals, optogenetics, spatial light modulator (SLM).**

The most common method in recording brain activity for BMI applications, due to the preference for minimum invasiveness, is electroencephalography where electrical activity is recorded by a set of electrodes along the scalp. Nevertheless, the more invasive technique of epidural electrocorticography (ECoG), in which electrode arrays are implanted directly on the surface of cortex without penetrating into the tissue, provides more robust and reliable signals, due to the close proximity to the neural tissue [4]–[10]. For realization of closed-loop interfaces, ECoGs are occasionally combined with penetrating microstimulating electrodes. However, simultaneous stimulation and recording has proven to be difficult due to potential electric artifacts that cannot be eliminated completely [11]. In addition, targeting specific cell-types is not feasible since electrodes stimulate all cells in the region with no specificity. Also, electrodes predominately stimulate cells to increase neural activity and they offer no direct mechanism for silencing.

In recent years, by combining optics and molecular genetics, a new methodology for optical modulation of neural activity was introduced. In this approach, known as optogenetics, cell-types of interest are genetically targeted to produce light-gated cation channels or anion pumps that are sensitive to a specific range

Appendix II: CV

MEHDI AZIMIPOUR

Department of Electrical Engineering
University of Wisconsin-Milwaukee

EDUCATION

Master of Science, Electrical Engineering,
Shahid Beheshti University, Tehran, Iran. December 2008

Bachelor of Science, Biomedical Engineering,
Amirkabir University (Tehran Polytechnic), Tehran, Iran. December 2005

JOURNAL PUBLICATIONS

- Mehdi Azimipour, Farid Atry, Ramin Pashaie, Calibration of Digital Optical Phase Conjugation Setups Based on Zernike Decomposition Analysis, Appl. Opt. 55, 2873-2880 (2016).

- Yuming Liu, Steven L. Jacques, Mehdi Azimipour, Jeremy D. Rogers, Ramin Pashaie, and Kevin W. Eliceiri, OptogenSIM: a 3D Monte Carlo simulation platform for light delivery design in optogenetics, Biomed. Opt. Express 6, 4859-4870 (2015)

- Ramin Pashaie, Tom Richner, Ryan Baumgartner, Sarah Brodnick, Mehdi Azimipour, Kevin Eliceiri, Justin Williams: Closed-Loop Optogenetic Brain Interface. IEEE transactions on bio-medical engineering 05/2015; DOI:10.1109/TBME.2015.2436817

- Mehdi Azimipour, Farid Atry, Ramin Pashaie: Effect of blood vessels on light distribution in optogenetic stimulation of cortex. Optics Letters 01/2015; 40(10):2173. DOI:10.1364/OL.40.002173

- Thomas J Richner, Ryan Baumgartner, Sarah K Brodnick, Mehdi Azimipour, Lisa A Krugner-Higby, Kevin W Eliceiri, Justin C Williams, Ramin Pashaie: Patterned optogenetic modulation of neurovascular and metabolic signals. Journal of Cerebral Blood Flow and Metabolism 11/2014; 35(1). DOI:10.1038/jcbfm.2014.189

- Mehdi Azimipour, Ryan Baumgartner, Yuming Liu, Steven L Jacques, Kevin Eliceiri, Ramin Pashaie: Extraction of optical properties and prediction of light distribution in rat brain tissue. Journal of Biomedical Optics 07/2014; 19(7):75001. DOI:10.1117/1.JBO.19.7.075001

- Mehdi Azimipour, Ramin Pashaie: Nonlinear optical signal processing on multiwavelength sensitive materials. Optics Letters 11/2013; 38(21):4324-6. DOI:10.1364/OL.38.004324

- Mohammad MasoudiMotlagh, Jeffery Sugar, Mehdi Azimipour, Whitney Linz, Gregory Michalak, Na Seo, Mahsa Ranji, Monitoring hemodynamic changes in stroke-affected muscles using near-infrared spectroscopy, Journal of Rehabilitation and Assistive Technologies Engineering 11/2015; 1. DOI: 10.1177/2055668315614195

- Azimipour Mehdi, Eshghi Mohammad: Parallel Circular-Scan Architecture. Journal of Applied Sciences 11/2008; DOI:10.3923/jas.2008.2083.2090

- Mehdi Azimipour, Mohammad Reza Bonyadi, Mohammad Eshghi: Using immune genetic algorithm in ATPG. Australian Journal of Basic and Applied Sciences 01/2008; 2:920-928.

CONFERENCE PRESENTATIONS

- Mehdi Azimipour, Farid Atry, Ramin Pashaie, Light pattern preservation in rodents cortical tissue during opto-genetic neuro-stimulation, SPIE Photonic West, San Francisco, Feb. 2016.

- Farid Atry, Ramin Pashaie, Iterative calibration of a digital optical phase conjugation system, SPIE Photonic West, San Francisco, Feb. 2016.

- Mehdi Azimipour, Ryan Baumgartner, Yuming Liu, Amy L. Kaczmarowski, Steven L. Jacques, Kevin Eliceiri, Ramin Pashaie, Development of a simulation toolbox for predicting light distribution in rat brain tissue during optical stimulation, SPIE Photonic West, San Francisco, Feb. 2014.

HONORS AND AWARDS

- Distinguished Graduate Student Fellowship (DGSF),
  University of Wisconsin Milwaukee ($15,000) 2015

- UWM Chancellors Graduate Student Award, College of Engineering
  and Applied Science, University of Wisconsin-Milwaukee ($2,000) 2014

- UWM Chancellors Graduate Student Award, College of Engineering
  and Applied Science, University of Wisconsin-Milwaukee ($1,000) 2013

- UWM Chancellors Graduate Student Award, College of Engineering
  and Applied Science, University of Wisconsin-Milwaukee ($1,000) 2014

- Iran Telecommunication Research Center (ITRC), master thesis support 2006

PROFESSIONAL EXPERIENCE

Teaching

- Electronics (I), Instructor, College of Computer and Information Technology,
  Payam Nour University, Tehran, Iran 2007

- Digital Logics, Instructor, College of Computer and Information Technology,
  Payam Nour University, Tehran, Iran 2007

- Microprocessors/Lab, Instructor, College of Computer and Information Technology,
  Payam Nour University, Tehran, Iran 2007

- Teaching Assistant, Department of electrical Engineering,
  University of Wisconsin-Milwaukee. 2014

Researcher

- Project Assistant, Department of electrical Engineering,
  University of Wisconsin-Milwaukee. 2012

- Research Assistant, Department of electrical Engineering,
  University of Wisconsin-Milwaukee 2013-2014

PROGRAMMING SKILLS

- MATLAB, LabView, Zemax, VHDL, C/C++, ModelSim, Hspice.

PROFESSIONAL AFFILIATIONS

- Society of Photo-Optical Instrumentation Engineers (SPIE), Student Member. 2015-Present

- Optical Society of America (OSA), UW-Milwaukee Chapter. 2013-2014

- Institute of Electrical and Electronics Engineers (IEEE), UW-Milwaukee Chapter. 2015-Present